



Università degli Studi di Napoli Federico II

*Dottorato di Ricerca in Fisica Fondamentale ed Applicata  
XVIII ciclo*

**Roberto Santorelli**

**WARP:  
a direct search for Dark Matter**

**Il Coordinatore:**  
Prof. Arturo Tagliacozzo

Novembre 2005



*Dedicato a Diego*  
*(nonostante tutte le notti insonni)*



# Contents

## Introduction

<b>1</b>	<b>The Dark Matter Problem</b>	<b>11</b>
1.1	INTRODUCTION . . . . .	11
1.2	ASTROPHYSICAL EVIDENCE OF DARK MATTER . . . . .	11
1.3	BARYONIC DARK MATTER . . . . .	15
1.4	COSMIC MICROWAVE BACKGROUND ANISOTROPIES . . . . .	15
1.5	COMPOSITION OF THE UNIVERSE . . . . .	20
1.6	COLD AND HOT DARK MATTER AND RELIC DENSITY . . . . .	22
1.7	SUPERSYMMETRIC EXTENSION OF THE STANDARD MODEL . . . . .	27
1.7.1	GUT . . . . .	29
1.7.2	SUPERPARTICLES . . . . .	32
1.7.3	R-PARITY . . . . .	33
1.8	THE GALACTIC DARK HALO . . . . .	35
<b>2</b>	<b>WIMP direct detection</b>	<b>38</b>
2.1	INTRODUCTION . . . . .	38
2.2	EXPECTED RECOIL SPECTRUM AND INTERACTION RATE . . . . .	38
2.3	LOW BACKGROUND TECHNIQUES . . . . .	45
2.4	REVIEW OF PRESENT EXPERIMENTS . . . . .	48
2.5	NOBLE LIQUIDS EXPERIMENTS . . . . .	53
2.6	INDIRECT WIMP SEARCHES . . . . .	55
<b>3</b>	<b>WARP 2.3 liters</b>	<b>57</b>
3.1	INTRODUCTION . . . . .	57
3.2	LIQUID ARGON AS WIMP TARGET . . . . .	57
3.3	SCINTILLATION LIGHT EMISSIONS IN LAr . . . . .	59
3.4	PROPOSED TECHNIQUE . . . . .	64
3.5	SETUP OF THE 2.3l TEST CHAMBER . . . . .	66
3.6	DATA ACQUISITION . . . . .	72
3.7	RESULTS OF THE PRELIMINARY TESTS . . . . .	74

3.8	WARP 2.3L CHAMBER AT LNGS . . . . .	79
3.8.1	SETUP . . . . .	79
3.8.2	DATA ACQUISITION . . . . .	81
3.9	RESULTS AT LNGS . . . . .	82
3.9.1	OBSERVATION OF THE INTERNAL $^{222}\text{Rn}$ AND $^{39}\text{Ar}$ SIGNALS . . . . .	83
3.10	ARGON RECOIL EVENTS SELECTION . . . . .	87
3.10.1	PULSE SHAPE DISCRIMINATION . . . . .	89
3.11	PRELIMINARY RESULTS ABOUT NUCLEAR RECOILS IDENTIFICATION . . . . .	91
<b>4</b>	<b>WARP 100L</b>	<b>94</b>
4.1	INTRODUCTION . . . . .	94
4.2	GENERAL LAYOUT . . . . .	94
4.3	INNER DETECTOR . . . . .	96
4.4	ACTIVE VETO . . . . .	98
4.5	PASSIVE SHIELDING . . . . .	100
4.6	READOUT ELECTRONICS AND TRIGGER SYSTEM . . . . .	102
4.7	BACKGROUND ESTIMATION . . . . .	103
4.7.1	NEUTRONS INDUCED BACKGROUND . . . . .	103
4.7.2	$\beta - \gamma$ INDUCED BACKGROUND . . . . .	112
4.7.3	OTHER BACKGROUND SOURCES . . . . .	114
4.8	EXPECTED EXPERIMENTAL SENSITIVITY . . . . .	116
<b>5</b>	<b>Characterization of photomultiplier tubes for the WARP experiment</b>	<b>118</b>
5.1	INTRODUCTION . . . . .	118
5.2	CRYOGENIC PHOTOMULTIPLERS . . . . .	119
5.3	AIM OF THE TESTS . . . . .	121
5.4	PMT TEST FACILITY . . . . .	125
5.4.1	MECHANICAL SET-UP . . . . .	125
5.4.2	DATA ACQUISITION AND ANALYSIS SOFTWARE . . . . .	128
5.5	RESULTS . . . . .	131
5.5.1	DARK COUNTS AND SINGLE PHOTOELECTRON RESPONSE . . . . .	131
5.5.2	MULTIPHOTONS RESPONSE . . . . .	137
5.6	POSSIBLE IMPROVEMENTS TO THE SET-UP . . . . .	141
	<b>Conclusions</b>	<b>145</b>
	<b>Bibliography</b>	<b>148</b>

*"L'Anticristo può nascere dalla stessa pietà, dall'eccessivo amor  
di Dio o della verità, come l'eretico nasce dal santo e  
l'indemoniato dal veggente.  
Temi, Adso, i profeti e coloro disposti a morire per la verità.  
... l'unica verità è imparare a liberarci dalla passione insana per  
la verità..."*

(*"Il nome della Rosa"*)



## Introduction

The main aim of this work is to present the results of my activity during the period as PhD student. During the last three years I was involved in the **WARP** experiment (*WIMP ARGon Programme*), whose aim is to obtain an evidence of the WIMPs existence through direct detections of their elastic scattering over the Argon nuclei. The first half of my PhD was spent between Napoli and Pavia Universities developing a double phase Argon chamber. I was involved in the improvement of the hardware set-up of a test chamber and in data analysis carried out during the last part of the *R&D* period in Pavia. In addition I developed some MonteCarlo studies in Naples, regarding mainly the light collection and field simulation. During the second half of my doctorate, I gave a contribute to the data taking at Gran Sasso national laboratory. Moreover, a large part of the activity was focused on the study of a new detector with 100l of sensitive volume. The main subject of this activity was the development of a MonteCarlo simulation of background and the setting-up of a facility in Naples for the test and the characterization of the cryogenic photomultipliers, used to detect the scintillation light produced in Argon.

The guide idea of this work is to merge the intention of reporting the main aspects of the research and the necessity of underlining my personal contribution to the activity. Anyway, I had the pleasure, like other members of the collaboration, to take part to a lot of activities regarding the experiment, so my contribute is spread in different aspects of the research. The final result is a good compromise, thus the main aspects of the research are presented in an exhaustive manner and my personal contribution stands out by pointing time by time on some specific aspects.

In this thesis the first two chapters are dedicated to the presentation of the *Dark Matter* problem. In chapter 1 the main evidences of the existence of more matter in the Universe than the baryonic component is presented, and a possible explanation of the *Dark Matter* problem in the Particle Physics field is given. In chapter 2 is dedicated to the description of the direct search of *Dark Matter*; theoretical prediction are discussed with the main experimental techniques. In chapter 3, after a brief description of the liquid Argon properties, the proposed technology, based on the contemporary detection of scintillation light and ionization charge through a double phase detector, is presented. Results of the *R&D* activity on a test chamber with 2.3l of sensitive volume and the preliminary results of the data taking at Gran Sasso laboratory are then presented.

In chapters 4 and 5 the activity concerning a new detector with 100l of sensitive volume, actually under construction, is presented. In chapter 4 the experimental set-up is presented with a MonteCarlo study of the background and an estimation of the experimental sensitivity. Finally, in the last chapter, a detailed description of the experimental set-up of the test facility

made in Naples is given. Preliminary results regarding the characterization of photomultiplier tubes used for the detection of the scintillation light in the detector are also presented.

# Chapter 1

## The Dark Matter Problem

### 1.1 INTRODUCTION

Recent astronomical evidences indicate that only a little fraction of the matter of the Universe is composed by "ordinary" baryonic matter, while about the 90% has an unknown nature. This is the so-called "Dark Matter". During last years, the proofs of the possible presence of Dark Matter have been found coming from several (and independent) investigations in different fields of research. Theoretical predictions suggest that this unknown matter could be made of a generic class of particles called Weakly Interacting Massive Particles (WIMPs), relics of the Big Bang, that still exist today. Moreover, in a completely independent way, the supersymmetric extension of the Standard Model provides a possible WIMP candidate in the lightest supersymmetric particle, that should be stable, enough massive and weakly interacting.

The main aim of this chapter is to present the most interesting evidences that could give proofs of Dark Matter, describing the scenario of the possible composition of the Universe, in which Dark Matter has an important role. The motivations of the so-called SuperSymmetry and its candidate as WIMP are then presented, evidencing how this theory, starting from a completely different point of view, requires the existence of a particle with the same characteristic of the WIMPs. Finally, assuming a relic abundance of WIMPs produced after the Big Bang, a possible presence of a galactic dark halo is considered and its possible theoretical model is presented.

### 1.2 ASTROPHYSICAL EVIDENCE OF DARK MATTER

Although the evidence for the existence of Dark Matter and Dark Energy is indirect, given by observation of their gravitational effects, it is possible to get indication of this evidence on scales ranging from galaxies to the

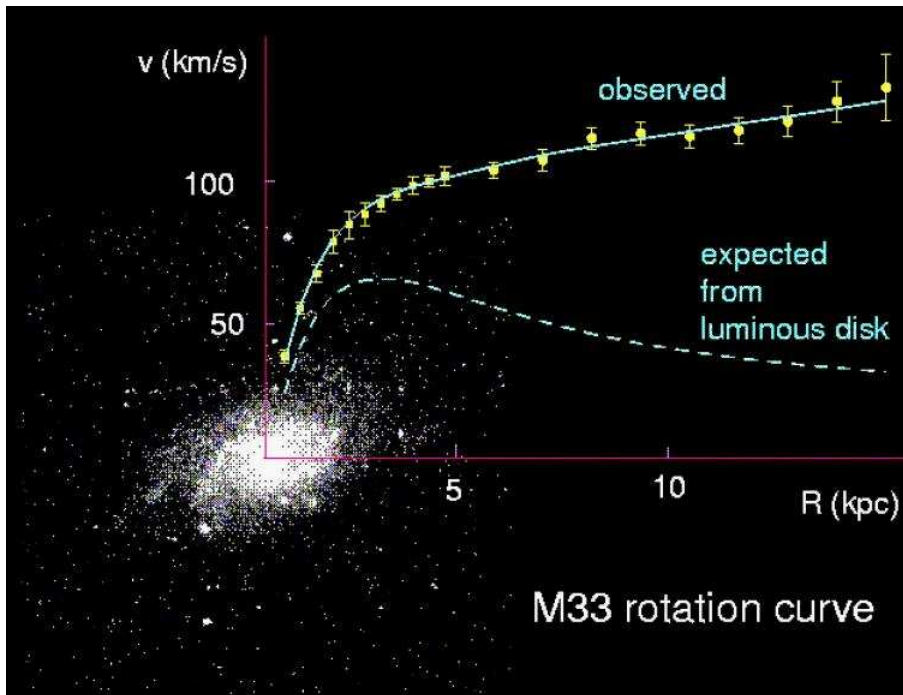


Figure 1.1: Rotation curve of the spiral galaxy M33, superimposed on its optical image. The points are the measured circular rotation velocities as function of the distance from the center of the galaxy. The expected behavior of the rotation curve based on the contribute of luminous disk alone is reported.

whole universe. Dark matter seems to be required from quite independent astrophysical observations. The most important evidence for Dark Matter on galactic scales comes from the observations of the rotation curves of galaxies, i.e. the circular velocities of the objects moving around a galaxy as a function of their distance from the galactic centre (fig. 1.1). During the 30's F. Zwicky made the first proposal for the existence of a "dark" matter component in the universe observing that velocity distributions in the Coma galactic cluster were incompatible with the gravitational effect of visible light-emitted matter by two orders of magnitude. During the 70's, using the observations of the Doppler shift of the 21cm emission by the cold atomic hydrogen clouds moving around the galaxies, it was possible to extend the measurement of the circular velocity far away from the optical disk <sup>1</sup> (the dimension of the gaseous disk is typically two times or more bigger than the optical disk). It's clear that such type of measure is strictly

<sup>1</sup>The optical disk is typically defined as the radius of the region containing the 83% of the total amount of light of a galaxy ( $R_{ott} \sim 10\text{kpc}$ )

related to the mass of the galaxy. According to the Newtonian dynamics, the circular velocity is expected to be

$$v(r) = \sqrt{\frac{GM(r)}{r}} \quad (1.1)$$

where  $M(r) = 4\pi \int \rho(r)r^2 dr$  is the mass included in a sphere of radius  $r$  and  $\rho(r)$  is the density function. In this way the circular velocity should decrease like  $\frac{1}{r^2}$  beyond the region of the optical disk. Nevertheless, the observed rotation curves usually exhibit a characteristic flat behavior at large distances even far beyond the edge of the visible disks. The fact that  $v(r)$  is approximately constant implies the existence of an halo with  $M(r) \propto r$  (and  $\rho(r) \propto 1/r^2$ ). In fig (1.2) it is shown the rotational curve of the galaxy NCG6503 which has an optical disk of 1.73 kpc of radius. As we can see, the rotational speed grows up to the border of the optical disk and then has a flat behaviour ( $115 km/s$ ) up to the last hydrogen cloud moving at 22.22 kpc from the centre. It is surprising that the optical measures on the external stars of the light disk are in agreement with the radio measurements. These measurements were later extended to a large number of spiral galaxies, and a flat speed distribution was found at very large distances from visible objects in the galaxies arms: this suggests a spherical halo of non-visible matter surrounding the galaxies. This spherical halo has the same mass of the visible matter inside a the optic sphere, but its dimension is much larger. If we would like to know the total amount of dark matter in the spiral galaxies, it would be necessary to understand the typical dimension of the dark matter halo. Thus it is necessary to find probes at distances typically bigger then the galactic dimensions. Many spiral galaxies are usually surrounded by satellite galaxies which could be used as probe to study the behavior of the gravitational field of the primary galaxies. In spite of the difficulty of the measurements due to the really long orbital period, the radii of the dark matter's haloes have been statistically estimated to be of the order of 200 kpc, typically ten times bigger than  $R_{opt}$ , with a total mass of the order of  $2 \cdot 10^{12} M_{\odot}$ . Other evidences of dark matter come from the gravitational lensing. Following Einstein's theory of general relativity, light propagates along geodesics which deviate from straight lines when passing near intense gravitational fields. The distortion of the images of background objects due to the gravitational mass can be used to infer the shape of the potential and thus the mass of the object, so the mass of a galaxy can also be estimated directly using the effect of the gravitation lensing on the images of distant quasar. The gravitational deflection of photons passing by a point of mass  $M$  is predicted by Einstein's general theory of relativity and is given by  $\alpha = \frac{4GM}{c^2 b}$  where  $G$  is the gravitational constant,  $c$  the speed of light and  $b$  the closest distance of approach between  $M$  and the photons. The gravitational deflection of light implies that massive objects can be used as gravitational lenses. In this way, it is possible to get the same results obtained using the

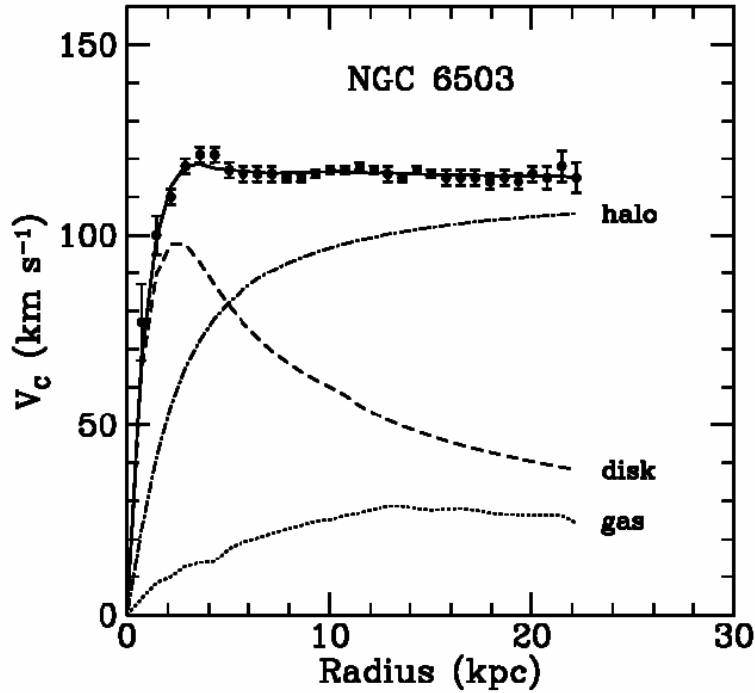


Figure 1.2: Rotation curve for the spiral galaxy NGC6503. The dashed and dotted curves are the contribution to the rotational velocity due to the observed disk and gas, respectively, and the dot-dash curve is the contribution from the dark halo.

previous method based on completely different hypothesis. The information about the shape of the dark matter's halo can be obtained measuring the value of the depth of the gaseous disk as function of the distance from the centre of the galaxy, in fact this value is the result of the competition between the pressure and the gravitational field: the more flat is the disk the more strong is the gravitational field. In this way, observing the shape of the gaseous disks, it is possible to conclude that dark matter's halo of the spiral galaxies has ellipsoidal shape not so different from the spherical approximation. The results regarding elliptical galaxies are not so clear like spiral galaxies. The dynamic analysis about the rotational speed, which has been for long time the only way to investigate the dark matter halo, is not so easy, due to the chaotic movement of the stars in such type of galaxies. The combination of the dynamic analysis and of the gravitational lensing doesn't give an indication of the presence of the dark matter's halo for all the galaxies and it is only possible to get this evidence for the bright galaxies. The experimental observation confirms that the mass of such type of galaxies is dominated by dark matter having an halo typically of the order

of 100 kpc. Another evidence of dark matter comes, on a bigger scale, from the galaxy cluster. If the single galaxies are dominated by dark matter, it is clear that the major part of a cluster's mass comes from the dark matter component. These experimental observations are not so obvious, in fact the study of the dark matter component in the clusters has been developed independently by the study of the dark matter component in the galaxies. The clusters have much of the visible mass in the form of hot X-ray emitting gas. The gas temperature (typically  $10^7 - 10^8$  K) is clearly far in excess of the escape velocities as deduced from the visible mass. The fact that the gas is bound by gravitational forces confirms that the largest part (at least 80%) of the total mass must be dark matter concentrated in the cluster centres. Although both the quantities of dark matter's component in galaxies and cluster are not sufficiently known, there is no evidence of inconsistency.

*References:* [1],[2],[3],[4],[8]

### 1.3 BARYONIC DARK MATTER

Many candidates have been proposed to solve the dark matter problem. It is natural to expect the existence of ordinary baryonic dark matter as astronomical objects with a reduced luminosity, (i.e. difficult to be detected). Possible examples are given by cold  $H_2$  clouds, that do not present characteristic 21 cm line of the atomic hydrogen and that could not emit any radiation (according to their temperature), and by MACHOs (Massive Astrophysical Compact Halo Objects). Many astrophysical objects belong to this category, like neutron stars, brown-white-red-beige dwarf, black holes. Several hundred MACHOs have been observed because of their gravitational lensing of light from some stars in the Large Magellanic Clouds. Although MACHOs seem to have a significant weight as part of the total matter, the following observations seem to exclude a scenario in which the dark matter problem can be explained by baryonic matter.

*References :*[2],[3]

### 1.4 COSMIC MICROWAVE BACKGROUND ANISOTROPIES

For several hundred thousand years after the Big Bang, the universe was hot enough for matter (predominantly hydrogen) to remain ionized. During this period, matter and light were in thermal equilibrium and the radiation is therefore expected to obey the classic blackbody laws (Planck, Wien, Stefan). At some point about 400,000 years after the Bing Bang (and at a temperature of about  $3000K$ ), the universe had cooled to the point where the matter became neutral, at which point the universe's matter also became transparent to the radiation. The Cosmic Microwave Background (CMB) is

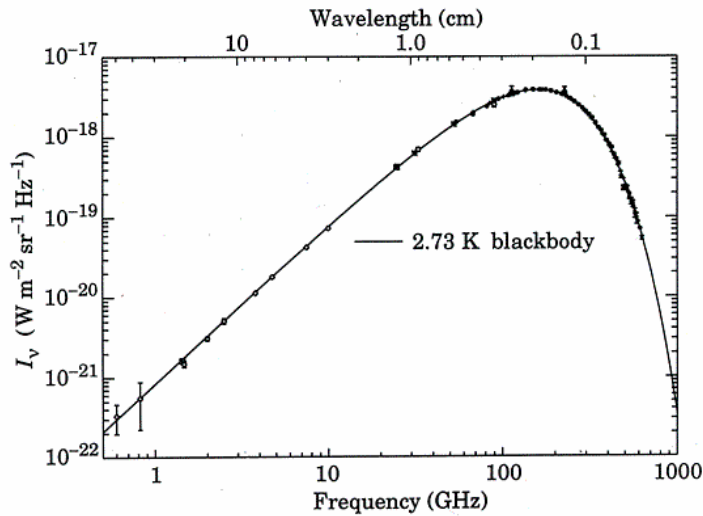


Figure 1.3: CMB spectrum as measured by the COBE satellite.

a millimetre wavelength radiation which fills the space everywhere and it is like a picture of that primordial Universe. Discovered in 1964 by Penzias and Wilson, the CMB is a perfect blackbody spectrum peaked at a temperature of  $2.73\text{K}$  (fig. 1.3). As space expands, wavelength expands according to the same factor, so the very low temperature CMB has today is a consequence of the expansion of the Universe. According to Wien's blackbody law, the wavelength peak of the CMB spectrum is inversely proportional to the temperature of the CMB, therefore the fall in the CMB temperature by a factor of  $10^3$  indicates an expansion of the universe by same order of magnitude from the moment of decoupling until now. The CMB should be essentially isotropic, but not exactly isotropic: careful measurements of the CMB, made for the first time in 1992 by the COBE satellite, reveal tiny anisotropies, i.e. departures from perfect homogeneity and isotropy. The anisotropies existing at the moment of decoupling, representing random noise during the very early universe, were amplified by inflation to cosmic-sized scales in such a way that they can account for the large-scale structures formed under the influence of gravity: it is generally assumed that the abundance of structures seen in the Universe today (galaxies, clusters of galaxies, superclusters...etc) evolved under gravitational interactions from small primordial density inhomogeneities. Since the anisotropies are so tiny, linear perturbation theory within general relativity suffices to treat them. Therefore, from the theoretical point of view, the statistical properties of CMB anisotropies are well understood. The usual way to present them is a curve called the CMB power

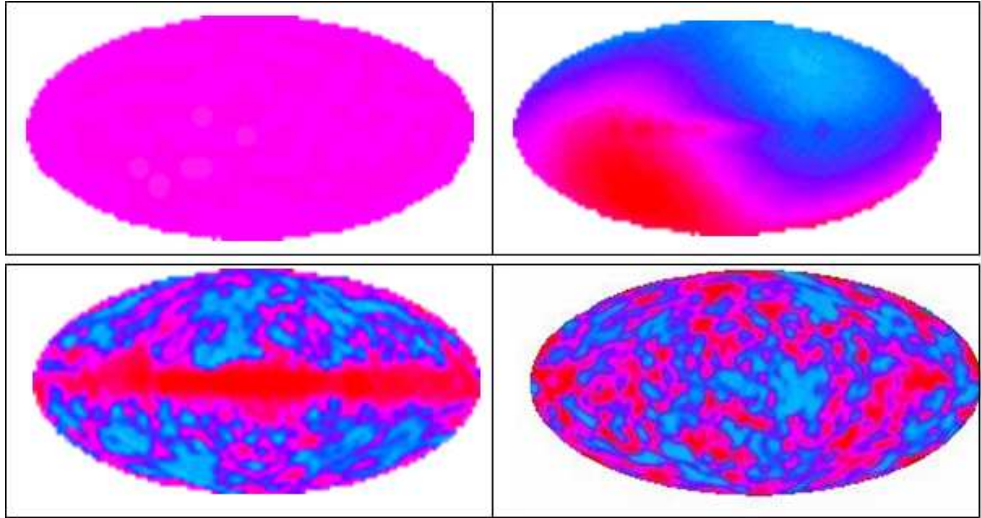


Figure 1.4: In these fig the entire sky is represented by a Mercator projection (the same technique often employed to portray the entire Earth). The galactic equator or plane (latitude 0) is a line running through the middle of the sky pictures. Only reaching a resolution  $\frac{\Delta T}{T} \sim 10^{-5}$  it is possible to discover the true anisotropies pattern (See text for details).

spectrum by spherical-harmonic multipole moments (fig. 1.5),

$$\frac{\Delta T(\theta, \phi)}{T} = \sum_{l,m} a_{l,m} Y_{l,m}(\theta, \phi) \quad (1.2)$$

The multipole moments have zero mean ( $\langle a_{lm} \rangle = 0$ ), and if the underlying density fluctuations are described by a gaussian random process, as inflation predicts, the angular power spectrum,  $C_l = \langle |a_{l,m}|^2 \rangle$ , contains all possible information (the angled brackets indicate the average over all observers in the Universe; the absence of a preferred direction in the Universe implies that C is independent of m). Temperature differences between points on the sky separated by angle  $\theta$  are related to those multipoles with spherical-harmonic indices around  $l \cong \frac{100^\circ}{\theta}$ . The rms fractional temperature fluctuation for a given angular separation is then

$$\left( \frac{\Delta T}{T} \right)_\theta \approx \sqrt{\frac{l(l+1)C_l}{2\pi}} \quad (1.3)$$

Temperature fluctuations in the CMB arise due to the variations in the matter density. After last-scattering CMB photons stream freely to us and the temperature fluctuations are seen as CMB temperature differences (anisotropy) across the sky. The power spectrum depends on the value of

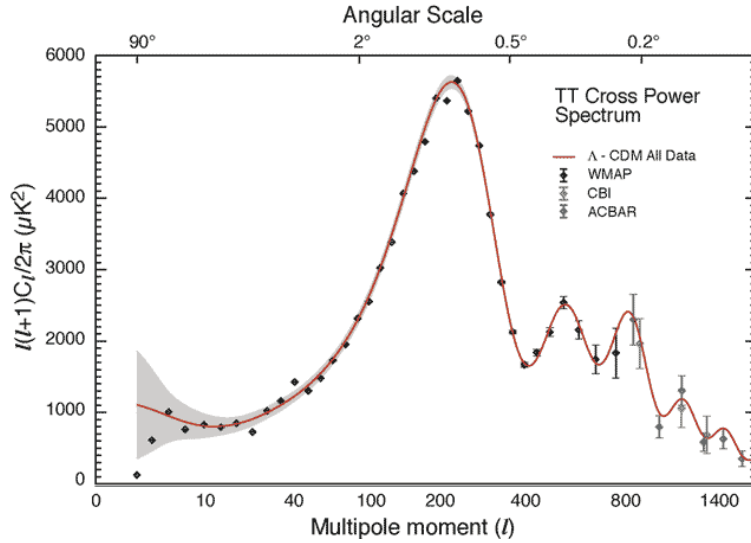


Figure 1.5: Power spectrum of the CMB fluctuations (the data of WMAP are included). These measurements give strong indications of the universe density and of the baryon density.

the so called cosmological parameters, which are a set of ten or so numbers which describe the matter content of the universe (baryons, dark matter, dark energy, neutrinos), its age (hubble parameter), its global geometry (curvature parameter) and the properties of the initial fluctuations (amplitude and spectral index). If the CMB had precisely the same temperature in every direction in the sky, the sky would have the same brightness in every direction. The contribution  $l = 1$  to the power spectrum is uniformly the same in all the directions (fig 1.4). At the level of  $\frac{\Delta T}{T} \sim 10^{-3}$  it is possible to see a dipole pattern in the temperature distribution; this is just a cinematic Doppler effect due to the motion of the Earth with respect to the frame in which the CMB is at rest. Subtracting those contributes together with the contribution of the Milky Way that is bright at microwave wavelengths, at the order of  $\frac{\Delta T}{T} \sim 10^{-5}$  it is possible to discover the true anisotropies in the CMB that were present at the moment of decoupling. Today it possible to perform the calculation necessary to reproduce the observed anisotropies for a given set of cosmological parameters; in this way it is possible to compare theoretical predictions with increasingly accurate measurements in order to determine the value of those parameters. The Inflation Model, with adiabatic perturbations and cold dark matter, predicts a series of peaks in the power spectrum on these scales, known as the Doppler peaks (figure 1.5), and detection of these peaks have a relevant meaning for the cosmology: the position of the first Doppler peak gives the density parameter of the

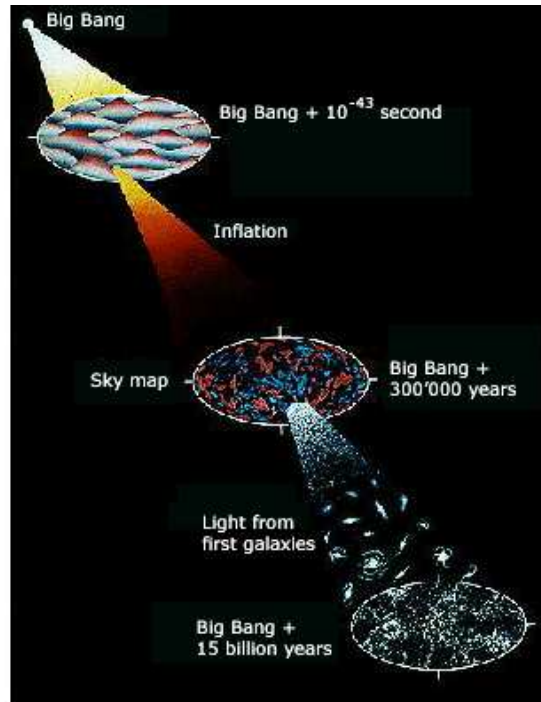


Figure 1.6: Schematic representation of the formation of cosmological structure in the universe after the Big Bang (i.e. inhomogeneities in the matter distribution like galaxies, clusters, super-clusters etc.)

universe,

$$\Omega_{tot} \equiv \Omega_M + \Omega_\Lambda \cong 1 \quad (1.4)$$

corresponding to a flat Universe, while the ratio between the amplitude of the first and the second peak gives

$$\Omega_B \cong 0.045 \quad (1.5)$$

as estimation of the component to the cosmic density associated with the baryonic matter. The observed level of CMB anisotropy provides additional evidence: if there were only baryons, an anisotropy of three order of magnitude larger than that observed would be produced by the primeval inhomogeneity, required to give reason for the structure observed today in the Universe. In other words, the formation of galaxy and clusters can't be explained only by the gravitational collapse of baryonic matter and the current anisotropy data appear to be consistent with the theoretical expectations for Inflation and Dark Matter.

*References:* [2],[3],[12],[13],[14], [15]

## 1.5 COMPOSITION OF THE UNIVERSE

As said before, from the measurement of the CMB's anisotropies it is possible to understand the composition of universe at the moment of decoupling. From the measurement of the position of first acoustic peak many experiments (BOOMERANG, WMAP, MAXIMA) obtained a result consistent with  $\Omega_{tot} = 1$  corresponding to a flat universe and from the ratio between the amplitude of the first and second peak it has been possible to estimate the component to the cosmic density associated with baryonic matter. Primordial nucleosynthesis is one of the three pillars supporting the Big-Bang model for the origin of the Universe. According to the theory, the extremely high temperatures that existed during the earliest moments of the Universe was too hot for nuclei to exist. At very high temperatures, (above a few MeV) nuclei do not exist because the average particle energy is above the nuclear binding energy. At around 1 s the temperature of the Universe cooled to  $10^{10}K$ , and it was possible to have the synthesis of the light elements  $D$ ,  ${}^3He$ ,  ${}^4He$ , and  ${}^7Li$ . In the scenario of standard Big-Bang nucleosynthesis BBN, the primordial abundances of four light isotopes ( $D$ ,  ${}^3He$ ,  ${}^4He$ , and  ${}^7Li$ ) depend only on the baryon-to-photon ratio. Over the past 25 years the big-bang origin of  $D$ ,  $He$  and  $Li$  has been established, not only testing models, but also enabling an accurate determination of the average density of baryons in the Universe. First, it was shown that there is no plausible astrophysical way for the production of deuterium due to its fragility, post big-bang processes only destroy it (nevertheless it is difficult to observe, because, in addition to its low abundance, its emission lines are very close to those of  $H$ , separated only by a small isotopic shift due to the different reduced mass of the atom). Thus, the presently observed deuterium abundance serves as a lower limit to the big-bang production. This argument, together with the strong dependence of big-bang deuterium production on the baryon density, led to the realization that  $D$  is an excellent "baryometer", and early measurements of the deuterium abundance, a few parts in  $10^5$  relative to hydrogen, established that baryons could not contribute more than about 20% of closure density. The baryonic component found  $\Omega_B \cong 0.04 - 0.05$  is in good agreement with CMB measurement and with the local measurement concerning the ratio between dark matter and baryonic matter in the galaxy and in the cluster. Using the astrophysical observations it is possible to estimate both the quantities of bright and dark matter in the Universe. Using the models on the stars' evolution in the galaxies with the known distribution of the light in many types of galaxies, it is possible to evaluate the contribution  $\Omega_l$  of brightening matter and  $\Omega_{DM}$  of dark matter to the cosmic density parameter. The most recent value are

$$\Omega_l \cong 0.005 \quad \Omega_{DM} \cong 0.20 - 0.30$$

From the previous cosmological considerations about the nucleosynthesis of the light elements in the universe and in the analysis on the anisotropy of CMB it is possible to evaluate the contribution  $\Omega_B$  of the baryon to the cosmic density parameter. The resulting value in both the cases is

$$\Omega_B \cong 0.045$$

From these results (and from the previous result about a flat universe with  $\Omega_{tot} \cong 1$ ) it is possible to get many important conclusions:

- most of the baryonic matter (about 90%) is non-luminous
- the baryons account only for a small fraction of the total matter
- the matter is not the main contribution to the cosmic density

Moreover, the contribution  $\Omega_{CMB}$  due to CMB radiation is well known ( $\approx 5 \times 10^{-5}$ ), and it is negligible if compared with the other contributions. Anyway it is possible to suppose the existence of non-baryonic dark matter spread in the cosmic space that would produce another contribution  $\Omega_{DM'}$  to the total galaxies matter  $\Omega_{DM}$ , in such way to have a total density contribution  $\Omega_{DM} + \Omega_{DM'}$ . It is possible to rule out this scenario studying the expansion of the Universe through the use of so-called standard candles, i.e. astronomical objects with uniform peak luminosities (the supernovae Ia belong to this category), so that it is possible to see them at cosmic distances and to determine their distance well. Measurement of the cosmic parameters  $\Omega_\Lambda$  and  $\Omega_M$  through the redshift-distance relation depends on comparing the apparent magnitudes of low-redshift SN Ia with those of their high-redshift cousins. It appears that the expansion rate is accelerating, indicating the existence of *Dark Energy* with negative pressure, and giving another density factor  $\Omega_\Lambda$ . The best-fit results can be approximated by the linear combination

$$\Omega_\Lambda = 1.33\Omega_M + 0.33 \tag{1.6}$$

These values are in excellent agreement with the results discussed above and it is possible to suppose a consistent scenario in which

$$\Omega_\Lambda \cong 0.71 \quad \Omega_M \cong 0.29$$

In particular, all flat model with  $\Omega_M = 1$  models are ruled out at the  $8\sigma$  level, so it is no more necessary to suppose the existence of matter spread in the intergalactic space, and we can assume that all the matter (baryonic and non-baryonic) is related to the galaxies. Although the scenario about the composition of the universe seems to be consistent and well-proved by several independent observations, many questions have no answer yet. In particular the constraint that we have on the baryon density is important because it is very model-independent, and the large discrepancy between

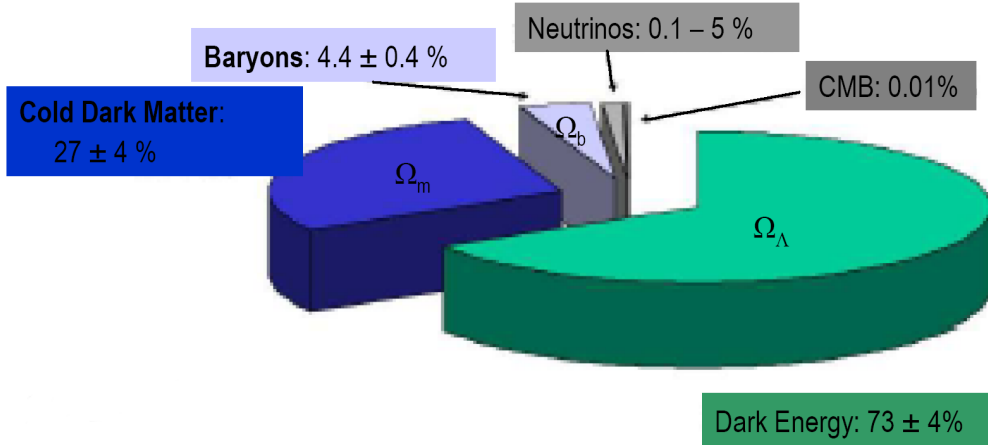


Figure 1.7: Actual composition of the Universe.

the value of  $\Omega_B$  and large-scale measurements of the matter density  $\Omega_M$  indicates a severe need for nonbaryonic dark matter.

*References:* [1],[2],[3],[22]

## 1.6 COLD AND HOT DARK MATTER AND RELIC DENSITY

As we have seen in the previous sections, it is necessary to assume that particles of dark matters are neutral particles with zero baryonic number. During the early moments of the Universe, those particles were at thermal equilibrium with the others and already decoupled to get a significant abundance to satisfy the cosmological requirements ( $\Omega_M \cong 0.3$ ). Let's consider, for example, a species  $\chi$  with a not negligible abundance today in the universe: it is necessary a stable particle or with an average lifetime higher than the age of the Universe. Among the particle dark matter candidates, an important distinction is whether the particles were created thermally in the Early Universe. Thermal and non-thermal relics have a different relationship between their relic abundance and their properties such as mass and couplings, so the distinction is important for dark matter detection. In thermal creation when the Universe was at very high temperature, the dark matter particle  $\chi$  can both annihilate or be formed by reaction like

$$\chi + \bar{\chi} \longleftrightarrow l + \bar{l} \quad (1.7)$$

where  $l$  is a generic particle. At the equilibrium the number of particle is

$$n(t) = \frac{g}{(2\pi)^3} \int f(p, t) d^3p \quad (1.8)$$

where  $g$  is the number of the internal degrees of freedom of  $\chi$  and

$$f(p, t) = \frac{1}{e^{\frac{(E-\mu)}{T} \pm 1}}$$

are the function of Fermi-Dirca (+) and Bose-Einstein(-), and  $\mu$  is the chemical potential. At high temperature ( $T \gg m_\chi$ ) the particle  $\chi$  acts as a relativistic particle  $E^2 = m^2 + p^2$  and assuming that  $T \gg \mu$  it is possible to rewrite  $(E - \mu)/T \cong P/T$ , obtaining

$$n = \frac{g}{(2\pi)^3} \int_0^\infty \frac{p^2}{e^{p/T} \pm 1} \pm 1 \propto \frac{g}{(2\pi)^3} T^3 \quad (1.9)$$

that gives the decreasing like  $T^3$  of the number of particles, thus, as the Universe cooled, the number of particles would decrease together as long as the temperature remained higher than the mass of  $\chi$ . At low temperatures ( $T \ll m_\chi$ )

$$n \cong g \left( \frac{m_\chi T}{2\pi} \right)^{3/2} \exp(-m_\chi/T)$$

so that their density is Boltzmann suppressed. When the temperature finally dropped below the  $m_\chi$  mass, the number density of  $\chi$  drop exponentially together with the probability of a particle to find another to annihilate. The Wimp number density would “freeze-out” at this point and we would be left with a substantial number of particles today. The evolution of the number density of the particles over time is given in detail by the Boltzmann equation

$$\frac{dn_\chi}{dt} + 3Hn_\chi = - \langle \sigma_A v \rangle (n_\chi^2 - (n_\chi^{eq})^2) \quad (1.10)$$

where  $\chi$  denotes the particle,  $H$  is the Hubble constant,  $n_\chi$  is the number-density and  $n_\chi^{eq}$  is the number-density in thermal equilibrium, so the term  $3Hn_\chi$  gives the expansion of the Universe. It is possible to rewrite the Boltzmann equation in a more suitable form using the variables

$$t \rightarrow x \equiv \frac{m}{T}$$

and the co-moving number-density instead of number-density

$$n_\chi \rightarrow Y \equiv \frac{n_\chi}{s}$$

where  $s$  is the entropy density. The parameter  $s$  scales inversely with the volume of the Universe when the entropy is conserved. Defining the total annihilation rate  $\Gamma_A \equiv n_\chi^{eq} \langle \sigma_A |v \rangle$  hence the Boltzmann equation becomes

$$\frac{x}{Y_\chi^{eq}} \frac{dY_\chi}{dx} = - \frac{\Gamma_A}{H} \left[ \left( \frac{Y_\chi}{Y_\chi^{eq}} \right)^2 - 1 \right] \quad (1.11)$$

from which it is evident that the process is dominated by the relationship  $\frac{\Gamma_A}{H}$ , which compares the annihilation rate with the expansion rate. Before freeze out, when the annihilation rate is large compared to the expansion rate,  $Y$  follows its equilibrium value. After freeze-out,  $Y$  became constant depending on the annihilation cross section. The larger the cross section, the longer  $Y$  follows its exponentially falling value at equilibrium so that the relic density assumes lower values. The relic density is inversely proportional to  $\langle \sigma_A v \rangle$ . This is illustrated in fig. (1.8) which shows the variation of the relic density with the annihilation cross section. The annihilation cross section thus informs us about the number density of the particle at freeze out. It is possible now to introduce a distinction between relativistic species and the non relativistic ones. Starting from

$$n_\chi = \frac{g}{2\pi^2} \int_{m_\chi}^{\infty} \frac{(E^2 - m_\chi^2)^{1/2}}{e^{E/T} \pm 1} E dE \quad (1.12)$$

which describes the numerical density at a temperature  $T$  of a species of particles with mass  $m_\chi$ ,  $g$  internal freedom degrees and zero chemical potential can be approximated in different ways, following or not the relativistic condition  $T_c \gg m_\chi$ . Dark matter candidates may be classified as 'hot' or 'cold' based on their energy at the time they de-coupled from the rest of the Universe. If they had been moving at relativistic speeds at that time, they are known as hot. The observations on the present Universe suggest a dark matter being predominantly cold. This is necessary because tiny fluctuations in the matter-density of the very early Universe have evolved into the large scale structure we see today. Anisotropies in the cosmic microwave background radiation, created by the fluctuations in the baryonic matter density, are not enough to create the distribution of matter of the present Universe. Hot dark matter would not be able to assemble into the large scale structure we see today, unless it would have been cold and non relativistic. Only this solution allows the present day structure of the universe without affecting the amplitude of the anisotropies seen in the temperature of the CMB radiation. This suggests that dark matter is mainly cold. It is not possible to solve exactly Boltzmann equation but it possible only to get numerical solutions. The main aspect we want to evidence is that if  $\Gamma_A$  and  $H$  have a dependence from the temperature, called  $T_f$  the decoupling temperature, the decoupling condition is given by

$$\Gamma(T_f) = H(T_f) \quad (1.13)$$

(or  $Hn_\chi = \langle \sigma v \rangle n_\chi^2$ ) which implies that the expansion and the annihilation rates are equal. As the temperature at freeze-out is less than the rest-mass energy of the particle, this implies that  $\chi$  fell out of equilibrium after becoming non-relativistic. For such cold relics, the relic abundance

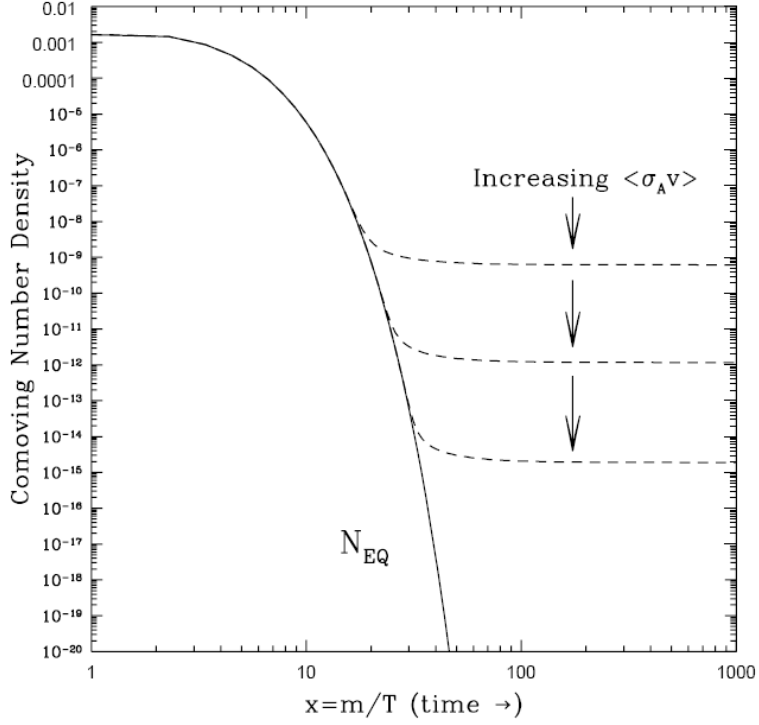


Figure 1.8: Co-moving number density of WIMPs in the early Universe. The solid curve is the equilibrium abundance. The actual abundance (dashed curves) depends on the annihilation cross section.

can be determined from the rate of annihilation at the time of the freeze-out. Resolving the Friedmann equations in a universe ruled by radiation, it is possible to write the Hubble constant as  $H(T) = 1.66g^{1/2} \frac{T^2}{m_{Pl}}$ , where  $m_{Pl} \approx 1.22 \cdot 10^{19} GeV$  is the Planck mass, so we can rewrite the equation (1.13) as

$$n_\chi(T_f) \langle \sigma_A |v\rangle = 1.66g^{1/2} \frac{T_f^2}{m_{Pl}} \quad (1.14)$$

using  $Y_\chi(T_0) = Y_\chi(T_f)$  where  $T_0$  is the actual temperature of the universe ( $2.725K$ ), it is possible to write

$$n_\chi(T_{f0}) = \frac{s(T_0)}{s(T_f)} n_\chi(T_f) \quad (1.15)$$

Considering that  $P = \rho/3$ , and resolving the evolution of from the Friedmann equations is possible to write the actual relic abundance of as

$$\Omega_\chi = \frac{m_\chi n_\chi(T_0)}{\rho_c} = \left( \frac{T_0}{T_f} \right)^3 \frac{1.66m_\chi g^{1/2} T_f^2}{\rho_c m_{pl}} \frac{1}{\langle \sigma_A |v\rangle} \quad (1.16)$$

in which the density  $\rho_\chi$  just the product of the mass  $m_\chi$  and the density number. We are now interested in a cold particle such as a massive particle that was non relativistic at the equilibrium. In this way assuming that the decoupling temperature is one order of magnitude less than the mass  $T_f \sim 10^{-1}m_\chi$  it is possible to rewrite the equation (1.16) as

$$\Omega_\chi = 1.66g^{1/2} \frac{T_0^3}{\rho_c m_{Pl} \langle \sigma_A |v \rangle} \quad (1.17)$$

Thus assuming

$$\begin{aligned} T_0 &= 2.35 \cdot 10^{-4} eV \\ \rho_c &= 1.05 \cdot 10^4 h^2 eV \cdot cm^{-3} \\ m_{Pl} &= 1.22 \cdot 10^{28} eV \\ g^{1/2} &\sim 1 \end{aligned}$$

it is possible to write

$$\Omega_\chi h^2 = \frac{m_\chi n_\chi}{\rho_c} \simeq \frac{3 \cdot 10^{-27} cm^3 s^{-1}}{\langle \sigma_a v \rangle} \quad (1.18)$$

If the cold dark matter in the Universe were made by a stable massive particle, then by Equation (1.18), its annihilation cross section is

$$\langle \sigma_a v \rangle \sim 10^{-27} cm^2 s^{-1} \quad (1.19)$$

when a typical weak interaction cross section is of the order of  $\langle \sigma_a v \rangle \sim 10^{-25} cm^2 s^{-1}$ . This suggests that a particle showing interaction strengths characteristic of the weak force may be a viable dark matter candidate. It must be stressed that no solution to the dark matter problem can be found in the framework of the Standard Model, although a neutrino species with a mass of at least 30 eV could provide the right dark-matter density. In fact the experimental limits on the neutrino mass don't support such values and the measurement done at LEP can exclude any other neutrino's family with  $m_\nu < 45 GeV$ . Moreover, from the N-body simulations of structure formation it can be seen that a neutrino-dominated Universe gives poor results in reproducing the observed structure of the Universe. It appears that some non-baryonic, non-relativistic matter is required in the Universe, and particle physics can provide candidates: any massive and stable particle which annihilates with an electroweak scale cross section is bound to contribute to the dark matter of the Universe. It is interesting that theories such as supersymmetry, invented for entirely different reasons, typically predict just such a particle.

*References::*[1],[4],[11]

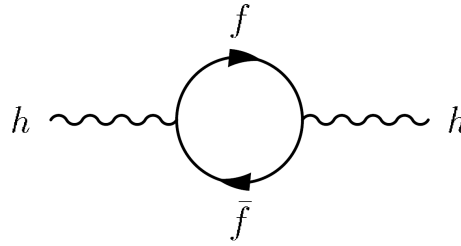


Figure 1.9: A Higgs boson dissociating in two a virtual fermion-antifermion pair

## 1.7 SUPERSYMMETRIC EXTENSION OF THE STANDARD MODEL

The Standard Model agrees with experimental data. There are several different parameters describing the model, but many of them cannot be predicted a priori, and must be measured. Among them, the masses of the particles and the coupling strengths of the forces must be included. One of the major aim of the physicist has been always to show that all four forces of nature can be derived from a single force, in such a way that the forces that we see are low-energy approximations to this single force, in the same way as the electromagnetic force and the weak force are two aspect of the electroweak force. In the process of unifying these two forces, the Higgs boson ( $h^0$ ) had to be introduced. This boson gives masses to all the particles, but it is the only one in the Standard Model that hasn't been observed yet experimentally. One of the biggest problem with the Higgs framework to give the mass to all the particles is the Higgs divergence problem. Figure (1.9) shows a Feynman diagram involving a Higgs boson: this diagram is one of many that contributes to the Higgs boson's own mass. There are infinitely many such diagrams, involving more than one such fermion loop, and, calculating the correction to the Higgs mass due to such loops, divergences to infinity are obtained. In the framework of the Supersymmetry it is possible to solve this problem. It is necessary to assume that for every Standard Model particle there is a corresponding supersymmetric particle (or "sparticle") which has a spin that is different by  $1/2$  unit. The existence of particles with exactly the same properties as the Standard Model particles (except for different spins) helps to solve the mentioned divergence problem. The main problem on the way of a global theory is that the graviton has spin 2, while the other gauge bosons (photon, gluons, W and Z weak bosons) have spin 1, so corresponding to different representations of the Poincaré algebra. Due to no-go theorems, unification of spin 2 and spin 1 gauge fields within a unique

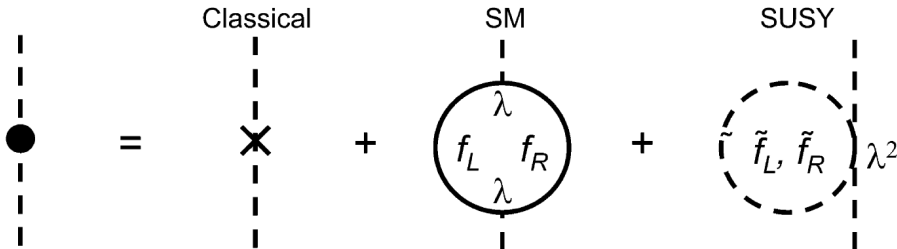


Figure 1.10: Contributions to the Higgs boson mass in the Standard Model and in Supersymmetry

algebra is forbidden, except for the supersymmetry algebra. This is a strict mathematical statement, saying that algebra of SUSY is the only graded (i.e. containing anticommutators as well as commutators) Lie algebra possible within relativistic field theory. The basic prediction of supersymmetry is, then, that for every known particle there is another particle, its superpartner, with spin differing by 1/2. If  $Q$  is a generator of SUSY algebra, then

$$Q|boson \rangle = |fermion \rangle \quad \text{and} \quad Q|fermion \rangle = |boson \rangle \quad (1.20)$$

According with this assumption, for every diagram like Fig (1.9) there is a diagram that looks like Fig.(1.10). The interesting thing is that in this way both the diagrams have the same vertices and coupling constants, producing an amplitude of the same magnitude. The standard sign of fermion loops in field theory is opposite to that of boson loops, so if standard particles and super-particle have the same masses, when the cross section is calculated, those contributions are cancelled. Thus in the framework of the Supersymmetry it is possible to get a mechanism able to produce a finite interaction probability. We know that supersymmetry cannot be an exact symmetry, in this case the sparticle would have exactly the same mass of the particle and many of them would have been already seen. In detail the mass of the Higgs boson  $m_h$  receives quantum corrections

$$m_h^2 = (m_h^2)_0 - \frac{1}{16\pi^2} \lambda^2 \Lambda^2 + \dots \quad (1.21)$$

where the last term in (1.21) is the leading quantum correction, with  $\lambda$  the Higgs-fermion coupling.  $\Lambda$  is the ultraviolet cutoff of the loop integral, presumably some high scale well above the weak scale. If  $\Lambda$  is of the order of the Planck scale ( $10^{19}$  GeV), the classical Higgs mass and its quantum correction must be eliminated to an 1 part in  $10^{34}$  to produce the required weak-scale

$m_h$ . This unnatural fine-tuning is the gauge hierarchy problem. In the supersymmetric standard model, however, for every quantum correction with standard model fermions  $f_L$  and  $f_R$  in the loop, there are corresponding quantum corrections with superpartners  $\tilde{f}_l$  and  $\tilde{f}_r$ . The physical Higgs mass then becomes

$$m_h^2 = (m_h^2)_0 - \frac{1}{16\pi^2}\lambda^2\Lambda^2 + \frac{1}{16\pi^2}\lambda^2\Lambda^2 + \dots \cong (m_h^2)_0 + \frac{1}{16\pi^2}(m_{\tilde{f}}^2 - m_f^2)\ln\left(\frac{\Lambda}{m_{\tilde{f}}}\right) \quad (1.22)$$

where the terms quadratic in  $\Lambda$  cancel, leaving a term logarithmic in  $\Lambda$  as the leading contribution. In this case, for a large range of  $\Lambda$ , it is possible to get quantum correction and it not requested an unnatural fine-tuning. In the case of exact supersymmetry, where  $m_f = m_{\tilde{f}}$ , even the logarithmically divergent term vanishes. Nevertheless, to solve the gauge hierarchy problem, it is not needed an exact mass degeneracy, but it is necessary the identity of the dimensionless couplings  $\Lambda$  of standard model particles and their superpartners. Moreover, not to make the logarithmically term divergent, superpartner masses are required to be not too different from the weak scale. It is possible to get this conditions by adding supersymmetry-breaking weak-scale masses for superpartners: if supersymmetry is broken, the sparticles may have much greater masses than ordinary particles. Moreover, if their mass is not very large, such mentioned corrections can eliminate the hierarchy problem (masses less than about 1 TeV in order to work the cancellation of Fig. 1.10)

*References:*[1],[16],[17],[18],[19]

### 1.7.1 GUT

Although it was not proposed to this aim, Supersymmetry plays a crucial role in the effort of the physicist to find a general theory of the interactions. The main idea of Grand Unification is that all known interactions are different branches of a unique interaction associated with a simple gauge group. So the basic assumption is that gauge symmetry increases with energy. The unification occurs at high energy, because at low energy it is impossible, due to a big difference in the values of the couplings of strong, weak and electromagnetic interactions. The crucial point here is the running coupling constants, i.e. the dependence of the couplings by a distance or an energy scale

$$\alpha_i = \alpha_i\left(\frac{Q^2}{\Lambda^2}\right) = \alpha_i(\text{distance}), \quad \alpha_i \equiv \frac{g_i^2}{4\pi} \quad (1.23)$$

This dependence, confirmed experimentally, is described by the renormalization group equations. In the SM the strong and weak couplings are associated with non-Abelian gauge groups, while the electromagnetic one is associated with the Abelian group. In this way we have the increasing

Low energy			⇒	High energy
$SU_c(3) \otimes$	$SU_L(2) \otimes$	$U_Y(1)$	⇒	$G_{GUT}$ (or $G^n +$ discrete symmetry)
gluons	$W, Z$	photon	⇒	gauge bosons
quarks	leptons		⇒	fermions
$g_3$	$g_2$	$g_1$	⇒	$g_{GUT}$

Figure 1.11: Basic assumption of the GUT theory: all known interactions are different branches of a unique interaction associated with a simple gauge group and the unification can occur at high energy.

of the weak and strong couplings with the increase of the energy and the decreasing of the electromagnetic one. It would be natural to investigate the possibility that at some energy scale they become equal. This equality would be the confirmation of a unique origin of these three interactions. The unique interaction would be divided into three different aspects as a result of spontaneous symmetry breaking. This happens at a very high energy (of an order of  $10^{15} - 10^{16} Gev$ ) outside of the range of accelerators. However, it is possible to check this hypothesis numerically. The three coupling constants to be compared are

$$\alpha_1 = (5/3) \frac{g'^2}{4\pi} = \frac{5\alpha}{3 \cos^2 \theta_W}$$

$$\alpha_2 = \frac{g^2}{4\pi} = \frac{\alpha}{\sin^2 \theta_W}$$

$$\alpha_3 = \frac{g_s^2}{4\pi}$$

where  $g'$ ,  $g$  and  $g_s$  are the usual  $U(1)$ ,  $SU(2)$  and  $SU(3)$  coupling constants and  $\alpha$  is the fine structure constant<sup>2</sup>. If we assume that the SM is valid without any correction up to the unification scale, it is possible to use the renormalization equations for the three couplings, which can describe the running of the coupling. Saying  $\tilde{\alpha}_i = \alpha_i/4\pi$  the equations are

$$\frac{d\tilde{\alpha}_i}{dt} = b_i \tilde{\alpha}_i \quad t = \log \frac{Q^2}{\mu^2} \quad (1.24)$$

where  $\mu$  is an energy parameter, typically assumed as  $Z^0$  mass. Thus, using the averaged values of the couplings at the  $Z^0$  energy (obtained from a fit to the LEP and Tevatron data)

$$(\alpha_1(M_Z), \alpha_2(M_Z), \alpha_3(M_Z)) = (0.017, 0.034, 0.118)$$

---

<sup>2</sup>the factor of 5/3 in the definition of  $\alpha_1$  has been included for proper normalization of the generators

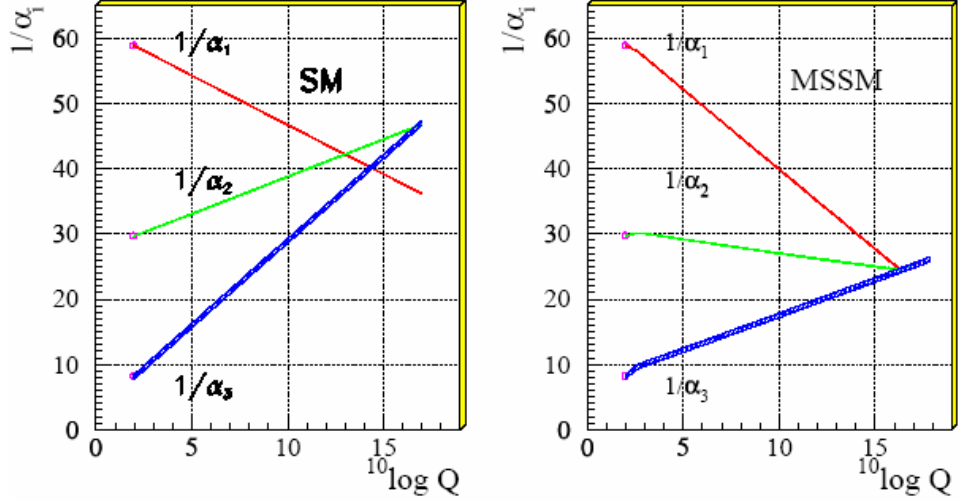


Figure 1.12: Evolution of the inverse of the three coupling constants in the Standard Model (left) and in MSSM (right). The SUSY particles are assumed to contribute only above the effective SUSY scale of about  $1\text{TeV}$ , which causes a change in the slope in the evolution of couplings. The thickness of the lines represents the error in the coupling constants.

and the coefficient <sup>3</sup>  $b_i = (41/10, -19/6, -7)$  the solution to eq. (1.24)

$$\frac{1}{\tilde{\alpha}_i(Q^2)} = \frac{1}{\tilde{\alpha}_i(\mu^2)} - b_i \log \left( \frac{Q^2}{\mu^2} \right) \quad (1.25)$$

is reported in Fig.(1.12) as the evolution of the inverse of the couplings as function of the logarithm of energy. At the first order we have straight line, the second order corrections are small and do not cause any visible deviation. It is evident that within the SM the coupling constants unification at a single point is excluded by more than 8 standard deviations, so that the unification can only be obtained if new physics enters between the electroweak and the Planck scales.

The starting point is that we do not know what kind of new physics it may be, having in this way a lot of arbitrariness and allowing to solve the problem within a supersymmetric generalization of the SM. In the SUSY case, the slopes of the RG evolution curves are modified. The coefficients  $b_i$  in eq. (1.25) now change ( $b_i = (33/5, 1, -3)$ ), and a perfect unification can be obtained if the SUSY masses are of an order of 1 TeV. The SUSY particles are assumed to effectively contribute to the running of the coupling

<sup>3</sup>the  $b_i$  coefficient are obtained in the framework of the Standard Model with  $N_{fam} = 3$  (number of matter multiplets) and  $N_{Higgs} = 1$  (number of Higgs doublets)

constants only for energies above the typical SUSY mass scale. At energies above 1TeV we have a change in the slope of the lines. Requiring unification it is possible to find the break point  $M_{SUSY}$  and the unification point  $M_{GUT}$

$$\begin{aligned} M_{SUSY} &= 10^{3.4 \pm 0.9 \pm 0.4} GeV \\ M_{GUT} &= 10^{15.8 \pm 0.3 \pm 0.1} GeV \\ \alpha_{SUSY}^{-1} &= 26.3 \pm 1.9 \pm 1.0 \end{aligned}$$

where the first error originates from the uncertainty in the coupling constants, while the second one is due to the uncertainty in the mass splittings between the SUSY particles. The importance of this observation lies in the fact that MSUSY should be in the range preferred by the fine-tuning arguments. It should be noted that introducing new particles and three free parameters (MSUSY, MGUT and GUT) all three curves are simultaneously influenced, due to the strong correlations between the slopes and the fact that it is possible to get the unification of the three curves at a single point is an important evidence.

*References:*[17],[18],[19],[20],[21]

## 1.7.2 SUPERPARTICLES

It could be shown that no particle of the standard model is the superpartner of another. Once supersymmetry is broken, the theory predicts **new particles** not discovered yet, with a different range of mass. The gauge hierarchy problem gives a strong motivation for this scale to be the weak scale. In the standard model there are already 18 experimentally accessible parameters (6 quark masses, 3 lepton masses, 4 parameters in the Cabibbo-Kobayashi-Maskawa matrix, 3 gauge couplings, the W-boson mass, and Higgsboson mass). In supersymmetry, there is a fermionic degree of freedom for every bosonic degree of freedom and vice versa, so the particle spectrum is greatly extended and there are many new parameters. Even in the minimal supersymmetry extension of the standard model MSSM, the minimum number of parameters is 63. It is easy to understand that for each "normal" degree of freedom, there is a supersymmetric degree of freedom. For example standard quarks have spin 1/2, while squarks are scalars, therefore, there are two squarks (left and right) for each quark. Supersymmetric particles that are electrically neutral, and so promising as dark matter candidates, are shown with their standard model partners in fig.(1.13). The superpartner spectrum of the standard spectrum is easy to represent. The only remarkable detail is that in supersymmetric models, two Higgs doublets are required to give mass to all fermions. The spectrum consists of spin 0 sneutrinos, one for each neutrino, the spin 3/2 gravitino, and the spin 1/2 Bino, neutral Wino, and down- and up-type Higgsinos. In the top row of fig.(1.13) the mass parameters ( $M_1, M_2, \mu, m_\nu$  and  $m_{3/2}$ ) that determine the masses of the gauge eigenstates are reported. These parameters are of the order

Spin	U(1) $M_1$	SU(2) $M_2$	Down-type $\mu$	Up-type $\mu$	$m_{\tilde{\nu}}$	$m_{3/2}$
2						G graviton
3/2						$\tilde{G}$ gravitino
1	B	$W^0$				
1/2	$\tilde{B}$ Bino	$\tilde{W}^0$ Wino	$\tilde{H}_d$ Higgsino	$\tilde{H}_u$ Higgsino	$\nu$	
0			$H_d$	$H_u$	$\tilde{\nu}$ sneutrino	

Figure 1.13: Neutral particles in the SUSY spectrum.  $M_1, M_2, \mu,$  and  $m_{3/2}$  are unknown weak-scale mass parameters. The Bino, Wino and down and up type Higgsinos mix to form neutralinos

of the weak scale, as described previously. The gauge eigenstates can mix to form mass eigenstates using the electroweak symmetry breaking. In the basis  $(-i\tilde{B}, -i\tilde{W}, \tilde{H}_d, \tilde{H}_u)$  the mixing matrix is

$$M_\chi = \begin{pmatrix} M_1 & 0 & -M_2 \cos\beta s_W & M_2 \sin\beta s_W \\ 0 & M_2 & M_2 \cos\beta c_W & -M_2 \sin\beta c_W \\ -M_2 \cos\beta s_W & M_2 \cos\beta c_W & 0 & -\mu \\ M_2 \sin\beta s_W & -M_2 \sin\beta c_W & -\mu & 0 \end{pmatrix}$$

where  $c_W = \cos\theta_W$ ,  $s_W = \sin\theta_W$ , and  $\beta$  is another unknown parameter defined by the ratio of the up-type to down-type Higgs scalar vacuum  $(\tan\beta = \langle H_u \rangle / \langle H_d \rangle)$ .

The mass eigenstates are called neutralinos and denoted  $\chi = (\chi_1, \chi_2, \chi_3, \chi_4)$ , in order of increasing mass. It is possible that the lightest neutralino is a pure Bino (in the case of  $M_1 \ll M_2$  and  $M_1 \ll |\mu|$ ) with a mass of approximately  $M_1$ , or it is an effective mixture of each gauge eigenstate (for  $M_1 \cong M_2 \cong |\mu|$ ). The last observation is that neutralinos are Majorana fermions, so they are their own anti-particles. This is an interesting observation for a possible identification of the neutralino as the candidate particle for the Dark Matter.

References: [1], [16] [18], [19]

### 1.7.3 R-PARITY

As it has been discussed above, the hypothesis of the existence of weak-scale superpartners gives the possibility to solve the gauge hierarchy problem through their virtual effects. Anyway, some additional assumptions are

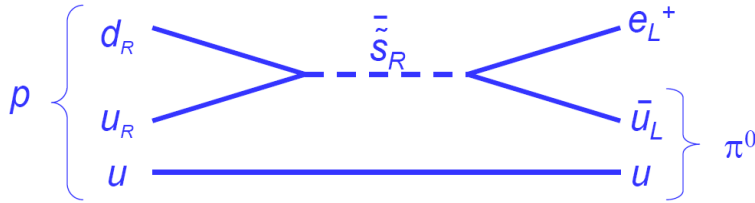


Figure 1.14: Example of a possible proton decay mediated by squark

necessary in order to prevent effects like the violation of the baryonic and leptonic number at an unneeded level . For example, in the proton decay the reaction  $p \longrightarrow \pi^0 e^+$  may be mediated by a squark as shown in fig.(1.14) . It is possible to assume a conservation law to forbid this type of decay. In this case we define the R-parity as

$$R_p = (-1)^{3(B-L)+2S}$$

where B, L, and S are baryon number, lepton number, and spin, respectively, in such a way that all standard model particles have  $R_p = 1$ , and all superpartners have  $R_p = -1$ . The conservation of the R- parity implies

$$\prod R_p = 1 \tag{1.26}$$

at each vertex, making impossible the previous decay because both vertices are forbidden. The R-parity conservation is something more than a theoretical invention. Although it is possible to avoid the proton decay without R-parity (for example by assuming the B or L violation but not both), many other processes will require some different explanation ad hoc. An immediate consequence of R-parity conservation is that any decay of the lightest supersymmetric particle would violate the R-parity conservation: therefore, the lightest supersymmetric particle (LSP) must be stable. Actually there are many supersymmetric extensions of the standard model, providing different candidates for the LSP. In the framework of the so-called minimal supersymmetric extension of the Standard Model (MSSM), the LSP is identified as "neutralino" , a linear superposition of different supersymmetric particles. Although there are uncertainty about the identity of what is known as LSP (and about its attributes), the main result we are interested in is that a natural extension of the Standard Model naturally suggests a symmetry that provides a new stable particle that may play a role at cosmological level. Thus Particle Physics could give a solution to the dark matter problem.

*References::*[1],[16]

## 1.8 THE GALACTIC DARK HALO

Due to the fact that the Earth is moving in the Milky Way with the Sun, at a distance of  $r_0 \cong 8.5kpc$  from the Sun to the Galactic centre, the knowledge of the Milky Way's dark halo has great importance for Dark Matter searches. The halo model, the local dark-matter density  $\rho_0 = \rho(r_0)$  and the mean dispersion speed  $\bar{v} = \langle v^2 \rangle^{1/2}$  play a crucial role in both direct and indirect Dark Matter detection methods. The most important information about the local halo density can be given by the rotation curve that is related to the total gravitational potential and so includes contributions from all the matter. The visible structure of spiral galaxies is dominated by a luminous disk of stars exponential in radius ( $I(r) = I_0 \exp(-r/r_d)$ ), where the disk radius  $r_d$  defines the scale of the disk ( $r_d \approx r_{ott}/3$ ). Spiral galaxies can also have a bulge-like component at the center (size of order  $1kpc$  or less), but its contribution to the gravitational potential is typically negligible beyond the luminous regions. The experimental observations suggest that dark matter dominates at large radii, but possesses flat core profiles so that dark and luminous matter give similar contributions inside the luminous regions. For example, considering the contribution of the stellar disk and dark halo (the most important mass components of the Galaxy), the total rotation speed is,

$$v_{tot} = [v_d^2(r) + v_h^2(r)]^{1/2}$$

where  $v_d$  is the disk contribution,  $v_h$  is the halo contribution, and  $r$  is the distance to the centre of the Galaxy in the plane of the disk. Assuming a phenomenological form of halo's mass density distribution and using free parameters ( $\alpha, \beta, \gamma$ ), it is possible to write a general density behavior like

$$\rho(r) \propto \frac{\rho_0}{(r/a)^\gamma [1+(r/a)^\alpha]^{[\beta-\alpha]/\alpha}}$$

where  $a$  is a parameter related to the core radius of the halo. As a function of ( $\alpha, \beta, \gamma$ ) this family of curves can define many possible shapes able to reproduce the observed rotation curves of most galaxies over a large range of radii (with quite different behaviors at very small or very large radii). A general and commonly used model for the halo is the cored spherical isothermal halo ( $\alpha, \beta, \gamma$ ) = (2, 2, 0) given assuming a system of particles of mass  $m$  interacting gravitationally at thermal equilibrium with a temperature  $T$ . It is possible to write the cored spherical isothermal halo for the Milky Way as

$$\rho(r) = \rho_0 \frac{a^2 + r_0^2}{a^2 + r^2}$$

where  $a$  is the core radius of the halo, producing flat rotation curves at large radii. The density and velocity distributions are related since the

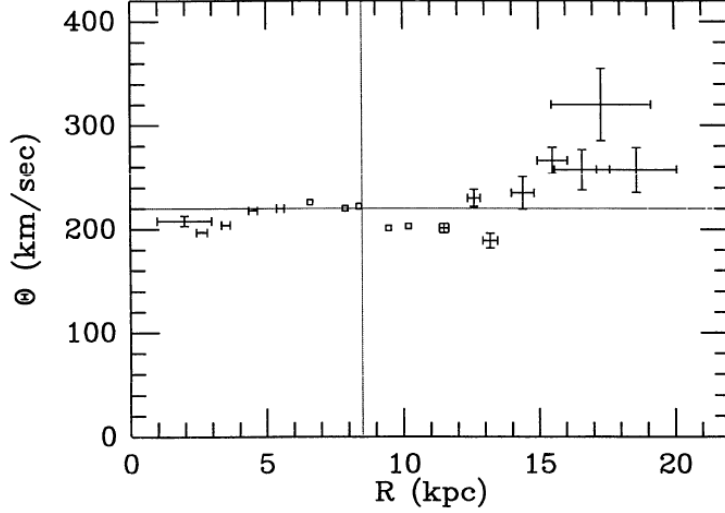


Figure 1.15: Measured rotation speed obtained by the average value of measurements on different objects between 5 and 20 kpc in the Milky Way.

phase-space distribution must satisfy Jeans equation, and the possible local velocity distribution in this model is Maxwellian

$$f_v d^3v = \frac{e^{-v^2/v_0}}{\pi^{3/2}v_0^3} d^3v \quad (1.27)$$

where it could be shown that the constant  $v_0$  is equal to the circular rotation velocity as  $r \rightarrow \infty$ . The exact solution for the density distribution for the cored spherical isothermal halo can be obtained numerically. According to this model, the rotation speed due to the halo alone is

$$v_h^2(r) = 4\pi G\rho_0(r_0^2 + a^2)\left(1 - \frac{a}{r}\tan^{-1}\frac{r}{a}\right) \quad (1.28)$$

According to the supposition of an exponentially drop of the stellar disk density at distances much larger than the disk dimension, the total speed should be due to the only contribution of the halo. Thus defining  $v_\infty$  as the circular rotation velocity for  $r \rightarrow \infty$ , at very large radii the identity  $v_{tot}(\infty) = v_h(\infty) = v_\infty$  is obtained. Starting from the previous equations it is possible to calculate the rotation velocity due to the halo at a distance equal to the solar circle radius, obtaining

$$\frac{a}{r_0}\tan^{-1}\frac{r_0}{a} = 1 - \frac{v_h^2(r_0)}{v_\infty^2} \quad (1.29)$$

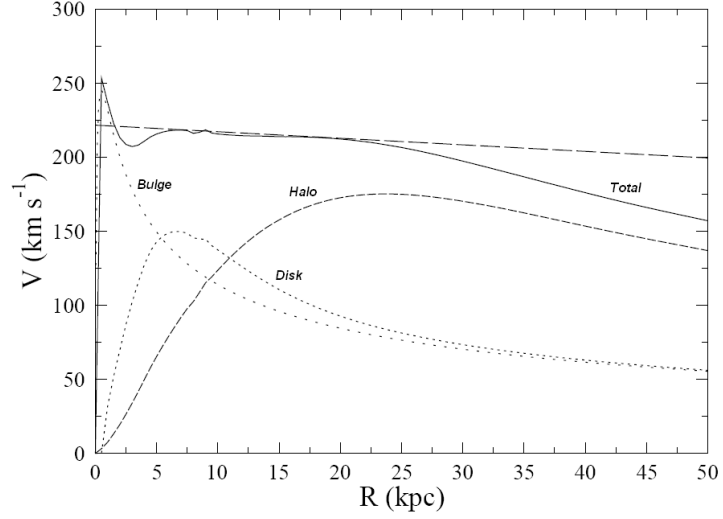


Figure 1.16: Possible different components (bulge,disk and halo) needed to reproduce the observed curves between 5 and 20 kpc in the Milky Way.

It is so possible to calculate the ratio  $a/r_0$  and  $\frac{v_h^2(r_0)}{v_\infty^2}$ . The local halo density can be written as

$$\rho_0 = \frac{v_\infty^2}{4\pi G r_0^2 [1 + (a/r_0)^2]} \quad (1.30)$$

so it's clear the dependency of  $\rho_0$  by  $a$ ,  $r_0$  and  $v_\infty$ . It should be noted that,  $v_\infty$  is an unknown parameter because the rotation speed at  $r \rightarrow \infty$  cannot really be measured. Assuming  $v_\infty = 230(\text{km} \cdot \text{s}^{-1})$  and  $a = 4.8\text{kpc}$  for the Milky Way (fig 1.15), equation (1.30) implies a local matter density such as

$$\rho_0 \cong 0.3\text{GeV}c^2\text{cm}^{-3} \quad (1.31)$$

References:: [1],[4],[2],[10],[5]

## Chapter 2

# WIMP direct detection

### 2.1 INTRODUCTION

As it has been stated in the last chapter, there are many experimental observations suggesting that the largest part of the matter of the Universe should consist in weakly interacting, non-barionic, massive and stable particles called WIMPs. WIMPs should be gravitationally trapped inside the galaxy and could have the adequate density profile to account for the observed rotational curves. Their mean velocity inside our galaxy is expected to be of the order of  $10^2 km/s$ , similar to the speed of the sun around the center of the Milky Way, and it should be possible to detect WIMPs by elastic scattering off the nucleus of ordinary matter ("direct detection"). At those velocities, WIMPs should produce a typical nuclear recoil energies in the range  $1 \div 100 keV$  (supposing a WIMP mass in the range  $10 GeV \div 1 TeV$ ). These constraints determine the main features of the direct experimental detection of WIMPs. Moreover, the shape of the recoil spectrum and the expected interaction rate have a fundamental meaning for this type of research.

In this chapter those theoretical predictions are discussed, together with the main experimental techniques used in the direct search and a review of some fundamental experiments. Finally a really brief discussion about indirect detection methods and their results is reported.

### 2.2 EXPECTED RECOIL SPECTRUM AND INTERACTION RATE

As stressed before, it is possible to detect WIMPs in a direct or indirect way. In the first case, the estimation of the expected spectrum has a crucial role together with the interaction of WIMPs with ordinary matter. The rate of such collisions depends on the local WIMP density  $\rho_\chi$  and their kinetic energy distribution. Due to the infinite range of the gravitational force, the number of particles to be considered is large and it is not so easy to calculate the

kinetic energy distribution. Anyway, as we have seen in the last chapter, the most common assumption is a spherical halo in which the WIMPs are trapped in the gravitation field at thermal equilibrium with a Maxwellian velocity distribution  $f(\vec{r}, \vec{v}, \vec{v}_E, v_{esc})$  like:

$$f(\vec{r}, \vec{v}, \vec{v}_E, v_{esc}) \sim e^{-\frac{(\vec{v} + \vec{v}_E)^2}{v_0^2}} \quad (2.1)$$

where  $\vec{v}$  is the WIMP velocity respect to the earth and  $\vec{v}_E$  is the total velocity of the Earth with respect to the centre of the galaxy (taking in account the Sun's speed),  $v_0 \approx 230 km s^{-1}$  and  $v_{esc}$  is the escape velocity from the Milky Way. The above distribution is clearly true for each value of  $\vec{v}$  such that  $|\vec{v} + \vec{v}_E| < v_{esc}$ . According to this assumption, if  $M_\chi$  and  $T$  are the WIMP mass and the equivalent temperature, it is possible to assume an abundance  $f(\vec{r}, \vec{v}, \vec{v}_E)$  that follows a Boltzmann distribution:

$$f(\vec{r}, \vec{v}, \vec{v}_E) \sim e^{-\frac{-M_\chi(\vec{v}_E + \vec{v})^2 + M_\chi\Phi(\vec{r})}{k_B T}} \quad (2.2)$$

where  $k_B T = M_\chi v_0^2$  and  $\Phi$  is the local gravitational potential. We are now interested in the estimation of the recoil energy spectrum that can give fundamental information about both the cross section neutralino-nucleus  $\sigma_{\chi-N}$  and the mass  $M_\chi$ . If  $n$  is the number density of WIMPs, the rate of interaction on a target of atomic mass  $A$  per unit of mass is dependent on the cross section, thus

$$R = \frac{N_0}{A} \int \sigma_{\chi-N} v dn \quad (2.3)$$

where  $N_0$  is the Avogadro number,  $v$  is the velocity's module of the impinging particles and  $dn$  is the density of particle with module of velocity within  $[\vec{v} - d\vec{v}; \vec{v} + d\vec{v}]$  that can be written in terms of the velocity distribution  $f(\vec{r}, \vec{v}, \vec{v}_E, v_{esc})$

$$dn = \frac{n_0}{k} f(\vec{r}, \vec{v}, \vec{v}_E, v_{esc}) d^3v$$

with  $n_0 = \frac{\rho_\chi}{M_\chi}$  ( $\rho_\chi \cong 0.3 GeV cm^{-3}$ ) and  $k$  a normalization constant such as  $\int_0^{v_{esc}} dn = n_0$ . Thus, assuming a constant cross section  $\sigma_0$  in the zero moment transfer approximation, we obtain

$$R = \frac{N_0}{A} \sigma_0 \int v dn = \frac{N_0}{A} \sigma_0 n_0 \langle v \rangle \quad (2.4)$$

and

$$dR = \frac{N_0}{A} \sigma_0 v dn \quad (2.5)$$

It is useful to define the total event rate  $R_0$  per unit of mass assuming  $v_E = 0$  and  $v_{esc} = \infty$ .

$$R_0 = \frac{2}{\pi^{1/2}} \frac{N_0}{A} n_0 v_0 \sigma_0 \quad (2.6)$$

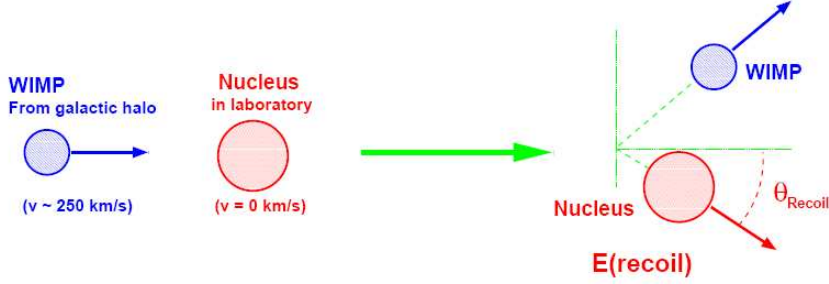


Figure 2.1: Kinematics of a WIMP-nucleus collision.

Supposing an elastic scattering off a nucleus of mass  $M_T$  of ordinary matter, the energy of the recoiled nucleus at an angle  $\theta$  (2.1) is given by:

$$E_R = E \frac{4M_\chi M_N}{(M_\chi + M_N)^2} \frac{(1 - \cos\theta)}{2} \quad (2.7)$$

so the maximal recoil energy is obtained when  $M_\chi = M_N$ . Assuming an uniform  $E_R$  distribution (hard sphere scattering model)<sup>1</sup> it is possible to write the differential interaction rate as:

$$\frac{\partial R}{\partial E_R} = \frac{R_0}{E_0 r} \frac{2\pi^{3/2} v_0}{k} \int_{v_{min}}^{v_{max}} v e^{-\frac{(\vec{v} + \vec{v}_E)^2}{v_0^2}} dv \quad (2.8)$$

where

$r = \frac{4M_\chi M_N}{(M_\chi + M_N)^2}$  is a kinematic factor,

$R_0 \sim (n_0 v_0 \sigma_0)$  is the total rate event per unit of mass,

$E_0 = k_B T$  is the most probable incident kinetic energy ,

$k$  is a normalization factor and

$v_{min}$  and  $v_{max}$  are respectively the minimum speed necessary to produce a recoil of  $E_R$  and the galactic escape velocity ( $v_{max} = v_{esc}$ ).

Assuming the limit conditions ( $v_{min} = 0$  and  $v_{esc} = \infty$ ), the eq. (2.8) gives the shape

$$\frac{\partial R(0, \infty)}{\partial E_R} = \frac{R_0}{E_0 r} e^{-\frac{E_R}{E_0 r}} \quad (2.9)$$

Thus, according with our assumption, the recoil energy spectrum has an exponential behavior and using the amplitude and the shape of the recoil energy spectrum, it is possible to constrain two physically important parameters:  $M_\chi$  and  $\sigma_{\chi-N}$ . Moreover, since the Galactic velocities are of the

<sup>1</sup>We assume the scattering is isotropic, i.e. uniform in  $\cos\theta$ , so the recoils are uniformly distributed in  $E_R$  over the range  $0 \leq E_R \leq Er$

order of  $10^2 km/s$ , values of  $M_\chi$  in the range  $10 \div 1000 GeV/c^2$  would produce recoil energies in the range  $10 \div 100 keV$ .

For practical purpose, assuming  $v_0 = 230 km s^{-1}$  and  $v_{esc} = 600 km s^{-1}$  the cut off for  $v_{esc}$  has a negligible effect, while the minimum speed  $v_{min}$  has the Earth speed (i.e. the speed of the target) as lower limit. Assuming in this way  $v_{min} = v_E$  and  $v_{max} = \infty$ , the previous formula can be generalized as

$$\frac{\partial R(v_E, \infty)}{\partial E_R} = c_1 \frac{R_0}{E_0 r} e^{-\frac{c_2 E_R}{E_0 r}} \quad (2.10)$$

where the constant  $c_i$  depend on the time of the year <sup>2</sup>. The differential interaction rate is conventionally expressed in units of  $(keV^{-1} kg^{-1} day^{-1})$  or "differential rate unit" (dru). It could be useful for some experiments to evaluate a limit on the total number of events in a finite energy range. Integrating the eq. (2.10) between two different values  $(E_1, E_2)$  of  $E_R$  we obtain

$$R(E_1, E_2) = R_0 \frac{c_1}{c_2} \left[ e^{c_2 E_1 / E_0 r} - e^{c_2 E_2 / E_0 r} \right] \quad (2.11)$$

The total rate obtained by the integration over the energy is so expressed as  $(events \cdot kg^{-1} \cdot day^{-1})$  or "total rate unit" (*tru*), while the partial integral of the differential spectrum between two different values is defined in terms of "integrated rate unit" (*iru*) (reserving "tru" specifically for the total integral  $E_1 = 0$  and  $E_2 = \infty$ ). As stated before, the total rate  $R_0$  is defined as the time independent rate corresponding to zero Galactic speed ( $v_E = 0$ ).

The time dependence is due to the different values assumed during the year by  $\vec{v}_E$ . If  $\vec{v}_E$  is the speed of the Earth in the galactic frame, its value is just the sum of the three different components due to the rotational speed of the galaxy disk  $\vec{v}_d$ , the Sun motion respect to the disk (i.e. its mean motion relative to nearby stars)  $\vec{v}_s$  and finally the rotational speed of the Earth around the Sun  $\vec{v}_e$ . Thus

$$\vec{v}_E = \vec{v}_d + \vec{v}_s + \vec{v}_e. \quad (2.12)$$

The tangential velocity of the sun around the galactic center (in the direction of Sagittarius) is  $230 km/s$  and is the dominant contribution. The earth velocity is an order of magnitude smaller ( $30 km/s$ ) and can generally be neglected, except for an interesting modulation effect in the flux. As the earth orbits around the sun with a  $60^\circ$  angle relative to the galactic plane, a  $v_e \times \cos(60^\circ) = 15 km/s$  velocity component is alternatively added and subtracted to the sun's velocity relative to the WIMP flux. According to the experimental results it is possible to write

$$\vec{v}_E = \left[ 244 + 15 \cos \left( 2\pi \frac{t - 152.3}{365.25} \right) \right] km/s \quad (2.13)$$

---

<sup>2</sup> $c_1, c_2$  are not independent, by integration we obtain  $\frac{c_1}{c_2} = \frac{R}{R_0}$ . For most purpose it could be useful to take fixed average values  $c_1 = 0.751$  and  $c_2 = 0.561$

where  $t$  is the number (real) of days since 00:00 of January, 1<sup>st</sup> of each year. In this way the net effect is to enhance the average kinetic energy of the WIMP flux on earth at 1st of June and to decrease at 1st of December. This may result in a 7% annual modulation of the collision rate that can give an interesting experimental signature of the detected signal (although the exact size of the effect may depend on the details of the halo models).

This scheme of the elastic scattering has to be modified to consider the case of a large momentum transfer  $q = (2M_T E_R)^{1/2}$  : in this case the wavelength could be comparable with the nuclear's typical dimension. The wavelength associated to the momentum transfer of 20 keV of kinetic energy is approximately 3 fm (about the size of the entire nucleus). It is not possible to assume a priori that the scattering cross-section on a nucleus has a scaling so that the contribution of various nucleons will be added coherently. In the first case only the unpaired nucleon will have a considerable contribution to the interaction, while in the last case all nucleon contributions add coherently giving a cross-section scaling. Thus, some assumptions about a spin-dependent or scalar (spin independent) interaction have to be made and a multiplicative form factor  $F(q)$  which depends on the type of WIMP-nucleon interaction (spin-dependent or spin-independent) has to be included. In general the differential cross-section of the scattering can be written as function of the momentum transfer  $\vec{q}$  as  $\sigma(q^2) = \sigma_0 F^2(q^2)$  or

$$\frac{d\sigma_{\chi-N}}{d|\vec{q}|^2} = G_F^2 \frac{C}{v^2} F^2(|\vec{q}|) = \frac{\sigma_0}{4\mu^2 v^2} F^2(|\vec{q}|) \quad (2.14)$$

where

$$\sigma_0 = \int_0^{4\mu^2 v^2} \frac{d\sigma_{\chi-N}(q=0)}{d|\vec{q}|^2} = 4G_F^2 \mu^2 C$$

is the cross section at zero-momentum transfer,  $F$  is the form factor ( $F_0 = 1$ ),  $\mu = \frac{m_N m_\chi}{m_N + m_\chi}$  is the reduced mass, and  $C$  is a dimensionless constant including all the particle-physics information and assuming different values as a function of the type of interaction. Saying  $J$  as the total angular momentum of the nucleus and  $\Lambda^2$  as a function of the spin content of neutrons and protons inside the nucleus, in the case of spin-independent coupling we obtain

$$\begin{cases} C_{spin} = \frac{8}{\pi} \Lambda^2 J(J+1) \\ \sigma_{0,spin} = \frac{32}{\pi} G_F^2 \mu^2 \Lambda^2 J(J+1) \end{cases} \quad (2.15)$$

while in the case of spin-independent

$$\begin{cases} C_{scalar} = \frac{1}{\pi G_F^2} [Z f_p + (A - Z) f_n]^2 \\ \sigma_{0,scalar} = \frac{4\mu^2}{\pi} [Z f_p + (A - Z) f_n]^2 \end{cases} \quad (2.16)$$

where  $f_n$  and  $f_p$  are the neutralino couplings to neutrons and protons. Assuming  $f_n \cong f_p$ , a value  $C_{scalar} \propto A^2$  is obtained. In the case of independent

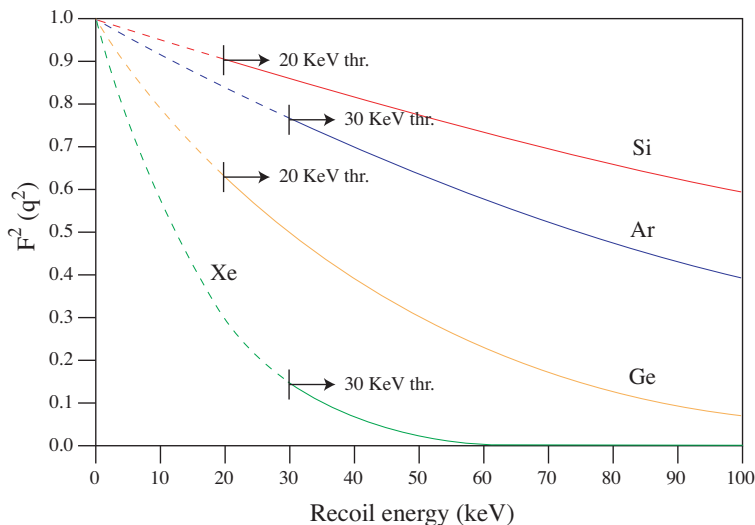


Figure 2.2: Spin independent nuclear form factors for the common typical target used in the direct search experiments. It is clear the decreasing of the factor with the increasing of the atomic number [Si(A=28),Ar(A=40),Ge(A=73) and Xe(A=131)]

coupling, only the unpaired nucleon will contribute significantly to the interaction as the spins of the  $A$  nucleons in a nucleus are systematically anti-aligned. In the second case, all nucleon contributions add coherently: the total amplitude scales as  $A$  and the total scattering probability as  $A^2$ . Direct searches can profit of this scaling using targets with a large  $A$ , due to the fact that in any model including at least a spin-independent component for the interaction, this term dominates the cross-section due to the factor  $A^2$ . We can now summarize the description of the recoil differential energy spectrum in a single equation:

$$\frac{dR}{dE_R} = R_0 S(E_R) F^2(E_R) I \quad (2.17)$$

where  $S(E_R)$  is the behavior of the expected recoil spectrum, accounting the correction due to detector energy resolution and its moving in the galactic frame,  $R_0$  is the total recoil rate for unit of mass (supposing a motionless detector),  $F^2(E_R)$  is the nuclear form factor previously introduced and  $I$  is a function needed to take into account the type of interaction (spin independent or spin dependent). According to the previous corrections, the rate of interaction on a target of atomic mass  $A$  is

$$R(E_1, E_2) = \int_{E_1}^{E_2} c_1 \frac{R_0}{E_0 r} e^{\frac{-c_2 E_R}{E_0 r}} F_A^2(E_R) dE_R \quad (2.18)$$

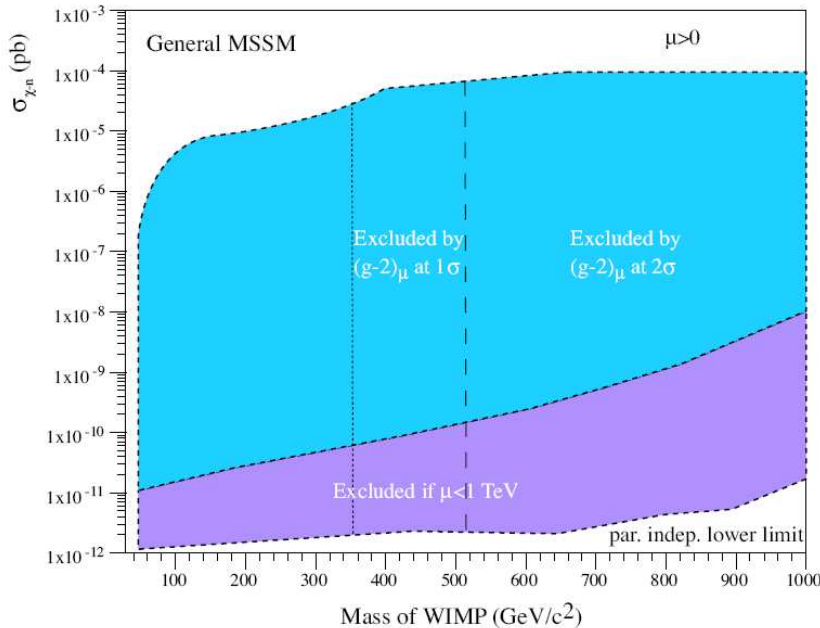


Figure 2.3: Allowed region of  $(m_\chi, \sigma_{\chi-n})$  parameters, obtained considering collider bounds and the requests of a not negligible neutralino cosmological abundance. See text for other possible constrains.

The nuclear form factor is defined as the Fourier transformation of the density distribution of the scattering centre within the nucleus <sup>3</sup>, so that  $F^2(E_R)$  is included in the range  $[0, 1]$  and its value decreases with the increasing of the momentum transfer. Thus at high energy the differential recoils energy spectrum is partially suppressed. Moreover, the decreasing of the factor  $F^2(q)$  is faster as the higher is the value of  $A$ . In this way for high  $A$  nuclei the high energy recoils, those easier to detect, are strongly depleted. This effect reduces the possible enhancement of the cross section with the atomic mass. As stressed before, the recoil energy spectrum gives some fundamental information to constrain two physically important parameters:  $M_\chi$  and  $\sigma_{\chi-N}$ . In order to compare different experiments using typically different targets within this formalism, the WIMP-nucleon cross section is usually used instead of the total cross section WIMP-nucleus. Assuming the same coupling between neutralino and proton and neutron, the cross section

<sup>3</sup>Defining  $g = (qr_N)$ , where  $q$  is the module of the momentum transfer  $r_N$  is the effective nuclear radius, it is possible to write the form factor as

$$F(g) = 3 \frac{j_1(g)}{g} e^{-\frac{(qs)^2}{2}}$$

where  $j_1$  is the spherical Bessel function and  $s$  is a constant  $s = 0.9fm$

neutralino-nucleon is not dependent on the momentum transfer since in our energy range of interest the nucleon can be considered as point-like. Using the spin independent formalism, the cross section in the zero momentum transfer approximation is related to the total cross section  $\sigma_{\chi-n}$  evaluated using  $A=1$  through

$$\sigma_0 = \sigma_{\chi-n} \frac{\mu_N^2}{\mu_n^2} A^2 \quad (2.19)$$

where clearly  $\mu_N(\mu_n)$  is the invariant mass of the WIMP-nucleus (WIMP-nucleon) system. Thus, using the quantity  $\sigma_{\chi-n}$  it is possible to compare different experiments with different targets. Usually the allowed space of parameters  $(M_\chi, \sigma_{\chi-N})$  of the MSSM model is considered using spin-independent interaction. The whole region of parameters is clearly wide due to the poor prediction of the theoretical model. For example, the mass of the neutralino cannot be much greater than  $1TeV/c^2$  and cannot be less than  $50GeV/c^2$ , except in versions of the model that are specially tuned for this purpose. Poor constraints can be obtained considering the results of the direct neutralino's production at colliders, the request of a not negligible cosmological abundance ( $0.1 < \Omega_\chi < h^2$ ). In fig (2.3) the ranges of spin independent neutralino-nucleon cross section and of neutralino mass are reported. Larger limits are provided by the theoretical requests about the Higgs/higgsino mass parameter  $\mu$  ( $0 < \mu < 1TeV$ ). Other constrains can be indirectly obtained measuring rare physical process and estimating the allowed SUSY contributions. This is the case of  $BR(b \rightarrow s\gamma)$  and especially of the anomalous magnetic moment of the muon. Recent results for  $(g-2)$  indicates a deviation from the Standard Model prediction that could be explained in terms of SUSY. The required extra contribution to  $(g-2)$  implies a stringent upper bound  $m_\chi < 350GeV$  ( $1 \sigma$  CL) and  $m_\chi < 512GeV$  ( $2 \sigma$  s) to the mass range, but it does not affect much the allowed ranges of the spin independent scattering cross section. Anyway the value of the anomalous magnetic moment of the muon is still a subject of discussion.

*References:*[1], [23],[24],[27],

## 2.3 LOW BACKGROUND TECHNIQUES

It is clear that extremely low background levels are necessary to explore the range of the MSSM predictions. As comparison a value of 0.1 decays per kgd should be necessary to achieve a  $10^6$  pb sensitivity in the WIMP's direct search, while it is possible to estimate the radioactivity of a human body as  $10^7$  decays per kgd (typically depositing more than 100 keV of energy). The background from natural radioactivity has two sources: external and internal radioactivity. First of all, to reduce the background due to external sources, the detector must be located in a deep-underground site, in order to reduce the cosmic muon flux to factor  $10^{-5}$  to  $10^{-7}$  of the flux at ground

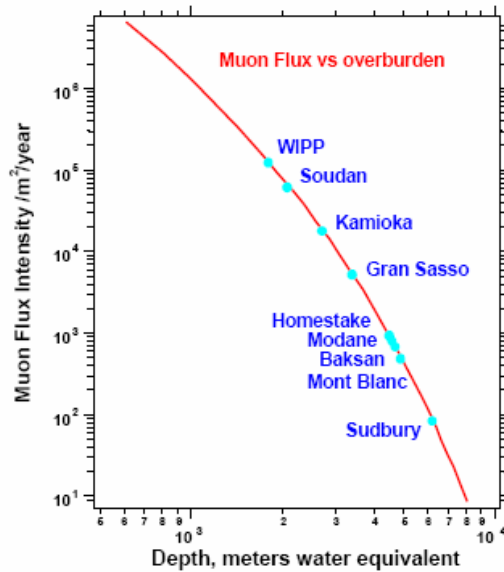


Figure 2.4: Muon flux in number of muons ( $m^{-2}y$ ) in different underground laboratories

level. Moreover, thick depth of absorbing material are generally used to shield the detector from external sources of radioactivity: a high- $Z$  material (for example lead) is very useful to stop MeV-energy  $\gamma$ -rays, while a few mm of low- $Z$  shield could be enough to stop low energy  $\gamma$ -rays,  $\beta$  and  $\alpha$  radiations. It must be stressed that, due the request of a low background, the design and the thickness of the shield must be exactly calibrated to reduce the external background to a suitable level. For example, beyond a thickness of 20-25 cm of lead, the shield could become itself a source for the internal radioactivity. Principally for what concern a WIMP's direct search, the main source of background could be produced by neutrons (environmental or from material contaminations), as they can produce nuclear recoils similar to those produced in WIMP collisions. Thus, fast neutron shields, made of material with a high density of hydrogen, such as polyethylene or water, are typically used as moderators. On the other side, it is a must the use of high radio-pure material inside the detector. Moreover, if the detector size is appreciably larger than the mean free path of high-energy photons or neutrons in the active material, the background interactions produced by the contamination of the surrounding materials will occur mostly at the sensible volume borders (other interactions produced by low-energy photons, beta and alpha rays have a really short typical mean free path ( $< mm$ )). Generally it would be useful to add an active background rejection technique to the passive shielding, in order to discard those event clearly not produced

by WIMP interactions. A possible rejection method could be based on the identification of multiple interactions. While the mean free path of a high energy  $\gamma$ -ray or a neutron in matter is of the order of the cm, the mean free path of a WIMP in matter is of the order of a light-year, due to the extremely low cross section of WIMP interaction. Thus the probability of two consecutive interactions in a single detector (or two adjacent detectors) is completely negligible. In this way, it is possible to reject those events that have more than one interaction in the detector defining a minimal time window between two following events or packing the sensible volume within a veto active volume. Furthermore an efficient identification method of the events (generally based on the different event's signature in the detector) is necessary in order to achieve a good rejection against energy deposits due to non-WIMP interactions. This background can be discarded using an event-by-event analysis, based on a direct identification of each single event, or using a statistical rejection, where a fraction of the total event sample could be identified as coming from a well-defined type of background. In any case the confidence of the identification method must be evaluated. In the first case the probability of failing (i.e. the identification of a background event as a WIMP event) must be estimated, in the second case the measurement of the WIMP rate is limited by the statistical fluctuation on the data sample. It would be possible to get indication of the existence of WIMPs in many different ways, thus many methods could be used in principle to get evidences of WIMP signatures. In order to obtain a convincing WIMP evidence, an experiment should combine more than one of these signatures. In the following scheme some of them are reported, with the main remarks about their motivations.

**Nuclear recoils direct detection:** This signature is based on the discrimination of nuclear and electron recoils. While most radioactive backgrounds typically interact via the electromagnetic force and produce electron recoils, WIMPs can only produce nuclear recoils. The discrimination is generally based on the fact that the former have a larger energy loss per unit length ( $dE/dx$ ) and a smaller recoil range. This also leads to the previously discussed quenching effects, as well as difference in scintillation time of the sensible material of the detector.

**Shape of the recoil energy spectrum:** The observed  $E_{recoil}$  spectrum can be compared with the expectation spectrum (that can be calculated as function of the WIMP's mass). In principle, the knowledge of the background spectrum could be used to apply a background subtraction, to make the observed energy spectrum consistent with the expectation. Anyway, this method is not so useful due to the few number of expected events and to the exponential shape typical of many background sources. The theoretical predictions are commonly used to define the optimal  $E_{recoil}$  search range.

**Coherence:** the observed interaction rate in a detector must be influenced by the scattering cross-section that should be proportional to  $\mu^2 A^2$ , for spin-

independent interactions, while the scattering cross-section of fast neutrons is approximately equal to the geometrical cross section of the target nucleus (corresponds to a  $A^{2/3}$  dependence).

**Time modulation in energy and direction spectra:** As discussed before, the composition of the earth and sun's velocity respect to the galaxy during the year makes a modulation in the WIMP's flux and their average kinetic energy. This modulation may be used as WIMP signature, although its magnitude is strictly depending on the halo model and this effect would require large sample of data. Moreover, the apparent direction of the WIMPs flux should be also correlated to the motion of the earth in the galaxy and to its the rotational motion during the day. Thus the annual modulation and a diurnal modulation in the direction of the WIMPs flux could be evidenced in addition to the energy spectra. However, due to short range of the nuclear recoils ( up to  $\sim 20nm$  in a solid and  $\sim 30\mu m$  in gas for a 20 keV recoil), most of the experiments are not sensitive to the recoil direction and cannot estimate the angle  $\theta_R$ .

As stressed before, the differential event rate is conventionally expressed as  $dru$  ( $events \cdot keV^{-1} \cdot kg^{-1} \cdot day^{-1}$ ). The total rate  $R_0$  integrated over the energy is so expressed as  $events \cdot kg^{-1} \cdot day^{-1}$  or "total rate unit" ( $tru$ ). In some experiments it is necessary to utilize the partial integral of the differential spectrum between two different values of  $E_R$ . In this case the denomination "integrated rate unit" ( $iru$ ) is commonly used.

*References::* [1],[27],[28],[30],[25]

## 2.4 REVIEW OF PRESENT EXPERIMENTS

The requirement of low threshold, reasonably high target mass and ultra-low background for WIMP direct detection experiments seem to constrain the detector technology. Nevertheless, today there are many different experiments searching WIMPs, based on a large variety of technology; several others with increasing mass have been proposed. However it can be now stressed that the counting time is strictly related to the detector mass in order to provide enough statistic for the detection of such rare events (the product of the mass and the counting time ( $M \times T$ ) defined as total exposure is typically used as indicative parameter). It is possible to classify direct WIMPs search experiments into two different categories. The first one historically developed had as aim the realization of a detector with a mass as large as possible, reducing passively the background shielding the detector active region. The ambition is to get a WIMP signal above background after long exposures. However, the sensitivity of this method only increases with  $(M \times T)^{1/2}$  due to the statistical nature of the discrimination. A more recent category of direct search experiments focuses mainly on the event-by event discrimination of signal against background, in order to

discriminate nuclear-recoils over the radioactive electromagnetic background giving mainly electron-recoils. Compared to the first category the sensitivity is enhanced in direct proportion to the exposure, obtaining in this way the best WIMP sensitivities. The discrimination technique is based on different responses of the detectors to different interacting particle of the same energy. For example such discrimination could be associated to the fact that electron recoils have an energy loss per unit length ( $dE/dx$ ) different from that related to nuclear recoil: thus the response to the ionization signal detection would be different for different particles at the same energy. Generally it is possible to get an efficient discrimination of the nuclear recoil signal against the electron recoil if the ratio recoil signal over  $\gamma$  signal ( $rc/\gamma$ ), typically used as discriminating parameter, is quite different from the unity in a wide range of energy. Since the detectors are usually calibrated using  $\gamma$ -sources (i.e. the energy scale is given in as keV e.e. (electron equivalent), a good understanding of the ratio ( $rc/\gamma$ ) is also necessary to set the right energy nuclear scale. From the point of view of detection techniques for nuclear recoil energy, it is possible to distinguish three different techniques based on ionization, scintillation and phonon detection. The ionization signal can be produced inside a detector sensible volume by the free electron-ion couples (liquid or gaseous target) or alternatively by electron-hole pairs (crystals), collected using a drift field and detected by charge sensitive devices. Another detection principle is based on the collection of the light produced during the de-excitation of the atoms of a scintillation target like NaI(Tl) [ $rc/\gamma \cong 0.3$  (Na) - ( $rc/\gamma \cong 0.09(I)$ ] or Xe ( $rc/\gamma \cong 0.2$ ). The last typically used detection principle is based on the collection of the phonons produced in cryogenic detectors (cooled at temperature of few  $mK$ ). This technique can provide the lowest energy threshold in nuclear recoil detection (down to few  $mk$ ), due to possibility of detection of a really tiny energy deposition. However, this kind of detection provide a ratio  $rc/\gamma \cong 1$ , not providing in this way an intrinsic discrimination method for background rejection. At present, the most interesting direct searches have reached sensitivities close to  $10^6 pb$ . This allow to explore the domain of optimistic Supersymmetric models, but more orders of magnitude are necessary in order to cover most of the SUSY predictions. Anyway some experiments aim to improve this result during the next years.

### CDMS-EDELWEISS

To detect WIMPs interactions, CDMS uses ZIP (Z-dependent Ionization Phonon) detector technology, consisting in disc-shaped germanium (250 g) or silicon (100 g) crystals as absorber. The technique allows the simultaneous detection of ionization and phonons signals. One face of the disc is covered by a thin layer of aluminium and 1024 tungsten transition-edge sensors (TES) which are evenly distributed over the surface. The  $Al$  layer

provides the phonon-phonon coupling between the two materials, so that the a-thermal phonons can pass the interface realising their energy into the Al by breaking Cooper pairs. These pairs are tunnelled into and the TES's at the superconducting transition temperature, and thus a small variation in the TES temperature will cause a significant change in the TES resistance ( $\sim 10m\Omega$ ), which is then read out. The other face of the detector, covered by Al, allows the collection of the charges using an electric field. The double detection technique provides both high sensibility and an efficient discrimination method. While the phonon signals in Ge and Si detectors give a low detection threshold ( $\sim 10keV$ ), they are characterized by  $rc/\gamma \sim 1$ . The correspondent ionization signal provides the possibility of a discrimination of the  $\gamma$  and  $\beta$  background. Recently, CDMS published the analysis of its first Ge WIMP-search data taken at Soudan during the period October 2003 - January 2004. This analysis revealed no nuclear-recoil events in 52.6 kg-d raw exposure in the Ge detectors. The data was used to set an upper limit on the WIMP-nucleon cross-section of  $4 \times 10^{-43}cm^2$  at the 90% C.L. at a WIMP mass of  $60GeV/c^2$  for coherent scalar interactions and a standard WIMP halo. The Edelweiss experiment is located at Modane Underground Laboratory in France. The detector is surrounded by passive shielding made of paraffin (30 cm), lead (15 cm), and copper (10 cm) and it uses the same principle as CDMS for WIMP detection: Ionization-heat discrimination. Unlike CDMS's athermal phonon sensors, the tiny rise in temperature, due to a particle event, is measured by an NTD (Neutron Transmutation Doped) heat sensor glued onto one of the charge-collection electrodes. Three events compatible with nuclear-recoils have been observed. However, the recoil energy of one of the events is incompatible with a WIMP mass  $< 1TeV/c^2$ . The other two events have been used to set the upper limit for WIMP-nucleon spin-independent interaction shown in Fig 2.5. The experiment is currently background-limited due to the lack of an active surface-event rejection, making the distinction between nuclear-recoils and near-surface background events very difficult. Edelweiss I experiment has now been stopped to allow the installation of the second-stage Edelweiss II, using 320 g Ge detectors equipped with NTD heat sensors and seven 400 g Ge detectors with NbSi thin film (sensitive to athermal phonons). With an improved polyethylene and lead shielding and an outer muon veto, the expected sensitivity for  $\sigma_{\chi-n}$  is about  $10^{-44}cm^2$ .

## CRESST

The CRESST I detector is a cryogenic bolometer using sapphire crystals as absorber at a temperature of  $15mK$ . This technique provides a really low threshold on nuclear recoils ( $\sim 500eV$ ), and it is sensitive to low WIMP's mass ( $m_\chi < 20GeV/c^2$ ). Nevertheless, the reduced target mass (262 g) provides a low experimental sensitivity. An upgrade of the experiment has

been developed using a technique based on the simultaneous detection of scintillation light and phonons produced by a scintillating absorber crystals in cryogenic calorimeters. This technique can give background suppression similar to that provided by the simultaneous measurement of ionization and light. It is known that a large variety of scintillating crystals ( $CaWO_4$ ,  $BaF$ ,  $PbWO_4$ , etc.) can be used in this manner. This method has been developed by the CRESST collaboration for the CRESST II experiment using prototype detector with 300g of  $CaWO_4$  as sensible volume. The main advantage over the Ge-based detectors is to avoid any possible surface-event problem caused by the contamination in the electrodes material. However, the technique also has some difficulties. First, rather than using PMTs to observe the scintillation signal (to avoid a possible radioactive background), the current approach is to use a second, phonon-mediated detector adjacent to the primary detector. The light collection is relatively poor, resulting in an energy threshold of 15-20 keV. Second, there are three nuclei in the crystal, all of which could potentially interact with the WIMPs. Moreover, the existence of three different nuclei in the target requires a careful study of the scintillation-yield and makes the event interpretation difficult. The goal of CRESST II is to build a 10 kg detector consisting of  $33 \times 300g$  crystals to reach a sensitivity for  $\sigma_{\chi-n}$  of the order of  $10^{-44} cm^2$ .

## DAMA

Although it can be considered a detector based on an old technology (without any pulse shape discrimination), the DAMA experiment is presented at the end of this section due to the fact that it is the only experiment that has detected an evidence of WIMPs. The DAMA project was begun in 1990 by an Italian group at Gran Sasso underground laboratory. The detector is based on nine 9.7 kg highly radiopure NaI(Tl) scintillators shielded from radioactive background, in order to detect the scintillation photons produced by nuclear-recoil events. The threshold provided is at 2 keV. The DAMA experiment can be considered to belong to the first category of dark matter experiments, which require a large detector exposure (107,731 kg-day over 7 years of operation). The Dama group also showed a slight difference between the pulse shapes produced by nuclear and electron recoil events. Though the latter factor could help to statistically discriminate WIMPs against radioactive background, it has been ignored in the DAMA data analysis due to low efficiency. In 2000, using a five-year exposure, the DAMA collaboration claimed to observe a  $6.3\sigma$  C.L annual modulation in WIMP-proton elastic scattering. Recently, DAMA confirmed the observation by adding the results from two more annual cycles. The DAMA evidence for the annual modulation is clear but only in the lowest energy bins (2-6 keV corresponding to a nuclear recoil energy of 22-66 keV for interaction on I nuclei) where the understanding of the efficiencies is particularly important. It must be

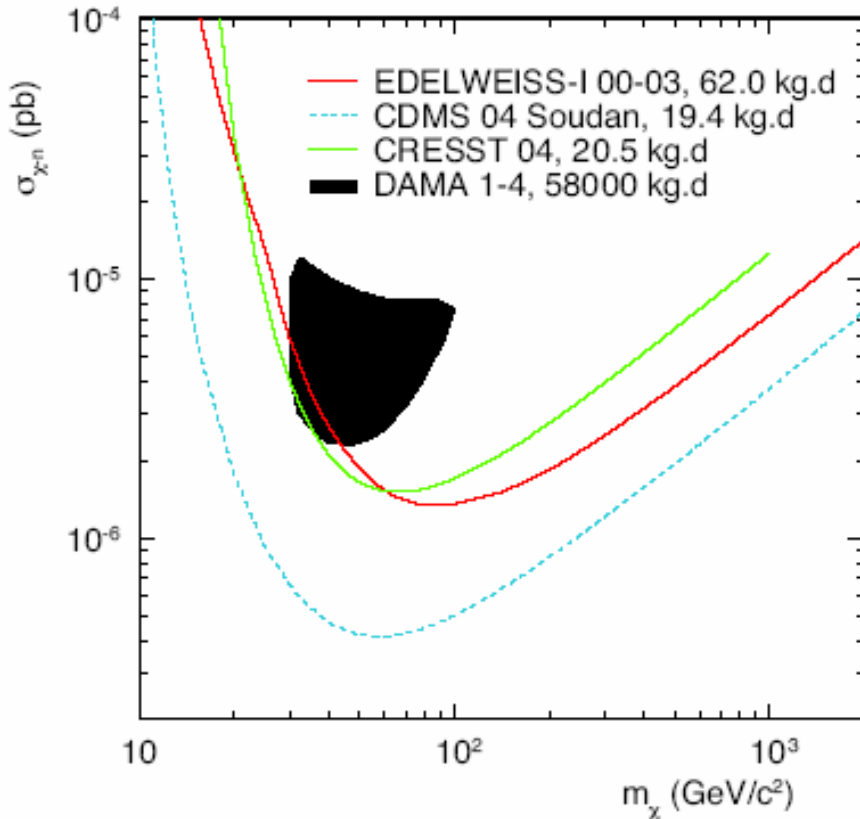


Figure 2.5: Recent experimental results: the closed contour shows the apparent signal region from the DAMA annual modulation while the open curves delimit the exclusion plot at 90% confidence limit for spin independent interaction obtained by CDMS, EDELWEISS, CREEST II.

stressed that the origin of this effect and its interpretation are widely disputed, although many studies have been performed by the collaboration regarding various possible systematic effects. Meanwhile the DAMA collaboration has upgraded the detector, reaching a sensible mass of 250 kg of NaI(Tl). Thus this new experiment called LIBRA is in measurement from March 2003 searching a confirm of the annual modulation previously shown. Such effect should be compatible with the seasonal modulation rate which could be generated by a WIMP with  $M_\chi = (58_{-8}^{+10})\text{GeV}/c^2$  and of scalar cross-section on protons of  $\sigma_{\chi-n} = (7.2_{-0.9}^{+0.4} \times 10^{-6})\text{pb}$  which could represent the most optimistic parameters allowed by the SUSY predictions. Assuming the standard spin-independent model describer previously, the Dama evidence region in shown in fig (2.6). During the last years many experiments whose aim was a WIMPs direct search have been upgraded in order

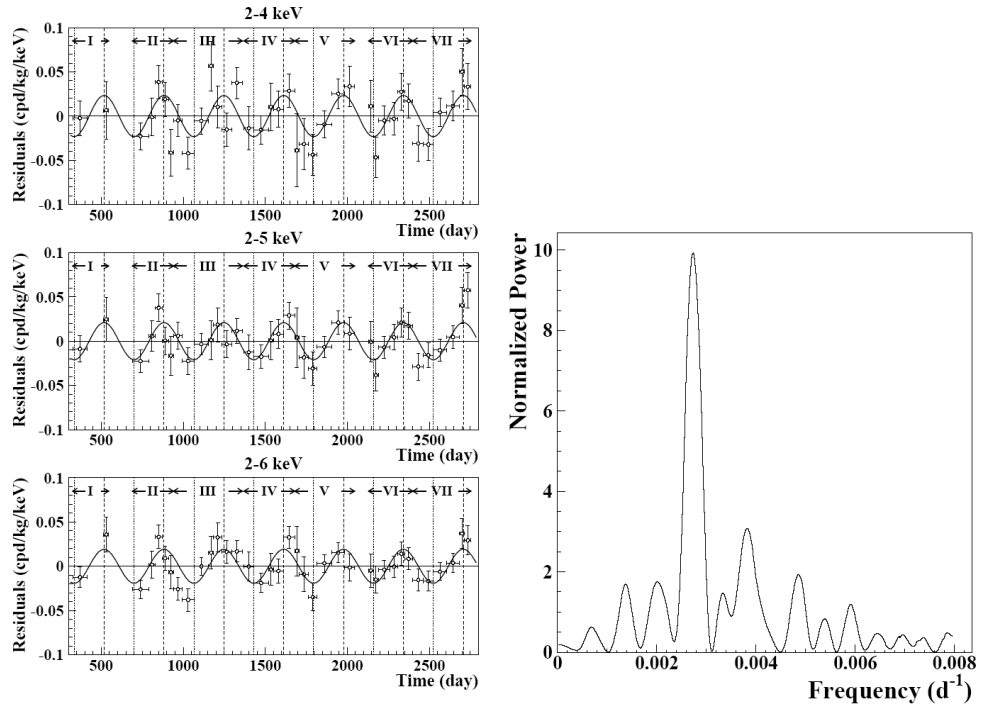


Figure 2.6: Left: The DAMA's annual modulation of the residual rate in three different energy range (2-4),(2,5)and (2,6)keV during 7 years. Right: Power spectrum of the measured modulation in the range (2-6)keV. The principal mode corresponds to 1 year period

to reach a sensibility better than of  $10^{-6}pb$  , without giving any further evidence of WIMPs signal. In fig (2.6) the most recent results of CRESST, EDELWEISS and CDMS have been reported as exclusion plot of the allowed range of parameters. As we can see the DAMA's favourite region should be ruled out by these new results, although the DAMA's evidence, differently from the other experiments, is based on several years of observations. The discussion is still open and more evidence to confirm or to exclude the result is needed.

*References::* [1],[34],[35],[36],[28],[27],[25]

## 2.5 NOBLE LIQUIDS EXPERIMENTS

Noble liquid scintillating detectors can provide large volume of highly purified target material. The using of noble liquid such as Argon and Xenon provides the great advantage of the simultaneous scintillation and ioniza-

tion yields due to their low ionization potentials, thus both the signal can be collected. Moreover the development of very efficient purification techniques developed for noble gases can provide targets with a low level of radioactive isotopes and other contaminations so that the targets would be virtually background free. The use of noble liquids has been demonstrated to provide an efficient event by event identification of nuclear and electron recoils, based on different scintillating time constants or different amounts in the ionization and scintillation yields. The **ZEPLIN** collaboration (Boulby mine, UK) uses liquid Xenon as a scintillating material. The target consists of a 5 kg cell of purified liquid Xenon surrounded by a 1-ton Compton veto, while 3 PMTs are used in order to detect the scintillation light. The acquired light signals show different time constants for nuclear and electron recoil events, and both rise-times are also functions of the deposited energy. Today some experiments using a double phase detector (liquid+gas) have been proposed. According to this technology the ionization charge produced in the liquid phase is extracted into the gaseous phase (using a strong electric field), where a secondary proportional luminescence is produced and detected. The simultaneous detection of both ionization and scintillation can provide an additional method for the recoil discrimination. One of the experiments based on this technology is the **XENON** project, a dual phase Xenon experiment using a time projection chamber. In spite of **ZEPLIN** or **XMASS** which only use a liquid phase and can therefore only achieve a limited discrimination between electronic and nuclear recoils, the double detection of ionization and scintillation signals can efficiently improve the nuclear recoil discrimination over the background.

Concluding, it must be stressed the main property of Ar or Xe as a WIMP detector concern their possible future development as large mass detectors, and the unique outstanding possibility of background discrimination. First of all the possibility of considerably long drift (due to the high mean life of the electrons in the noble liquid) allows the creation of large sensible volume (a detector using LAr of many hundreds of tons has been built by the **ICARUS** collaboration). Detectors with target mass up to 1 ton have been proposed during these years by several collaborations. Moreover it has been shown during last years the possibility of such type of detectors to provide a good position resolution in order to reject events due to borders contamination and multiple scattering inside the detector. This characteristic, together the low level of radioactive contaminations of the noble liquids reached using efficient purification devices, gives the chance to reach a low background level and an efficient background rejection. All the mentioned features make the use of nobles liquid very interesting for the Dark Matter search.

*References::* [36],[28],[27]

## 2.6 INDIRECT WIMP SEARCHES

It should be possible to have indirect evidence of on the WIMPs by searching for products of WIMP annihilation in regions that are expected to have relatively large WIMP concentration, such as galactic centers, the centre of the Sun, or the center of the Earth, where the WIMPs are expected to be gravitationally captured. As predicted by SUSY models, this search is based on the assumption that the WIMP is its own antiparticle and that equal numbers of WIMPs and anti-WIMPs are present. Thus a signal of the  $\chi - \bar{\chi}$  annihilation could be found as flux of  $\gamma$ -rays, neutrinos, or antimatter (positrons or anti-protons) coming from an area where a large concentration of WIMPs is expected. Many experiments have been proposed to observe indirect signatures of WIMPs, and this research is quite complementary to direct observation in the laboratory. One of the possible way to observe the WIMP's annihilations is the observation of high energy  $\gamma$ -rays. It is possible to suppose that the production of  $\gamma$ -rays would occur in different ways. Both a continuous and a mono-energetic spectrum are expected. The first one can be produced from the hadronization and decay of  $\pi^0$  produced in the cascading of the annihilation products, while a direct production of  $\gamma$  such as

$$\begin{aligned}\chi\chi &\rightarrow \gamma\gamma \\ \chi\chi &\rightarrow \gamma Z\end{aligned}$$

can produce mono-energetic  $\gamma$ -rays of energy  $M_\chi$  and  $M_\chi(1 - M_Z^2/M_\chi^2)$ . Photons of such energy, coming from sites where an high density is expected, would be a clear indication of WIMP annihilation. Anyway the size of this signal depends very strongly on the halo model. The searching of such WIMP's evidence is based on different techniques. Ground-based experiments rely on Atmospheric Cherenkov Telescopes (ACTs), such as CELESTE (France) and STACEE (New Mexico). The main feature of such experiments consist in distinguish (usually at  $> 99\%$  efficiency) between the showers caused by  $\gamma$ -rays and those caused by cosmic rays that is the dominant background. Many of them have a dedicated mirror in order to observe the rays coming from the most promising points (CANGAROO (Australia), VERITAS (Arizona), CAT (France), HESS (Namibia)). The typically sensitivity is of the order of 1 TeV  $\gamma$ -rays, thus such types of experiments have the possibility to investigate a wide range of WIMP mass. Moreover, some satellite-based experiments have completed their research (EGRET, 20 MeV - 30 GeV range) or have been planned to be lunched soon (GLAST, 10 MeV - 100 GeV). Recently VERITAS and CANGAROO have observed an excess in the flux of  $\gamma$ -rays coming from the galactic centre. These observations, however, are not compatible between themselves and can be also explained by astrophysical sources, like a black hole at the galactic centre. In addition to the  $\gamma$ -search just described, neutrinos produced in WIMP-annihilations

inside the Earth and the Sun would be produced. A direct production of neutrinos is expected both directly

$$\chi\chi \rightarrow \nu\bar{\nu}$$

and indirectly

$$\chi\chi \rightarrow f\bar{f}$$

(where the fermion  $f$  can decay and emit a neutrino) . The energy spectrum is thus expected to be continuous and extended up to  $M_\chi$  . Muon neutrinos can be evidenced if they interact with the rock sufficiently close to the Earth's surface, producing an high energy muon (with a direction quite collimated with the original neutrino and with about the same energy). The investigation of the neutrinos produced in the Earth, for example, is focalized on the search of the up going muons with a direction pointing to centre of the Earth. The only possible background could be made by atmospheric neutrinos produced in the cosmic rays interactions with the atmosphere at the opposite side of the Earth. Many experiment, designed mainly to study solar or atmospheric neutrinos (SuperKamiokande, MACRO, AMANDA) or properly proposed (ANTARES, AMANDA II, ICE CUBE), have been used to search the signal of WIMP's annihilation. At the moment, none of the experiments has observed an excess of neutrinos from the Earth or the Sun. *References::* [1],[4][27]

## Chapter 3

# WARP 2.3 liters

### 3.1 INTRODUCTION

As stressed in the previous chapter, the small cross section of WIMP-nucleus scattering requires a large mass detector. Moreover, an efficient background rejection needs an event by event identification, in order to discriminate few nuclear recoils from a large number of interactions induced by electrons.

The liquid Argon technology can provide both these features: it is possible to build large mass detectors at low cost and the energy releasing mechanism in LAr has different aspects that could be influenced by the nature of the impinging particle and by its energy. For example ionizing particles moving in liquid Argon can produce excitons and electron-ion pair along the track, and the measurement of their relative amounts leads to a clear identification for the reacting particle.

In this chapter, the effectiveness of LAr detector for Dark Matter search is shown. After a brief presentation of the light emission mechanism in LAr, a description of the test chamber built by the WARP collaboration is given, with a presentation of the results of the tests in Pavia. The last part of the chapter is devoted to report the preliminary results of the data taking at Gran Sasso laboratory, which shows the effectiveness of the proposed technique.

### 3.2 LIQUID ARGON AS WIMP TARGET

Liquid Argon represents a good sensitive material to detect WIMPs. As shown by the ICARUS collaboration, liquid Argon technology is mature enough and well supported at industrial level to realize large mass detectors with the radio-purity required in rare event search. Moreover, the Argon nuclei have zero nuclear spin, thus avoiding any dependence on the spin-interaction models, and the form factor depression of the largest energy recoils is relatively moderate for Argon (respect to Xe, for example). The

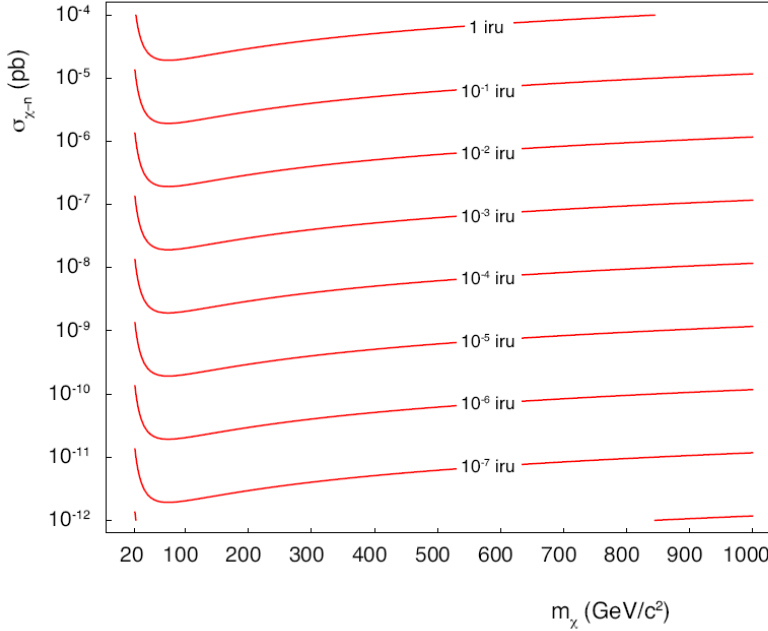


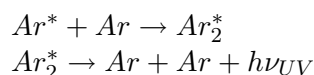
Figure 3.1: Iso-rate curves representing the number of detected events expressed in  $iru(event\ kg^{-1}\ day^{-1})$  for Argon target with detection threshold  $E_R = 30keV$ . The halo parameters ( $\rho_\chi$  and  $v_0$ ) reported in the last chapter and the mean value of the time dependent constant  $c_1$  and  $c_2$  are assumed.

iso-rate curves, representing the number of detectable WIMP-Argon nucleus scattering events expressed in  $iru(event\ kg^{-1}\ day^{-1})$ , are shown in fig. (3.1) as function of the WIMP mass and of the cross section  $\sigma_{\chi-n}$ . The curves represent the solution of the equation (2.18) and have been computed assuming conservative detection limits ( $E_1 = 30keV$  and  $E_2 = 100keV$ ), the galactic halo parameters ( $v_0 = 230km/s$  and  $\rho_\chi = 0.3GeV\ c^{-2}\ cm^{-3}$ ) and the average values for  $c_1$  and  $c_2$ .

It is evident that, in order to explore exhaustively the wide range of the SUSY predictions (fig. 2.3), the detector mass must be very large. For instance, the lower theoretical limit, for the likely assumption for the parameter  $\mu < 1GeV$ , corresponds for Ar to a typical rate of the order  $10^{-6}ev/kg/day$ , namely an event rate of about  $0.1ev/day$  for a sensitive mass of the order of  $100tons$ . Although, WIMPs signatures could be found with much larger event rates, even those very substantial masses are allowed to the LAr technology, giving in principle access to the full range of theoretical predictions.

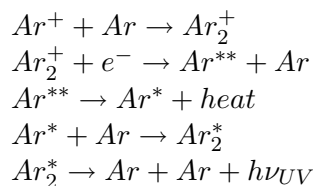
### 3.3 SCINTILLATION LIGHT EMISSIONS IN LAr

The luminescence process in LAr has been studied in details. The passage of ionizing radiation through LAr results in the emission of ultraviolet light without any chemical change. It has been shown that scintillation light has two components, corresponding to two different processes. The *excitation luminescence* is produced by the creation of an excited Argon atom  $Ar^*$ :



The de-excitation of  $Ar^*$  via photon emission is strongly suppressed: in a short time after the formation ( $\approx ps$ ) the exciton  $Ar^*$  captures one of the surrounding  $Ar$  atoms forming an excited molecule  $Ar_2^*$ . The radiative transitions produce the emission of a UV photons peaked 128 nm ( $FWHM \approx 5nm$ ) and  $E \approx 9.7ev$ .<sup>1</sup>

The formation of the free pair ion  $Ar^+$ -electron can produce a photon with exactly the same energy through a different mechanism known as *recombination luminescence* :



The prompt formation of the excited molecule  $Ar_2^+$  avoids the recombination ion-electron, driving to the formation of a exciton  $Ar^*$ . This exciton follows, finally, the same radiative transition of the previous case, so that an  $Ar$  atom and UV photon are finally produced. It is clear that the recombination luminescence is strongly dependent on the presence of an external electric field that can suppress the recombination process. In fig. (3.2) the luminescence light intensity  $L$  and the amount of the collected charge are shown as function of the electric field strength for  $1MeV$  electrons. As we can see, the decrease of light correspond to a the contemporary increase of the free charges collected (the recombination luminescence can be regarded as proportional to the uncollected charge  $Q - Q_0$ , where  $Q_0$  is the produced total charge). It is possible to decouple the two different luminescence components comparing the different results obtained using strong drift field ( $> 10kV/cm$ ) and without drift field. In the first case photons are essentially produced through excitation luminescence, while in the second

---

<sup>1</sup>We assume in this process a radiative de-excitation of the dimer  $Ar_2^*$  to the ground state: due to the large gap between the lowest excitation level and the ground level no decay channel exists except for the above transition. Although this is not clearly confirmed we assume that each excited dimer  $Ar_2^*$  emits one photon.

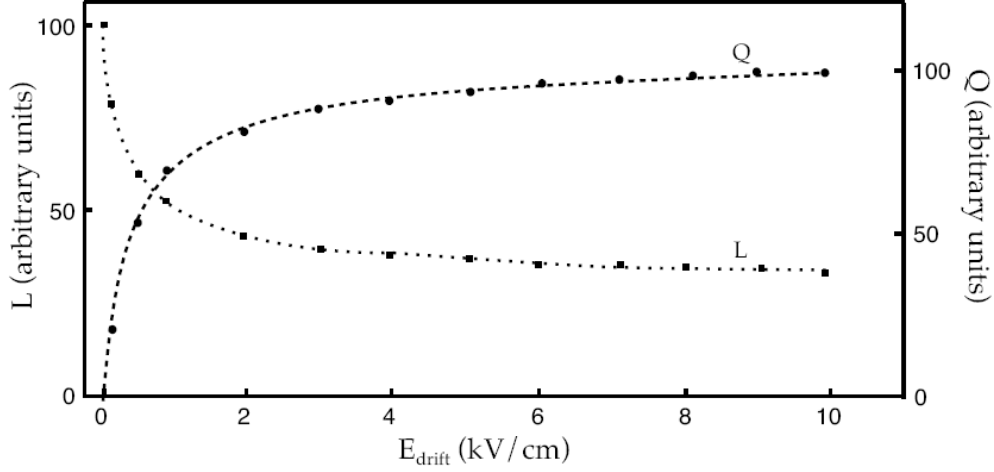


Figure 3.2: Behaviors of the scintillation light intensity and of the collected charge as function of the external electric field (source:  $1MeV$  electrons).

case both the components are present <sup>2</sup>. In fig. (3.3) the time dependence of the luminescence intensity is reported with electric field ( $6kV/cm$ ) and without electric field. The difference curve is also reported to represent the time dependence of the recombination luminescence. As we can see, both contributions are characterized by two components with two different decay constants (about  $6.3ns$  and  $1.5\mu s$ ), that could be due to the transition from the states  $^1\Sigma_u^+$  (singlet) and  $^3\Sigma_u^+$  (triplet) of  $Ar_2^*$  to the fundamental dissociate state.

On the basis of the previous scintillation mechanism, it is possible to estimate the number of photons  $N_{ph}$  produced by a ionizing particle releasing an amount of energy  $E$ :

$$N_{ph} = N_i + N_{ex} = N_i(1 + N_{ex}/N_i) = \frac{E}{W}(1 + N_{ex}/N_i) \quad (3.1)$$

where  $W$  is the energy required for an electron-ion pair production,  $N_{ex}$  and  $N_i$  are the number of excited atoms and ion-electron pairs respectively. Eq. 3.1 shows that  $W' = W(1 + N_{ex}/N_i)$  can be used as parameter to estimate the number of photons emitted by a ionizing particle. For electrons of  $1MeV$  of energy it is possible to assume  $N_{ex}/N_i \approx 0.21$  and using  $W = 23.6eV$ , we obtain a value  $W' = 19.5eV$  and a maximum number of photons emitted of

<sup>2</sup>Observing that at  $10kV/cm$  the 95% of the initial charge is collected is possible to estimate the relative intensity of the two different luminescence components at zero field as  $L_{ex}/L_i(0) \approx 0.43$ .

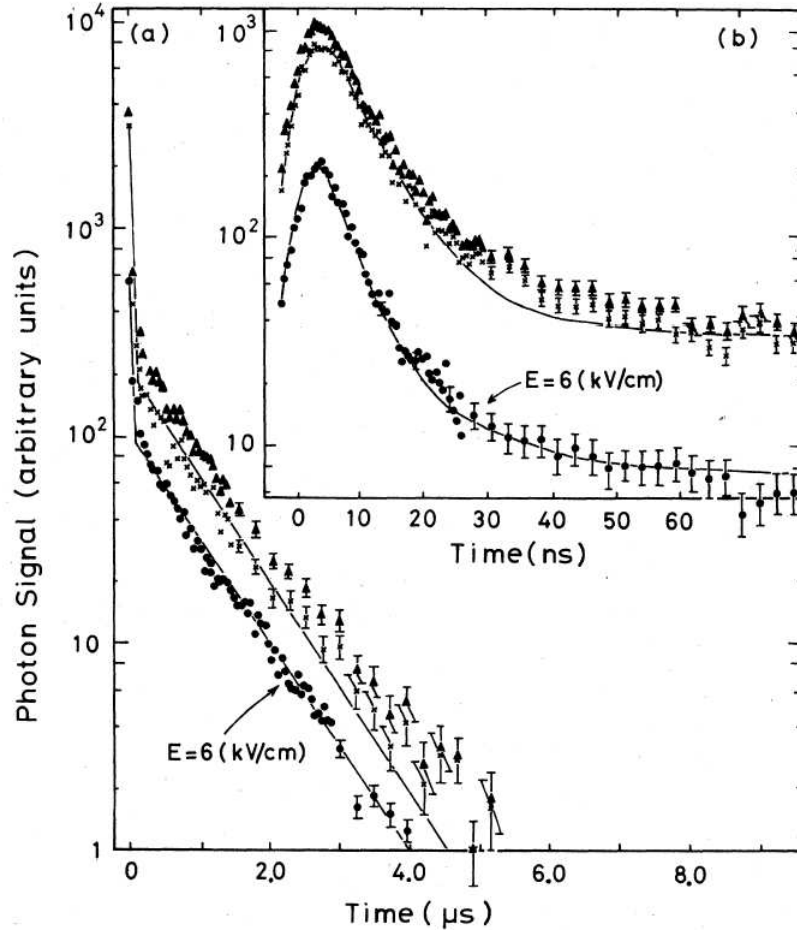


Figure 3.3: Time dependence of the luminescence intensity with (●) and without (▲) an electric field. The plotted data are such that counts for the two curves are equal to the ration  $(L_{ex} + L_r)L^{-1}$ . The difference curve (×) represent the decay curve for the recombination luminescence.

the order of  $5.13 \times 10^4$ . This value is the maximum theoretical scintillation yield  $dL/dE$  (scintillation intensity for unit absorbed energy).

Anyway, the amount of scintillation yield is strongly dependent on the ionizing particle, i.e. on its so-called  $LET$  (linear energy transfer), representing the average energy loss along the particle path (obtained dividing the energy loss and the particle range). Different effects can substantially change the theoretical value of  $W'$ . In fig (3.4) the dependence of  $dL/dE$  on the  $LET$  is shown for several ionizing particles (data obtained at zero electric field). As we can see, only for heavy ions (from  $Ne$  to  $La$ ) it is possible to obtain a scintillation of the order of the maximum theoretical

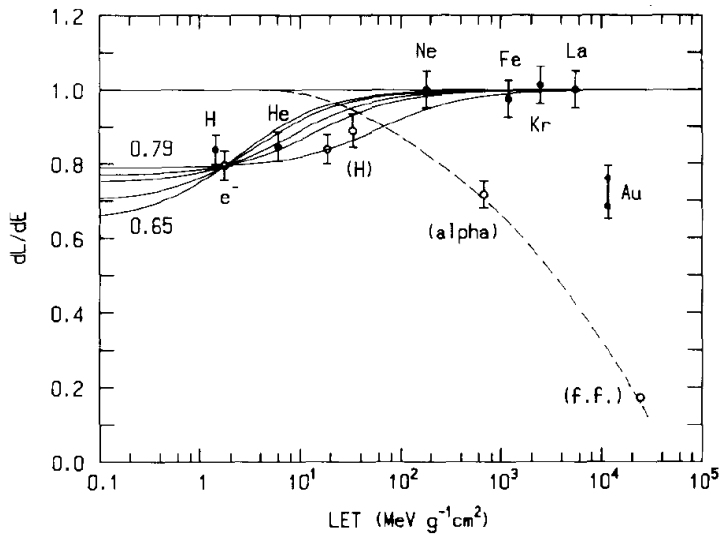


Figure 3.4: LET dependence of the scintillation yields for various ionizing particles. The dashed curve shows the reduction of the scintillation process due to the quenching. Non-relativistic particles are given in the brackets.

value (3.1). The decreasing of the scintillation yield in the low  $LET$  region could be explained assuming that electrons escape from the ionization area in case of relativistic electrons and light ions. Electrons could not recombine for long time ( $\approx few ms^3$ ), producing a decrease in the scintillation yield. It is possible to prove this effect collecting the escaping electrons through a drift field. In fig. (3.5)  $I$  represents the number of the collected electrons on an electrode,  $S$  the number of emitted scintillation photons and  $a$  is a normalization constant. With no drift field the ratio  $aS/(N_{ex} + N_i)$  differs from the unity, while the identity occurs in presence of the drift field. This suggest that the reduction of the scintillation yield is due to the escaping of the electrons and a lower ion-electron recombination. From fig. (3.5) it is clear that in both cases  $\alpha$  particles and fission fragments produce a lower amount of scintillation. This effect could be explained by a *quenching* mechanism that can affect non relativistic particles producing an high ionization density (high  $LET$  particles). The quenching process is not only a function of the energy loss, because relativistic ions like  $Fe$  and  $La$  don't present such effect, but it is function of the structure of the ionization track too. Several models have been proposed to explain the quenching effect and the most accepted is based on a possible interaction between the excitons  $Ar^*$ , allowing an energy fraction to be dissipated through non-radiative channels.

<sup>3</sup>such times are typically longer of than the time window normally used in the experiments.

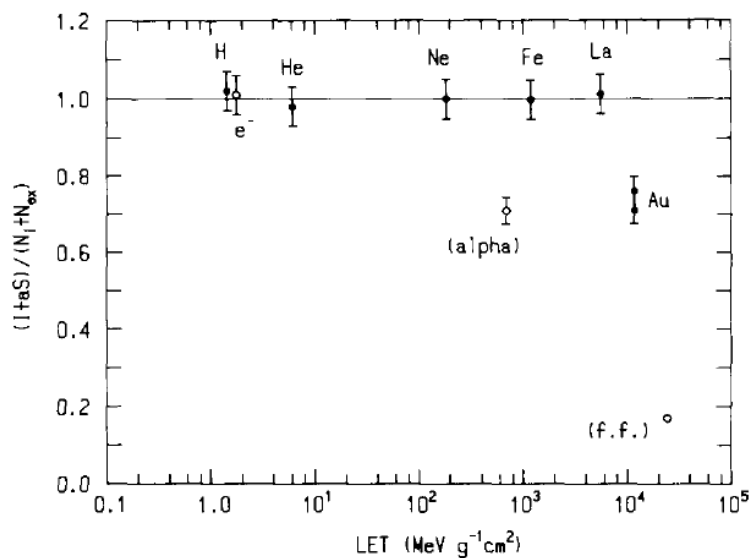


Figure 3.5: LET dependence of the ratio  $I + aS$  to  $N_i + N_{ex}$  for various ionizing particles. Non-relativistic particles are given in the brackets

The quenching rate depends on the excitons density, thus  $\alpha$  particles, although characterized by a LET lower than that of  $La$  ions, present a higher excitons density; this feature leads to a higher quenching effect with respect to relativistic ions. In this way, for  $\alpha$  particles and fission fragments the real energy deposit and the detected one are different, while the identity occurs for the electrons. Measured *quenching factor* of the order of  $f_A \approx 0.3$  tell us that only the 30% of the energy deposited by a slow heavy nucleus can be detected.<sup>4</sup>

As stressed before, the transitions from the first singlet molecular excited state  $^1\Sigma_u^+$  and from the triplet state  $^3\Sigma_u^+$  produce two different scintillation components, characterized by two different decay constants because the transition from  $^1\Sigma_u^+$  to the ground state  $^1\Sigma_g^+$  is favorite by the selection rule respect to the transition form a  $^3\Sigma_u^+$  state. Those time constants are not function of the energy loss density (LET) and they assume similar values for particles of different nature. Anyway, the relative intensity of the two components are strongly *LET*-dependent, so that the singlet component increases with the *LET* growing (fig. (3.6)). The most accepted mechanism that is able to explain this effect is based on a possible interaction between free electron and the singlet state that can produce a singlet to triplet transition, thus producing an enhancement of the number of triplet state and a radiative transition according with the longer decay-constat. The probabil-

<sup>4</sup>Thus an electron of  $30keV$  of energy can produce about the same scintillation signals of a heavy non-relativistic ion of  $100keV$ .

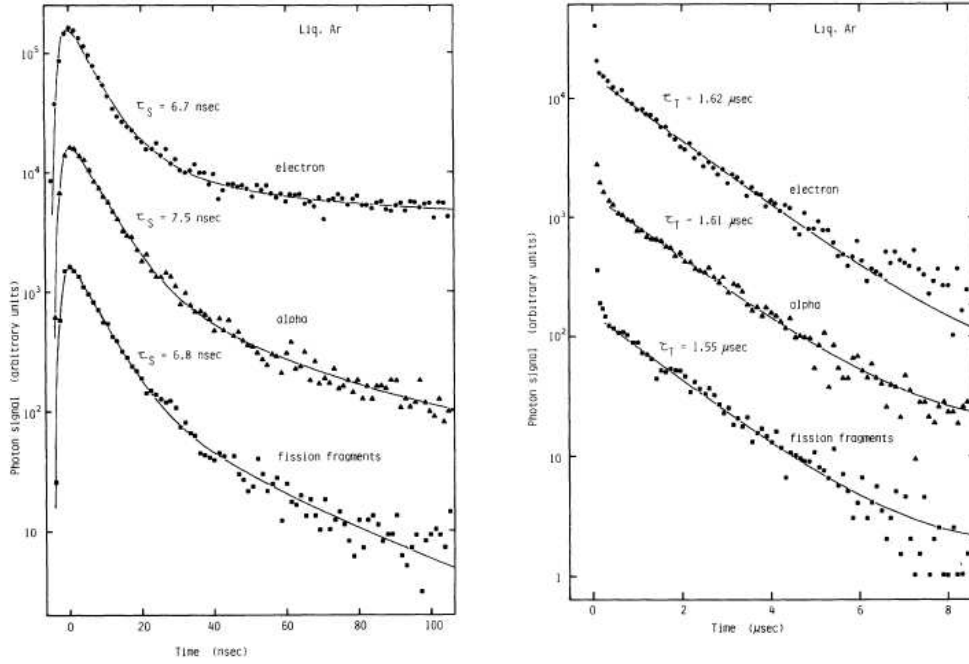


Figure 3.6: Decay curves (at zero field applied) with electrons,  $\alpha$  particles and fission fragments. The fast (left) and the slow (right) components are plotted.

ity of this process is connected to the ionization density. The values of the ratio  $I_s/I_t$  for relativistic electrons,  $\alpha$  particles and fission fragments are

Particle	$I_s/I_t$
Relativistic $e^-$	0.3
$\alpha$	1.3
FF from $^{252}\text{Cf}$	3.0

Concluding, light and charge production mechanism in LAr has several different aspects that are strongly influenced by the nature of the impinging particle and by its energy. Both the energy detected, its partition between ionization and scintillation processes and the time dependence of the scintillation signal can provide interesting features in order to identify the particle using a proper device.

*References*::[37],[38],[41] [42],[40],[39]

### 3.4 PROPOSED TECHNIQUE

As stressed before, electrons and nuclear recoils are characterized by different yields of scintillation photons and free electrons due to different processes

of energy release in  $LAr$ , giving in this way the possibility to determine the nature of the particle reacting in the chamber. Thus the proposed technique is based on the discrimination of the impinging particle through the measuring of the ratio between scintillation light and ionization charge, even if, in case of nuclear recoils, only few hundreds of ionization electrons are produced and only a small fraction (typically of the order of few units) can survive to the recombination process.

The WARP prototype is an Argon double-phase drift chamber, in which a set of photomultipliers allows the collection of scintillation photons produced in both phases. The liquid volume is the sensitive element of the chamber, where the interactions in  $LAr$  produce scintillation photons (at  $128nm$  of wavelength) and ionization electrons. The chamber set-up has been realized suitably to allow the simultaneous measure of both photons and electrons. The main experimental difficulty is the small number of electrons produced in nuclear recoil interactions (at  $1kV/cm$  only few units of free electrons can survive to the strong recombination and can be collected). To detect the ionization signal, electrons are extracted toward the interface liquid-gas using a drift field and then accelerated in a high field region, thus producing a luminescence signal in gas. In this way the scintillation photons produced in the liquid phase (primary scintillation) could be followed by another light signal (secondary scintillation) produced in the gaseous phase, proportional to the initial ionization charge. Both signals are detected by the same photomultipliers, and the delay of the secondary emission respect to the primary emission can be used to estimate the distance of the interaction from the interface.

This technique has been evaluated during preliminary tests at Pavia University. A chamber of  $2.3l$  of the sensitive volume has been realized initially in order to verify the possibility of the simultaneous detection of scintillation photons and ionization electrons produced in the liquid phase, through the detection of the double light signals. During preliminary tests in Pavia, the chamber has been exposed to both  $\gamma$  and neutrons sources, in order to study the responses to different interactions in the sensitive volume (such as electrons recoils induced by Compton scattering and nuclear recoils produced by the elastic scattering of neutrons over nuclei) . Without drift field it has been possible to measure the photon yield (average number of photoelectrons produced per energy unit) for different sources, to get an energy calibration of the chamber, and, using the drift field, the proposed discrimination technique between nuclear recoil and electronic events has been tested.

At the end of the *R&D* period the prototype has been installed in an underground hall of the National Laboratory of Gran Sasso (LNGS) to study its performances in a low background environment.

## 3.5 SETUP OF THE 2.3l TEST CHAMBER

### General set-up in Pavia

The external structure of the chamber consists in a stainless steel vacuum tight cylindrical container (fig 3.7); its geometric dimension are summarized in tab (3.1). To have an uniform drift field inside the tests chamber, the liquid phase is surrounded by stainless steel race tracks and a stainless steel circular cathode is placed on the bottom of the sensitive volume. The top of the drift region is bordered by a set of three grids, 4mm pitched with wires of 150 $\mu$ m of diameter (see fig. 3.8). The first two grids (g1 and g2) enclose the liquid-gas interface and are used to extract the electrons through the interface, while the upper grid g3 is used to produce the field necessary for the proportional scintillation production. The total drift length is 75mm and the total volume is 2.3l. An 8 inch photomultiplier (PMT) Electron Tubes 9537 FLA with a borosilicate glass window is positioned in the gaseous phase at 40mm from the upper grid and it is used for the detection of both primary and secondary scintillation. A reflective and shifting coating covers the internal part of the chamber (drift and gaseous region) thus improving the collection efficiency of photons. In order to get the double phase coexisting in the internal volume of the chamber, the container is placed in an external liquid Argon bath; in this way it has been possible to cool the chamber down to 87.2K (Argon boiling point at 1.02 bar abs) and to get an absolute pressure equal to the external pressure.

One of the main requirements for such type of experiment is to get a good radiochemical purity, in order to reduce the possible background. Moreover, a possible contamination of electro-negative atoms can significantly reduce the small number of ionization charge produced by nuclear recoils. Using the standard purification system developed by the ICARUS collaboration, it has been possible to get a really high level of purification. Ultra-pure commercial Ar with a nominal impurities concentration of 0.1ppm  $O_2$  equiv. has been used, and, in order to maximize the radiochemical purity, it passes further through *Hydrosorb<sub>TM</sub>* and *Oxisorb<sub>TM</sub>* Cartridges before being injected in the drift chamber. A level of 0.1ppb  $O_2$  equiv. has been reached. During the *R&D* period no recirculation system has been implemented because the lifetime degradation has no substantial effect during the run (15  $\div$  20 days of run time after the filling procedure were possible). The right level of the liquid-gas interface (between the first couple of grids in order to extract the drifted electrons) was achieved by measuring the liquid level during the filling procedure with two different kinds of level sensors. The first one uses the change of resistivity of a set of silicon resistors ( $R \cong 1k\Omega$ ) with the temperature, according to the different heat dissipation occurring in the liquid and gas Ar phases. The precision on this measurement is determined by the physical dimension of the resistor itself ( $\cong 1mm$ ). The



Figure 3.7: 3D-view of the test chamber inner volume

Cathode diameter	200mm
Race track inner diameter	200mm
Drift length	75mm
Drift volume	2.3l
Distance g1-g2	10mm
Distance g2-g3	7.5mm
Distance g3-PMT	40mm
Container diameter	250mm
Container height	600mm

Table 3.1:  $\gamma$  Geometric dimension of some components of the test chamber.

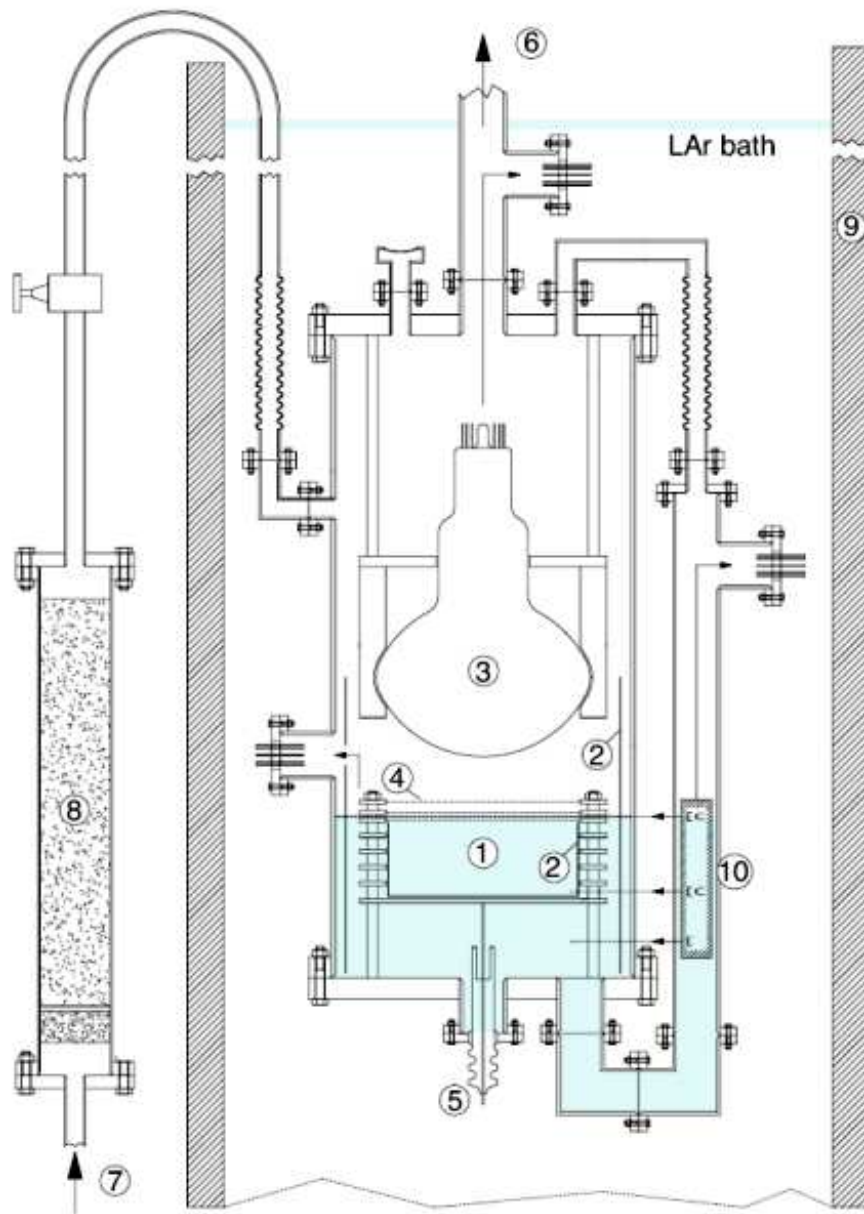


Figure 3.8: Representation of the experimental set-up: (1) drift volume, (2) reflective layer, (3) PMT, (4) grids, (5) HV supply feed-through, (6) line to the vacuum pump and pressure sensors, (7) LAr line injection, (8) Hydrosorb/Oxysorb filter, (9) External dewar, (10) level meters. The liquid Argon external bath is also sketched.

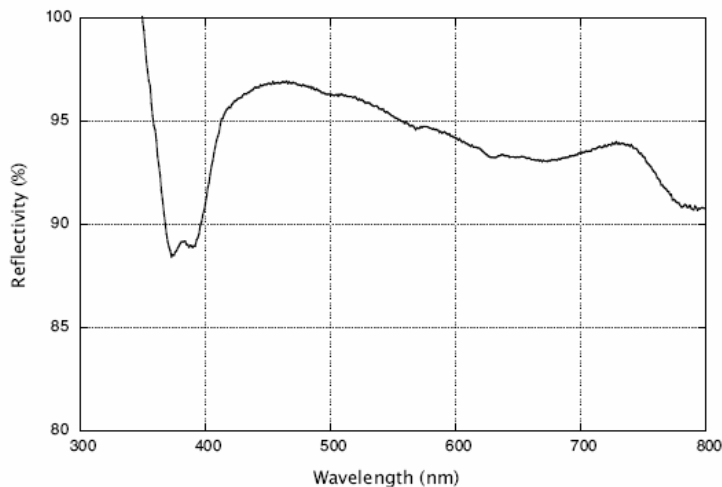


Figure 3.9: Measured reflectivity for the VM2000+ TPB system as function of the impinging light wavelength.

second level meter is made by a metal nail facing a conductor plate  $0.5\text{mm}$  distant: due to the different dielectric rigidity of liquid and gas Argon, it is possible to generate a discharge in the gas phase but not in liquid phase. In this way it is possible to obtain a level meter with a precision of about  $0.5\text{mm}$ . An interaction in the sensitive volume of LAr leads to the emission of prompt primary UV photons (with two decay constants of  $\tau_s \cong 6\text{ns}$  and  $\tau_l \cong 1.5\mu\text{s}$ ), and free electrons escaping from the recombination process. With an appropriate field configuration those electrons, after a drift along a vertical axis, could be extracted from the liquid phase and then accelerated in the gaseous phase, producing secondary proportional light pulses (assuming different values according to the type of ionization event). The role of the multiplication field has been investigated. In fig (3.10) the multiplication factor is shown for different values of the multiplication field, obtained for a fixed extraction field.

A detailed study of the electric field in the WARP 2.3l prototype has been performed using two programmes. The first one is Maxwell 2D-3D, a commercial three-dimensional package (commercially available by Ansoft) that has been used as field simulator software, the second one is Garfield version 8 (available at CERN) to simulate the electrons propagation in order to evaluate the grids transparency, defined as the fraction of the numbers of electrons starting from the liquid that reaches the last grid. The full setup has been implemented with the geometrical details and the materials properties. In fig (3.11) the layout of the complete WARP 2.3 liter prototype is shown as implemented in Maxwell3D. The value of the potential inside

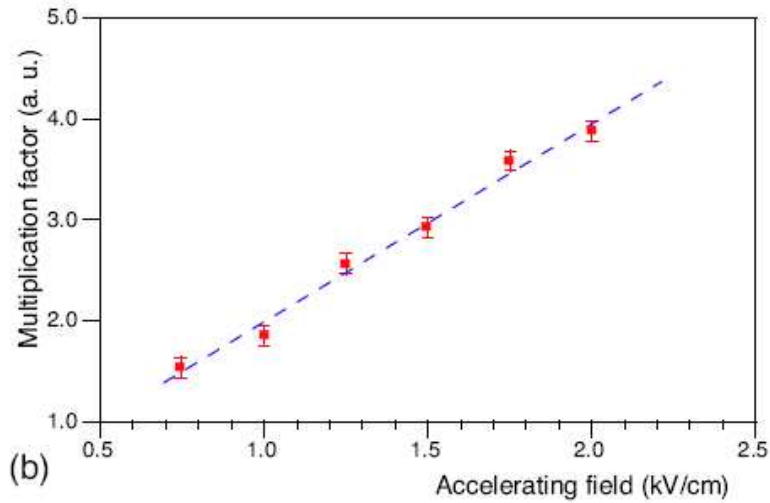


Figure 3.10: Multiplication factor as function of the field between the grids g2 and g3.

the chamber calculated using Maxwell package has been given as input to Garfield in order to calculate the electron drift lines. Different configurations of the grids and different voltages have been investigated. According to the field configuration, a maximum collection efficiency on the last grid of 97% about has been obtained. In fig. (3.11) the electron drift lines, as calculated by Garfield, are shown, according to a new grids setup using a distance of 2cm between g2 and g3, in order to use higher multiplication fields in gas and to reduce discharge problems. Moreover a fourth grid has been added to collect the electrons after the proportional electroluminescence process.

### Light detection

The scintillation UV light produced in the chamber is detected by a set of photomultipliers. It is well known that the UV photons at 128nm produced during the scintillation process in Argon could be absorbed by the glass or quartz windows used by EMI PMTs, causing a reduced transmittance. Only  $MgF_2$  windows could present a transmittance value sensitively different from zero at those wavelengths, but it has been chosen not to use such material due to its high cost and its fragility at low temperature. In order to have a high detection efficiency, the inner surfaces of the chamber have been covered by a wavelength shifter, to obtain the shifting of the 128nm light into a wavelength region for which PMT transmittance is high. The solution consists in the use of Tetraphenylbutadiene (TPB) coated on the

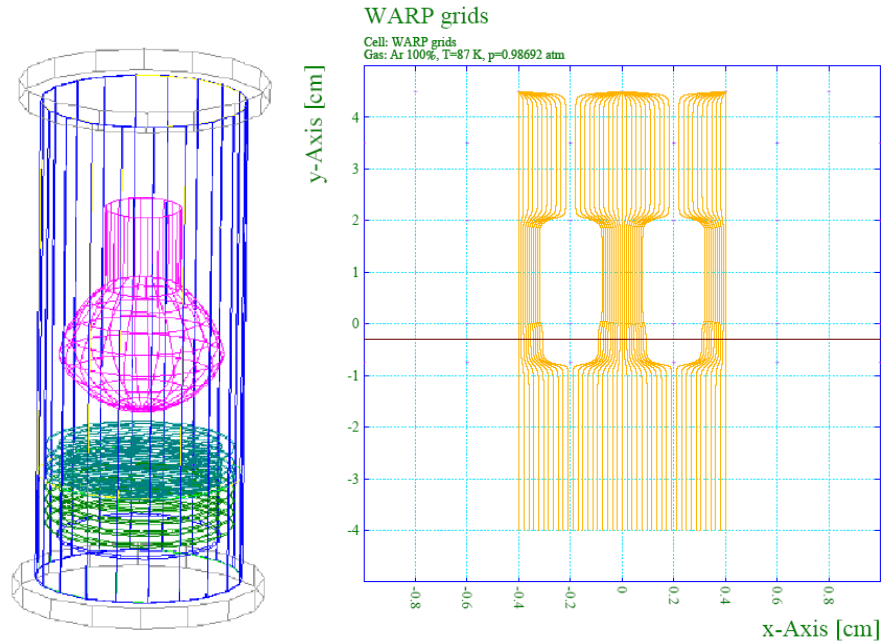


Figure 3.11: Left: layout of the complete WARP 2.3 liter prototype as implemented in Maxwell3D. Right: electron drift line as calculated by Garfield. The liquid-gas interface is indicated by the purple line; the second grid is placed at  $y=0$ .

reflective layer and on the window of the PMTs (about 85% of the inner volume total surface). This material can absorb the pure LAr  $128nm$  light and re-emits it with a broad peak centered around  $438nm$  (visible range). At this wavelength there is an efficient shifting: a rough estimation, assuming an isotropic light re-emission by the TPB, leads to the an average correspondence of one  $\gamma$  (vis.) each one  $\gamma$  ( $128nm$ ). At visible wavelengths it is possible to use reflecting layers, obtaining in such way an increase of the detection efficiency; thus the layer of TPB has been deposited on all the inner surfaces of the chamber using an airbrush by evaporation under vacuum conditions, obtaining a thickness of  $200\mu gcm^{-2}$ . A reflective layer constituted by VM2000<sub>TM</sub> plastic mirror (specular reflectivity 99%, dielectric in order to avoid electric field modifications) glued on Mylar<sub>TM</sub> substratum has been used. In this way an UV scintillation photon is shifted when it touches the PMT window or the diffusive layer, producing the emission of a visible photon reflected by the VM2000 + TPB system, until it is absorbed or detected by the PMTs. The measured diffusive layer reflectivity, in the visible range, is about 95%. The experimental results are shown in Fig.3.9. As stressed before, scintillation signals produced in both phases have to be

detected. A photomultiplier, facing the multiplication region, detects both direct and reflected light (by the diffusive layer surrounding the sensitive volume) produced as primary and secondary scintillation. An 8 inch photomultiplier (PMT) Electron Tubes 9537 FLA with a borosilicate glass window positioned in the gaseous phase has been used. Details about the Electron Tubes photomultipliers are reported in chapter 5. The contemporary detection of primary and secondary scintillation provides interesting features, allowing the investigation of some characteristic of the interaction events. The separation in time between primary signal and secondary scintillation is proportional to the time required to the electrons to drift from the interaction point to the surface. Thus such measurement allows the localization along the drift direction of the event. Moreover, the amount of the scintillation emissions are strictly dependent on the the kind of event (beyond to the field magnitudes). For example, for muons crossing the sensitive volume, the primary light is followed by a long train of secondary photons that lasts for the total drift time. The ratio between the number of photon emitted during both secondary and primary scintillation processes  $N_2/N_1$  can be used to determine the type of reacting particle. Different amounts of excitation and ionization produced by different particles generate a diverse numbers  $N_1$  and  $N_2$  of photons, allowing, in this way, the identification of the particle. According to the discrimination of the particle, the absolute number of primary electrons can be used to measure the energy of the particle reacting in the chamber.

### 3.6 DATA ACQUISITION

To acquire the signals of the primary scintillation, the charge coming from the output of the PMTs is integrated and converted to a voltage signal using a inverting preamplifier Canberra mod. 2005. The preamplifier has two different conversion values ( $4.5mV/pC$  or  $22.7mV/pC$ ) with a rise time of about  $15ns$  and a fall time of about  $50\mu s$ . The integrated signal coming from the preamplifier is shown in fig 3.12. As we can see, two peaks corresponding to primary and secondary scintillation are clearly visible. The voltage output is proportional, for fast signals, to the number of photoelectrons. To get a secondary signal proportional to the input charge, the amplitude of the second peak must be subtracted by the contribution of the first peak and corrected for lifetime degradation depending on the position along the vertical axis. We can define  $S_1$  and  $S_2$  the amplitude of the primary signal and the corrected secondary signal. The output of the Canberra preamplifier is sent to an ORTEC 570 amplifier. The signal is shaped at  $6\mu s$  sufficiently to contain all the primary photons (primary light has a slow component with a decay constant of  $1.5\mu s$ ). A multichannel analyzer is used to acquire the amplifier's output, providing in this way the number of counts for each chan-

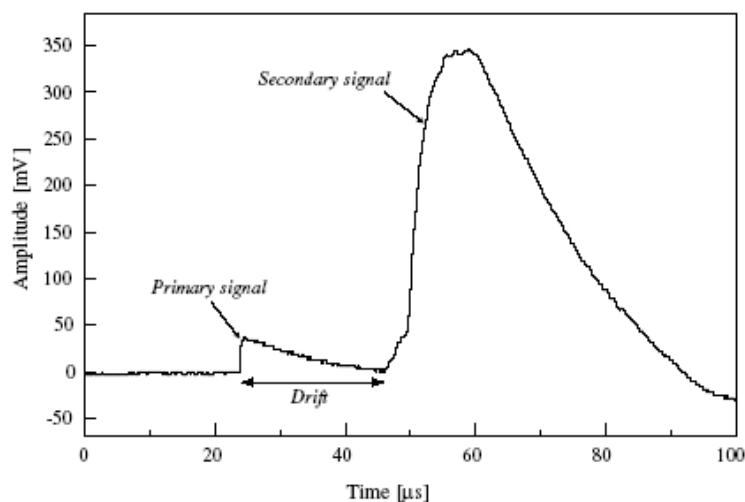


Figure 3.12: Typical peamplified signal

nel. Using different amplification values the readout system can measure the scintillation spectra at different scales. In fig. 3.13 a typical dark spectra acquired using the MCA is shown. The gaussian peak, due to the electron emission by the photocathode, and the exponential noise, due mainly to the electron emission by the dynode chain, are clearly visible. The single photoelectrons response (SER) is used to evaluate the average  $phe/ADC$  channel factor as function of the gain of the chain PMT- preamplifier - amplifier and to express the amplitude of the signal  $S_1 - S_2$  as number of photoelectrons. When the extraction fields are turned on, the light produced is the result of both the scintillation in liquid and the luminescence in the gaseous phase. The previous setup is used essentially to acquire the dark spectra of the PMT in order to measure its gain (due to its small amplitude the SER spectra is not affected by the presence of proportional light that has typically an higher amplitude). In order to acquire the complete signal, the output of the Canberra preamplifier is splitted and sent to a digital scope (Lecroy LC534AM) with a sampling rate of 25 MHz and a 8 bit dynamical range. The trigger is defined as  $\max(S_1, S_2) > threshold$ , in this way it is possible to trigger on both signals. For this reason, the trigger delay is in the middle of an acquisition window of  $200\mu s$ . The recorded data are then transferred using a GPIB board to a personal computer for the analysis.

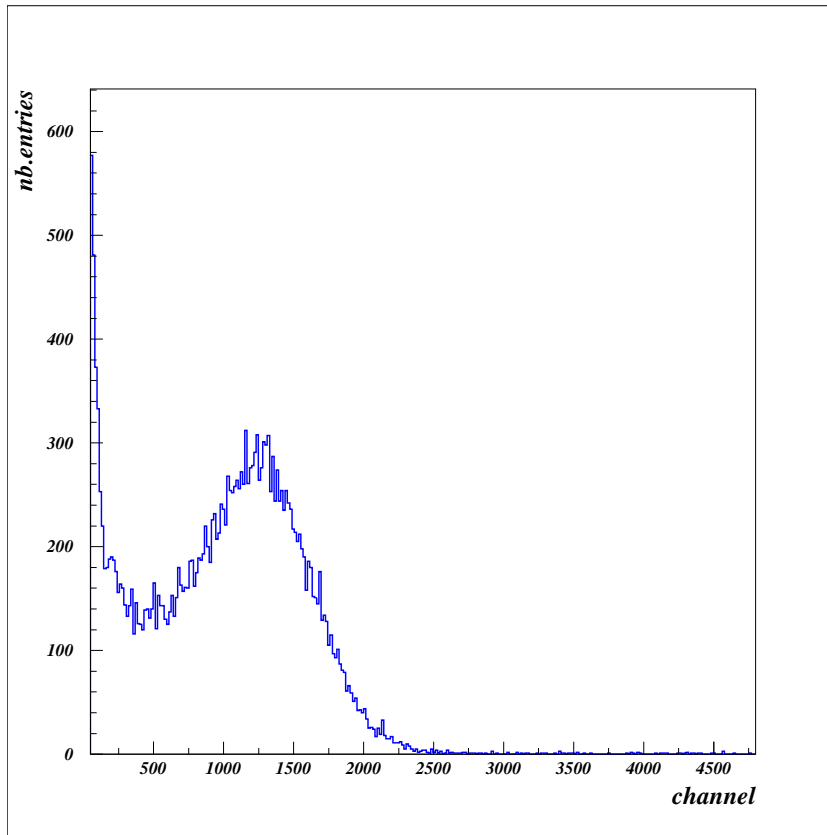


Figure 3.13: Typical dark spectra signal acquired using the MCA. The gaussian peak due to the electron emission by the photocathode is clearly visible with the exponential noise.

### 3.7 RESULTS OF THE PRELIMINARY TESTS

A really large amount of tests has been performed during the *R&D* period at Pavia University, and a really large amount of data has been collected, allowing to improve the set-up of the chamber in order to implement the events discrimination techniques. The aim of this section is not to report all the *R&D* activity, but it is to show few results that have allowed to prove the effectiveness of the proposed technique. It was shown the possibility of the particle discrimination based on the ratio  $S_2/S_1$  between the amplitude of the secondary and primary scintillation. In fig (3.14) two different events are presented. The first one is characterized by a large  $S_1$  and a smaller  $S_2$ , while the second has a tiny  $S_1$  followed by a huge  $S_2$ . Those behaviors agree with the hypothesis of different amount of scintillation and ionization produced in the sensitive volume. Only in the first case the event seems to be

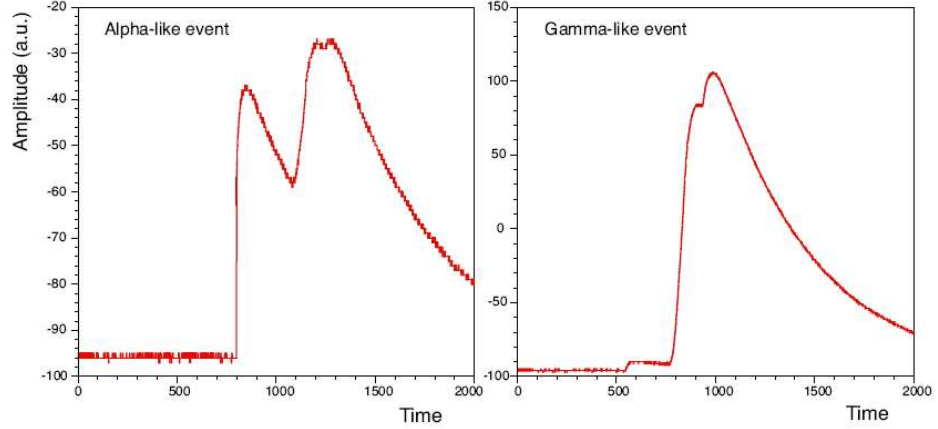


Figure 3.14: Different shapes characterize  $\alpha$ -like and  $\gamma$ -like events. In the first case a large  $S_1$  is followed by a smaller  $S_2$ , while in the second case there is a tiny  $S_1$  is followed by a huge  $S_2$ . The last little third peak is related to the collection of the electron on the last grid.

characterized by an high charge recombination, thus reducing the number of free electrons and increasing the production of primary scintillation photons. Different measurements have been conducted for different electric fields. The following results have been obtained using the following values for the electric fields

	<i>Field(kV/cm)</i>
$V_{drift}$	1.0
$V_{extraction}$	2.14(gas) - 3.2(liquid)
$V_{multiplication}$	3.5

This configuration has been chosen in order to have an high extraction and multiplication efficiency, avoiding, in the same time, any possible discharge problem <sup>5</sup>.

In fig. (3.15) the scatter plot of  $S_2/S_1$  vs  $S_1$  shows different populations. Two sets of events localized in two completely separated areas of the plot are easily recognizable. The first one is characterized by  $S_1 < 800$  and a ratio  $S_2/S_1 \approx 10.9$ , while the second one has  $S_1 > 2000$  and a ratio  $S_2/S_1 \approx 0.194$ . The experimental data are consistent with different interactions produced by  $\gamma$  and  $\alpha$  particles. In case of heavily ionizing  $\alpha$  particles, the amount of ionization charge produced is enough to neglect locally the external drift field.

<sup>5</sup>It should be noted that the electric field is not uniform in the extraction region, due to the different permittivities of the liquid and gaseous phases. Thus the field in liquid has a lower value respect to the value in the gaseous phase.

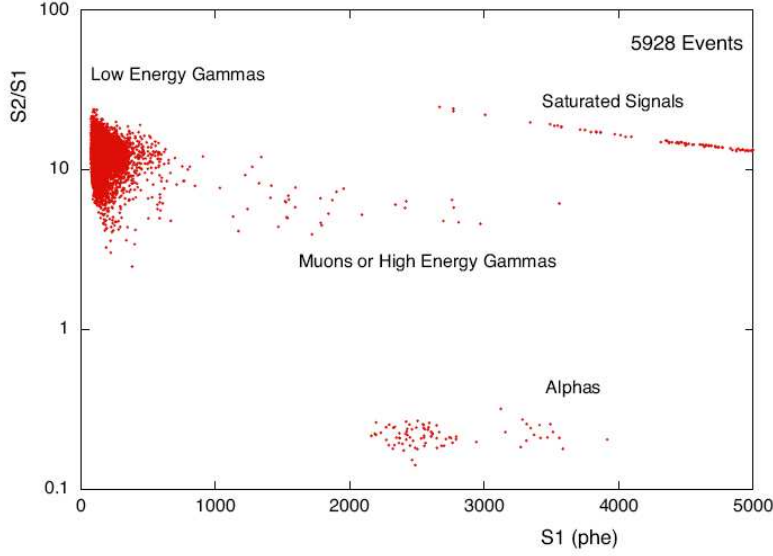
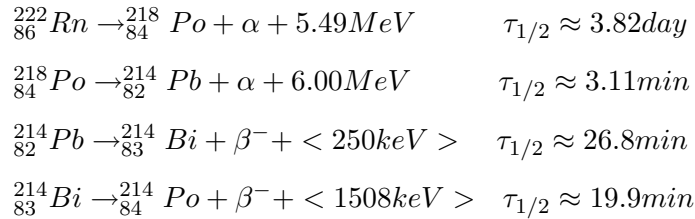


Figure 3.15: Bi-dimensional plot of the ratio between secondary and primary scintillation vs. primary scintillation (5928 events acquired without sources). As we can see, different areas are populated according to the different types of interactions

Thus the recombination process is widely favored, producing in this way an enhancement of the scintillation light. It has been possible to show that in case of electronic ( $\gamma$  or electrons) interaction the ratio  $S_2/S_1$  is strictly dependent on the value of the external drift field, which has influence on the recombination process, while in the  $\alpha$  interactions the ratio  $S_2/S_1$  is essentially constant for fields of the order of  $1keV/cm$ . Other types of events in the scatter plot can be easily identified. A population (approximately described by the condition of  $(S_1 + S_2 = const)$ ) could be referred to high energy events saturating the oscilloscope dynamical range, while few diffuse events are probably due to high energy photons and cosmic rays. The experimental data regarding the  $\alpha$ -like interactions are consistent with the characteristic decay chain of the  $^{222}Rn$ , coming from the little contamination in the freshly produced industrial Argon:



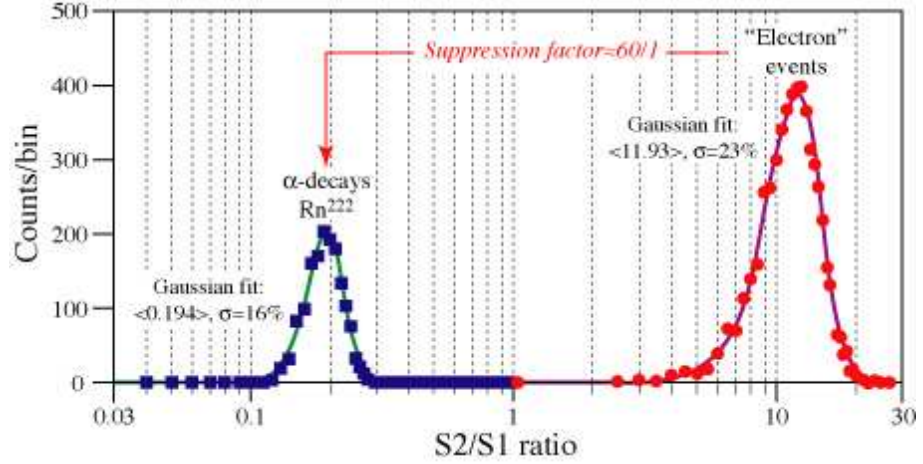


Figure 3.16: Histogram of the ratio  $S_2/S_1$  for the events identified as  $\alpha$ -like and  $\gamma$ -like. A suppression factor of the order of  $\approx 60$  characterizes the  $\alpha$ -like and makes a clear separation between the two families.



This assumption is provided by the disappearing of the  $\alpha$ -like events according with the  ${}^{222}\text{Rn}$  chain decay time. Moreover two cluster of events detected in the energy spectra are consistent with the relative position of the  $\alpha$  particle emitted according to the previous decay chain: two peaks can be detected in the spectra, the first one connected to  $\alpha$  particle coming from  ${}^{222}\text{Rn}$  decay (mean energy  $\approx 5.49\text{MeV}$ ) and the second one produced by the  ${}^{218}\text{Po}$  (mean energy  $\approx 6.0\text{MeV}$ ). In this way the  ${}^{222}\text{Rn}$  can provide the possibility of an energy calibration. In fig (3.16) the histogram of the distribution of the ratios between secondary and primary scintillation is reported. As we can see data are well fitted by a gaussian fit. A suppression factor of the order 1 : 60 characterizes the  $\alpha$ -like events respect to  $\gamma$ -like events. Considering  $\alpha$  particles of  $5.7\text{MeV}$  of mean energy and  $1\text{MeV}$  electrons, the observed suppression factor is in agreement with the theoretical prediction obtained using the average values for the energy loss, for pair ion-electron creation and for photon emission (see eq (3.1)).

The previous measurements have been performed for different values of the multiplication field<sup>6</sup>. As we can see from fig. (3.7) both  $\gamma$ -like and  $\alpha$ -like events show similar behaviors, thus the suppression factor is not dependent onto the multiplication field  $E_m$ . The only effect is the change of the multiplication gain  $\rho(E_m)$  expressed as ( $\text{photons} \cdot \text{electrons}^{-1}$ ), as shown in fig.

<sup>6</sup>the fields configuration adopted was able to provide a total electronic transparency of the grids.

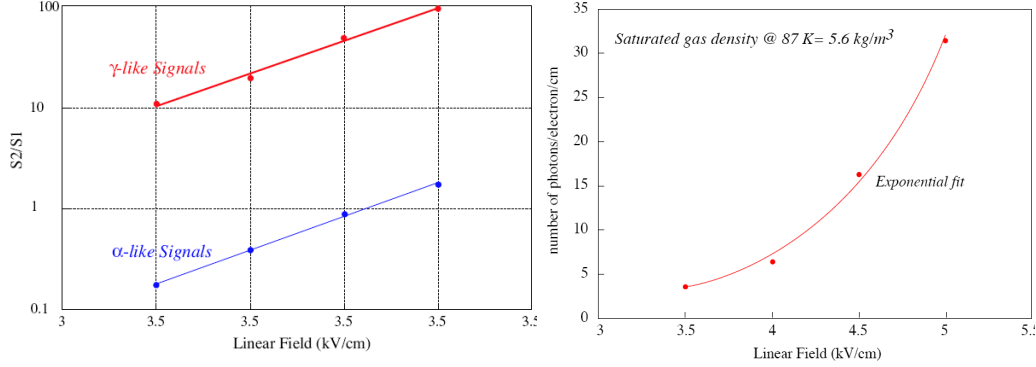


Figure 3.17: Left: values for  $\gamma$ -like and  $\alpha$ -like ratios  $S2/S1$ , as a function of the value of the linear multiplication field. Both signals evidence similar behaviors. Right: Multiplication gain expressed in  $phe/electron/cm$  as function of the field.

(3.7) for the  $\alpha$ -like events. The number of emitted photons shows a roughly exponential growth as a function of the applied electric field.

Considering that the ratio  $S2/S1$  can be expressed as

$$\frac{S2(E_m)}{S1} = \frac{n_{e,\alpha} \cdot \rho(E_m) \epsilon_g}{n_{ph,\alpha} \cdot \epsilon_l} \quad (3.2)$$

where  $E_m$  is the multiplication field,  $\epsilon_{l,g}$  the collection efficiencies for photon produced in liquid and gaseous phase and  $n_{e,\alpha}-n_{ph,\alpha}$  the number of free electrons and photons produced in liquid Argon by  $\alpha$  particles<sup>7</sup>; it is possible to estimate the number  $N = \rho(E_m)/2cm$  of ( $photons \cdot electrons^{-1} \cdot cm^{-1}$ ). The resulting observed light signal, due to electrons extracted in the gas, is in excellent agreement with predictions of geometrical light collection. The collection efficiency  $\epsilon_{l,g}$  for photons produced in liquid and gaseous phase has been investigated through a MonteCarlo simulation (see fig. 3.18 ), reproducing the propagation of photons in the detector. The estimated average values, expressed in photoelectrons/photon, are<sup>8</sup>  $\langle \epsilon_l \rangle = 0.088 \pm 0.012$  and  $\langle \epsilon_g \rangle = 0.118 \pm 0.014$ .

Concluding, the contemporary detection of both scintillation and ionization yields is strictly dependent on the nature of the impinging particle and the test chamber has shown the effectiveness of the proposed technique in the separation between electronic and  $\alpha$  interactions. This separation should

<sup>7</sup>According to the results of section 3.3, an  $\alpha$  particle with a kinetic energy of 5.7MeV should produce about  $2.4 \times 10^5$  electrons. Due to the recombination process, at  $1kV/cm$  only  $5.2 \times 10^3$  survive. Assuming an average energy loss for photon emission of  $W'=27.5eV$ , an average number of  $2.1 \times 10^5$  is produced

<sup>8</sup>A reflectivity of 95% for the Mylar-TPB layer and a PMT efficiency of 20% have been assumed.

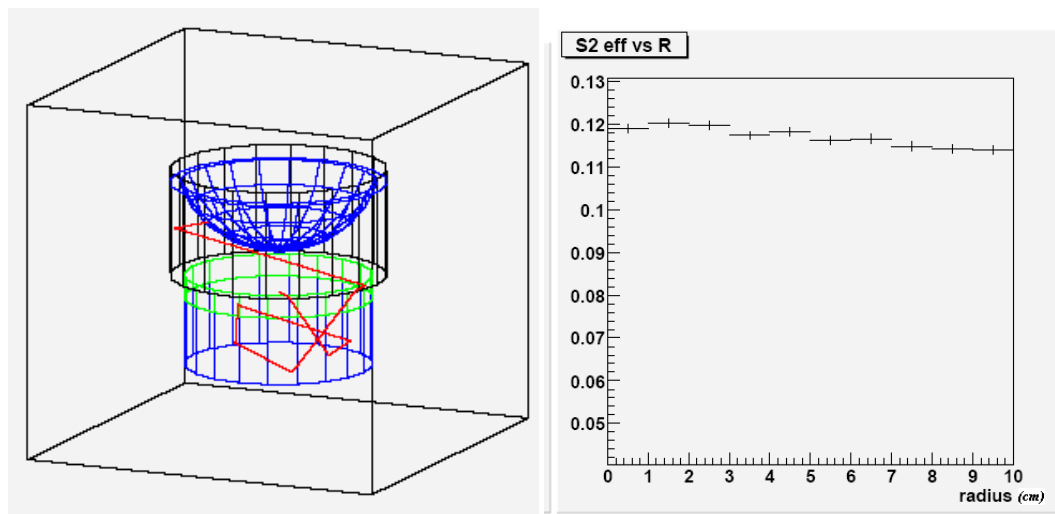


Figure 3.18: Left: example of a 3D view of the path of a photons produced during the luminescence process in gas in the 2.3 prototype. Right: detection efficiency as function of the distance from the central axis for photons produced in gas.

be even larger in case of electrons and nuclear recoils. In fact, the total recombination effect for  $\alpha$  particles is a superposition of high recombination occurring in the high density ionization area, and of a reduced recombination occurring in the surrounding area (penumbra). In case of a slow nuclear recoil, the higher ionization density should enhance the recombination, producing a ratio  $S_2/S_1$  lower (or almost equal) than the one measured for the  $\alpha$  particle (although in a different energy range).

## 3.8 WARP 2.3L CHAMBER AT LNGS

### 3.8.1 SETUP

During the data taking at LNGS both the PMT of 2" and 3" have been used. For details on the EMI photomultipliers see chapter 5. Seven 2 inch phototubes (mod. Electron Tubes EMI D743, with sand blasted glass flat window) have been initially used. They are arranged on a hexagonal centered grid with nominal spacing of 65mm, placed on top of the sensitive volume, in the Argon gas phase, with the PMTs windows at about 40mm from the last grid. A low threshold trigger is built using the coincidence between signals coming from different PMTs. Moreover, the use of more than one phototube gives in principle the possibility of a rough localization of the interaction in the (x-y) plane normal to the drift direction, since the PMT facing the point of production of the scintillation light in the gaseous phase



Figure 3.19: 3D-representation of the test chamber as used during the LNGS background measurements. As we can see the general set-up has changed and an array of 7 PMTs has been used.

detects a higher number of photons. Using the information of the drift time between the primary and the secondary signal, it is possible to get the 3d location of the interaction inside the chamber, with a granularity in the x-y plane depending on the phototubes dimensions. In this way, it is possible to use this information to define a fiducial sensitive volume, thus giving the possibility to remove events typically associated with materials radioactivity. Moreover, those smaller PMTs have an higher quantum efficiency respect the 8" used previously, in this way it is possible to balance the decreasing in the photocathode coverage. The aim of the measurements performed at LNGS was the estimation of the background and of the internal radioactivity. In order to do this, a number of changes have been performed on the setup described previously. A smaller and inner sensitive volume (1.87l) has been chosen to increase the distance between the border of the volume and the racetracks in order to avoid any drift field dis-uniformity. The major improvement to the external setup is a 10cm lead shield surrounding the whole external dewar, to minimize the number of particles coming from the

external room and to estimate the internal radioactivity. To maximize the radiochemical purification an Hopkalit cartridge has been used instead of standard Oxisorb. This new filter offers performances similar to the previous one regarding the oxygen purification, allowing a long electron lifetime, but it decreases the traces of heavy metals and other contaminants, thus reducing the internal  $\gamma$  and  $\beta$  emissions. Starting from August 2005 a recirculation system has been implemented at LNGS in order to allow a longer period of data taking. A little evaporation of the liquid is obtained through the heat dissipation of resistance placed in the chamber, and the overpressure is used to drive the gas Argon in a purification cartridge placed outside the chamber. The system has been able to avoid the necessity of the LAr replacement, allowing a continuous data taking.

To improve the wave length shifting during the measurements, the liquid Argon has been doped with Xenon at a concentrations  $< 1\%$  in order to shift from  $128nm$  to  $175nm$ . In this case, instead of standard VME + TPB system, a PTFE diffusive layer has been adopted (estimated reflectivity 88% at  $175nm$ ).

### 3.8.2 DATA ACQUISITION

The readout system has been changed to take in account the presence of seven PMTs. The system described in the previous section was preserved to get the possibility of the SER measurement (needed to calculate the gain of each photomultiplier) and to detect the primary scintillation spectra of one or more PMTs. A new system has been added in order to manage the coincidence of the signals of many PMTs and to implement an efficient trigger logic necessary to identify a few number of nuclear recoils beyond a large number of  $\gamma$ -like events. The general layout of the trigger is shown in fig 3.20. Two levels of trigger logic have been implemented. The first level is based on a majority condition: the trigger requests at least 4 PMTs over the threshold in order to allow the acquisition of the signals. To implement this trigger logic, the signals coming from the last dynode of each PMT are preamplified by a fast inverting preamplifier with a gain set at about a value of 100, and then the signal is discriminated using a threshold of 1.5 photoelectrons. To have uniform conditions all the PMTs have been equalized to the same gain. The NIM output of each discriminator is sent to a coincidence module and the request of at least four PMTs over threshold is applied. The NIM output of the coincidence board is the trigger signal sent to a trigger board CAEN V793. At the same time the anodic output of each PMTs is acquired and shaped using the Camberra 2005 charge preamplifier described in previous section. A board CAEN V789 is used in order to digitalize the signal (the board has been modified excluding the preamplified section that has been replaced by fast amplifiers). The signal is splitted

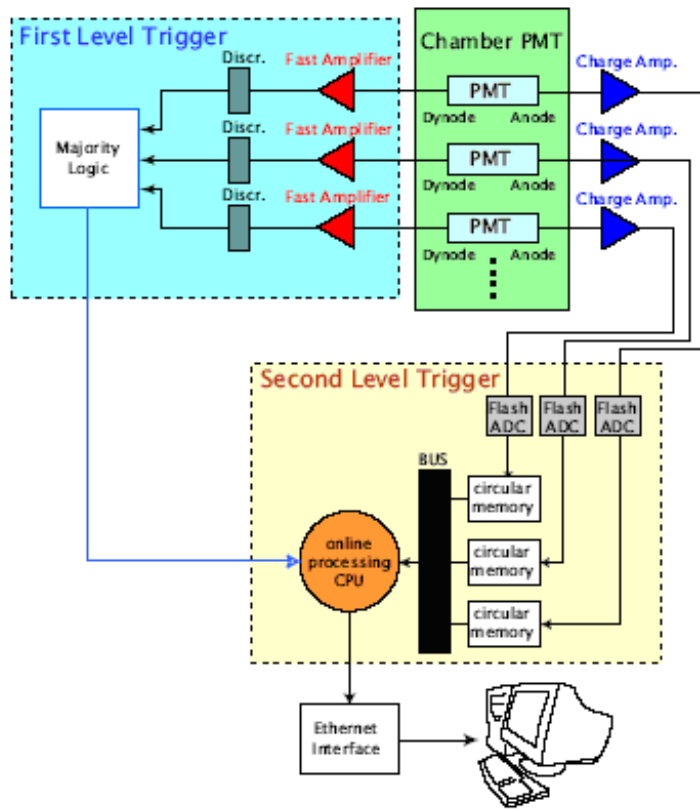


Figure 3.20: Layout of the data acquisition and readout system as implemented at Gran Sasso laboratory.

in two channels, one of those has been attenuated of a factor 10. Both signals have been digitalized using a Flash ADC (10 bits dynamical range and 20 MHz sampling frequency) and then they have been recorded into a circular buffer of  $4kB$  (about  $204\mu s$  at 20MHz) in order to record an event with the maximum drift time ( $50\mu s$  about). The gain of the chain PMTs-premplifier is equalized to obtain a conversion factor of 10 ADC count for each photoelectron in the high gain channel.

Once this board has received the input signal from the first level trigger, data are transferred to a mass storage disk of a personal computer hosted in the control room.

### 3.9 RESULTS AT LNGS

The aim of the measurements at LNGS was at first the study of the background due to environmental and internal radioactivity. First of all, calibra-

Source	Activity ( kBq)	$\gamma$ energy (KeV)
$^{57}\text{Co}$	1.1	122(90%) - 137 (10 %)
$^{137}\text{Cs}$	17	662
$^{60}\text{Co}$	19	1173(100%) - 1332 (100 %)

Table 3.2:  $\gamma$  emitting sources used for the calibration of the detector.

tion measurements have been performed using  $^{57}\text{Co}$ ,  $^{137}\text{Cs}$  and  $^{60}\text{Co}$  (tab 3.2)  $\gamma$  sources located in the external LAr bath, in order to use the average photoelectron yields to calibrate in energy the primary scintillation for  $\gamma$ -like events. As stressed before, the single photoelectrons response (SER) is used to evaluate the average  $phe/ADC$  *chnannel* factor, thus the estimation, expressed as number of ADC channels, of Compton edges or photoelectron peaks can provide the energy calibration in terms of  $phe/keV$ . This measurements is clearly function of the experimental setup, depending for example on the reflectivity of the diffusive layer, on the values of the electric fields and on the photo-cathodic coverage<sup>9</sup>. Without fields, photoelectron yields of the order of  $1phe/keV$  have been obtained using the sources of table (3.2).

During the data taking, an external 10cm thick Pb shielding completely surrounding the Ar dewar has been installed to investigate the internal radioactivity. The background level, achieved in the underground environment with the help of the shielding, was sufficiently low to permit the detection of the main components of the internal radioactivity present inside liquid Ar, clearly identified as coming come from  $^{222}\text{Rn}$  and  $^{39}\text{Ar}$  decays.

### 3.9.1 OBSERVATION OF THE INTERNAL $^{222}\text{Rn}$ AND $^{39}\text{Ar}$ SIGNALS

In fig (3.21) the comparison of the background spectra acquired with (red histogram) and without (blue histogram) the lead shield are shown, with the vertical scale expressed in counts/keV/sec and the horizontal scale in electron equivalent energy. Two peaks at energies greater than 3.0MeV are clearly visible and they could be explained by the  $^{222}\text{Rn}$  decay chain (section 3.7). The first peak at lower energy should be due to the  $\alpha$  particles produced by  $^{222}\text{Rn}$  and by  $^{218}\text{Po}$ , while the  $\beta - \alpha$  decays of  $^{214}\text{Bi}$  and  $^{214}\text{Po}$  can explain the second peak. Using those peaks to evaluate the quenching factor of particle respect to the electron of an equivalent energy, it is possible to obtain a value of 0.75. The contamination of  $^{222}\text{Rn}$  dissolved in liquid Argon inside the active volume is always present from the filling of the chamber, and the reduction of its activity according to an half-life of 3.82

<sup>9</sup>moreover the calibration is strictly dependent on the particle scintillation yield, as stressed in section (3.3)

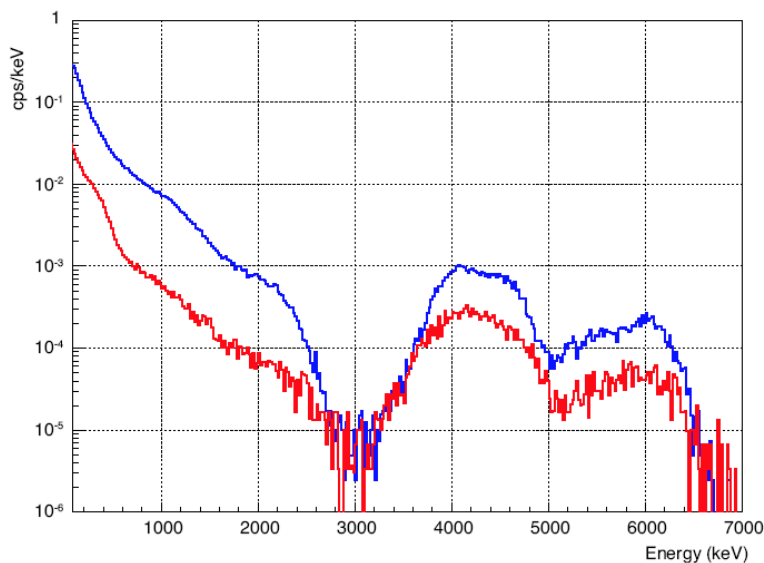


Figure 3.21: Background spectra acquired at LNGS with (red) and without (blue) lead shield. In both cases the decay peaks of the  $^{222}\text{Rn}$  internal contamination are clearly visible.

days gives the different amounts of the amplitude of the peaks between two different spectra. At lower energy ( $< 2.5\text{MeV}$ ) the background events are mainly produced by environmental particles interacting inside the active volume. In fig (3.21) and (3.22) the peaks at  $1.2\text{MeV}$  and  $2.4\text{MeV}$  on the spectrum acquired without the external shielding, could be explained by the Compton edges of the  $^{208}\text{Tl}$  ( $2382\text{keV}$  from a line at  $2615\text{keV}$ ) and  $^{40}\text{K}$  ( $1242\text{keV}$  from line at  $1460\text{keV}$ ). The remaining background in this energy range is also due to  $\gamma$ -emission from  $^{222}\text{Rn}$  and its daughters, which is affecting both setups with and without shield, whose magnitude depends on different levels of contamination at the time of the spectra acquisition (the typical event rate of the internal  $^{222}\text{Rn}$  signal for "fresh" Argon filling of the  $2.3\text{l}$  chamber is about  $1.2\text{Hz}$ ). In this way the internal  $\gamma$ -background from  $^{222}\text{Rn}$  and its daughters can be estimated taking into account its activity decreasing.

As shown in fig (3.23), a subtraction of two energy spectra, acquired at 8 days of distance during the same run and normalized to the counting rate of the peaks, reveals the full contribution of the  $^{222}\text{Rn}$  decaying chain alone. This contribution regards a large parte of the detected energy range, due to contemporary production of  $\alpha$  and  $\beta$  particles of different energies. According to the acquired spectra, it is possible to conclude that the con-

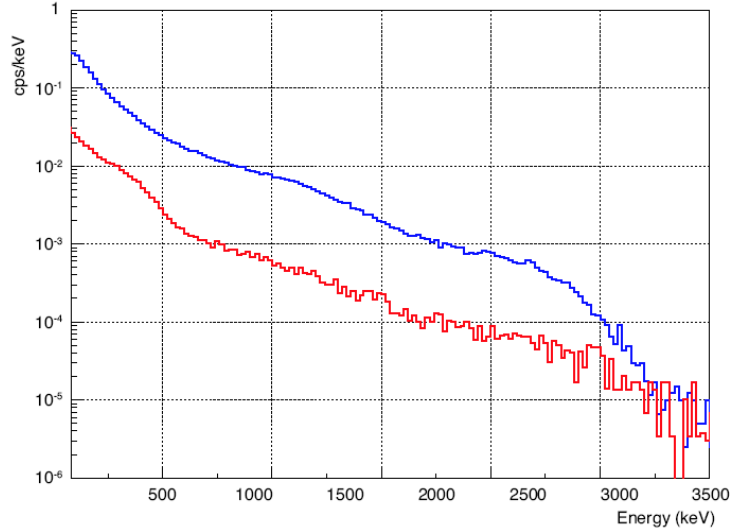


Figure 3.22: Energy spectra in the range  $80\text{keV} - 3\text{MeV}$  acquired with (red) and without (blue) lead shield. Compton edges due the  $\gamma$  emission ( $^{208}\text{Tl}$  and  $^{40}\text{K}$ ) are clearly visible in the spectra without shielding.

<i>Energy(keV)</i>	<i>Rates(Hz) (No shield)</i>	<i>Rates(Hz)(Shield)</i>	<i>Supp. factor</i>
100-500	35.4	4.15	0.12
500-1000	6.5	0.56	0.09
1000-1500	2.22	0.17	0.08
1500-2500	0.78	0.081	0.1

Table 3.3: Total counting rates observed with and without shield in different energy ranges.

tribution of the  $^{222}\text{Rn}$  induced background is not negligible, however, due to the  $^{222}\text{Rn}$  lifetime, it can be strongly reduced during the data taking by waiting for a sufficiently long time after the filling.

From the comparison of the background spectrum acquired with the lead shielding with the  $^{222}\text{Rn}$  induced background spectrum (fig. 3.24), it is possible to conclude that the  $^{222}\text{Rn}$  induced is the main background source above  $3\text{MeV}$  of energy, while its contribution is less significant at lower energies.

Below  $3\text{MeV}$  the energy spectra should be caused mainly by environmental  $\gamma$ -rays from  $U$ ,  $Th$ , and  $K$ , coming from materials surrounding the sensitive volume of the detector (air, rock and concrete of the lab). As we

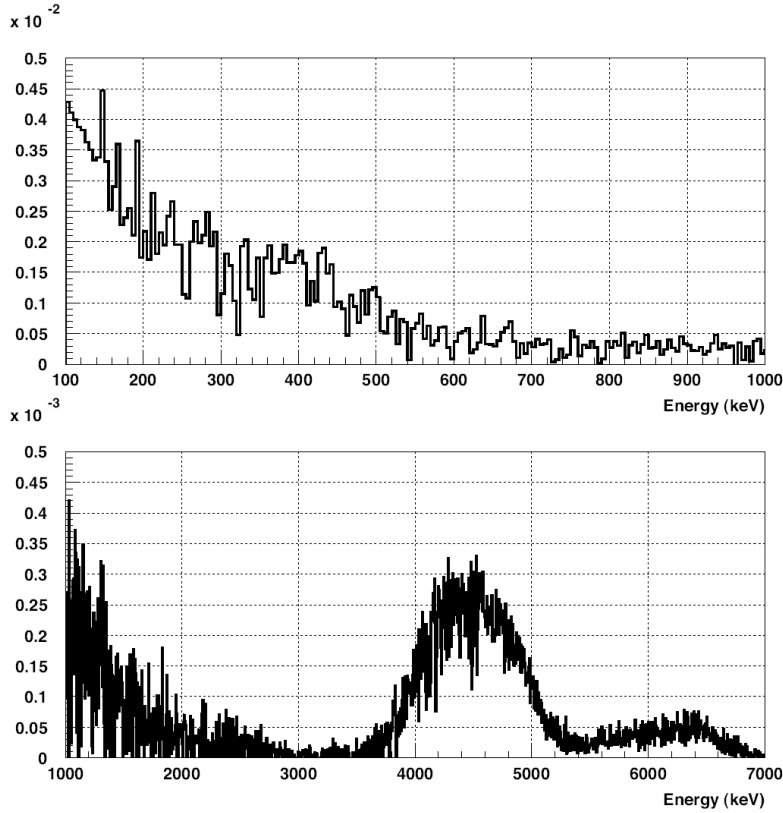


Figure 3.23: Energy spectrum of the events generated by the internal  $^{222}\text{Rn}$  decay chain in two energy ranges (100 – 1000 keV and 1 – 7 MeV), obtained by subtracting by the difference of two spectra acquired at 8 days of distance.

can see from fig (3.22) and table (3.3) the shielding can reduce the event rate of one order of magnitude at all the energies. With the lead shield the dominant contribution is from the shielding itself and from the internal contamination.

Once the subtraction of the internal background from  $^{222}\text{Rn}$  and the environmental  $\gamma$ -ray has been performed, we obtain a residual internal background (Fig 3.25) that is compatible with the  $^{39}\text{Ar}$   $\beta$ -decay (half life 269y, end-point at 565keV and average energy 220keV). It is possible to fit the distribution using the  $^{39}\text{Ar}$  spectrum with end-point at 565keV, and average energy 220keV. Including evaluation of uncertainties, the determination of the activity of  $^{39}\text{Ar}$  is finally  $A_{(^{39}\text{Ar})} = (1.1 \pm 0.4)\text{Bq/l}$  of LAr, or  $(0.76 \pm 0.28)\text{Bq/Kg}$  of Argon. This value is in good agreement with the determination by H.H. Loosli (ref), where the  $^{39}\text{Ar}$  content in natural Argon is

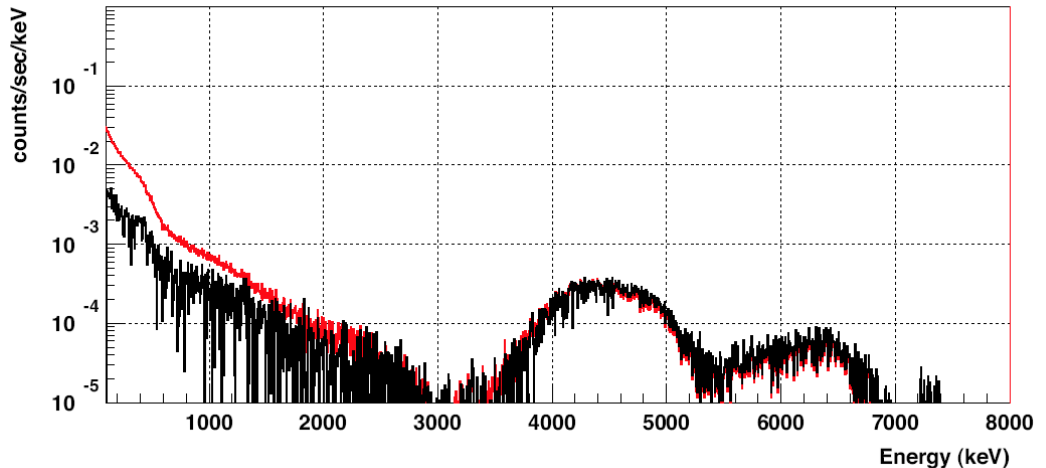


Figure 3.24: Comparison of the background spectra observed with the Pb shielding (red histogram) with the Rn induced background (black histogram) normalizing with  $\alpha$ -peaks rate.

quoted as  $(8.1 \pm 0.3)10^{-16}$ , giving a specific activity in LAr of  $(1.40.05)Bq/l$ .

Finally the excess of events at of low energy could be due to the residual activity in the Pb shielding.

### 3.10 ARGON RECOIL EVENTS SELECTION

In order to maximize the rejection power of the  $\gamma$ - background, two independent criteria are used. The first one is based on a pulse shape discrimination and it is used to identify the density of ionization of the emitted scintillation light  $S_1$ . The measurements with the 2.3l chamber proved that it is possible to get a rejection power well in excess of  $10^{-4}$ . The second one, used as well during the preliminary tests in Pavia, is based on the different amount of ionization extracted from the liquid to the gas, due to the different recombination probability. This criterion on the S2/S1 ratio, showed a rejection power of the order of  $10^{-5}$ . It should be possible to apply those criteria at the same time, obtaining in this way an overall rejection factor of the order of  $10^{-9}$ . This level is many orders of magnitudes greater than what has been performed in previous WIMP searches, and it is sufficient to eliminate the possible background due to  $^{39}Ar$  contamination up to the level of 1 event in 100 days.

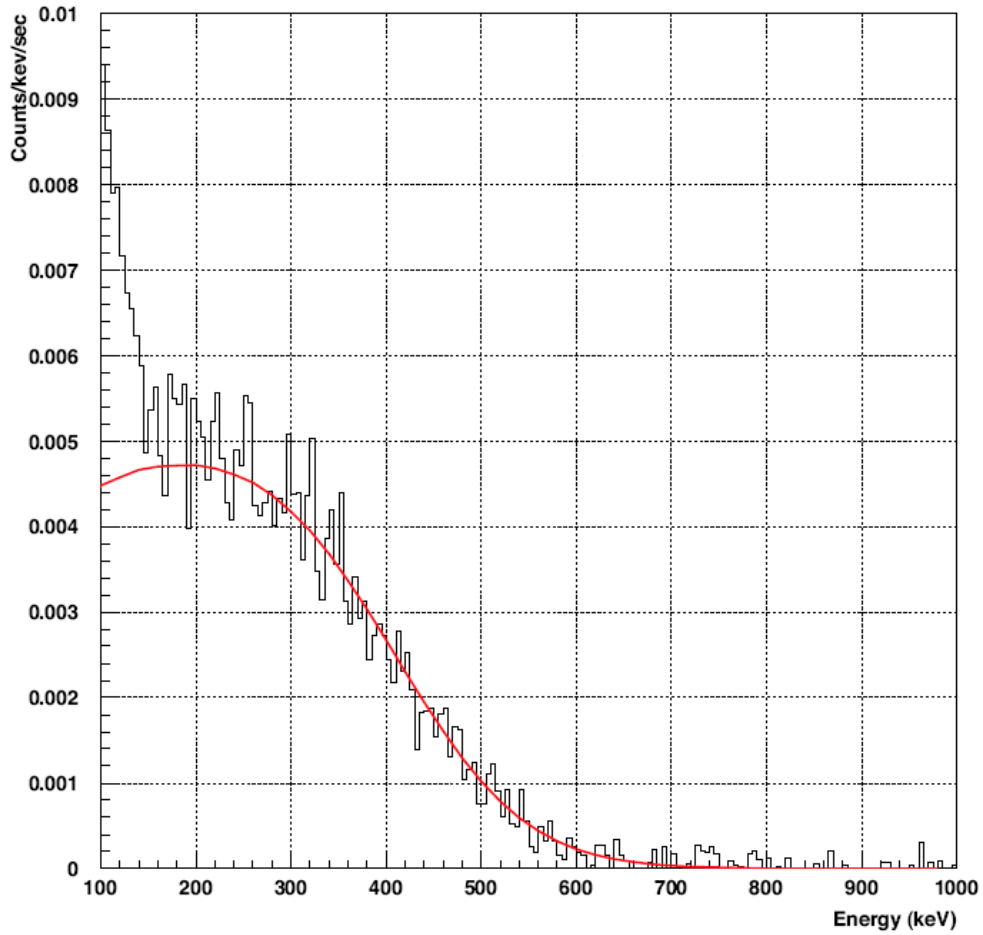


Figure 3.25: Residual signal after subtracting out the time-dependent contribution from  $^{222}\text{Rn}$  background and the external  $\gamma$ -rays signal estimated by the attenuation effects of the Pb shielding. The red line is the expected behavior of  $^{39}\text{Ar}$   $\beta$ -decay.

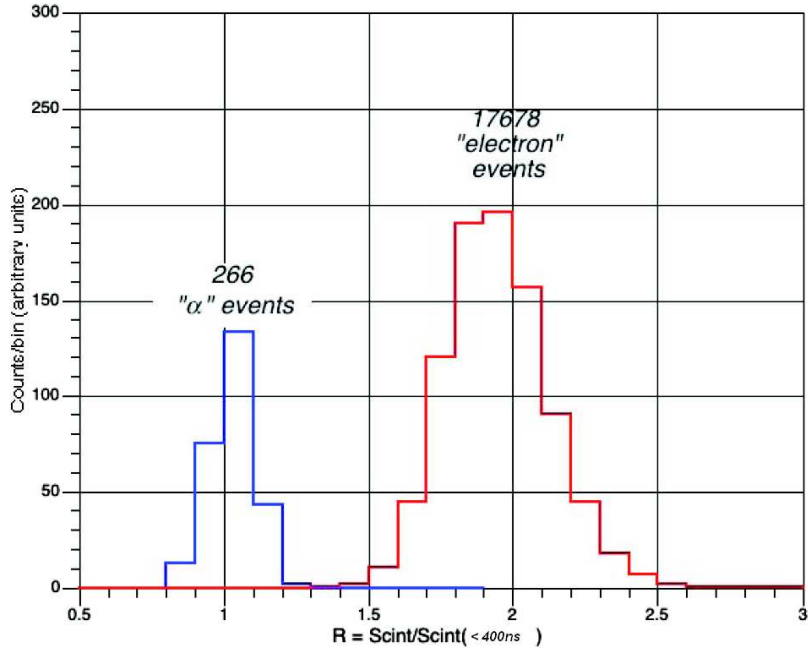


Figure 3.26: Distribution in the ratio  $R = S1(\text{full pulse})/S1(< 400ns)$ . As we can two distributions corresponding to  $\alpha$ -like and *electron*-like interactions are clearly separated

### 3.10.1 PULSE SHAPE DISCRIMINATION

As stressed in section (3.3), the scintillation light is constituted by two different components associated to the singlet  $^1\Sigma_u^+$  state and to the first triplet  $^3\Sigma_u^+$  state of the dimer  $Ar_2^*$ . The radiative transition to the ground state can occur from both states, but with widely different decay constants  $\tau_s = 7.0 \pm 1ns$  and  $\tau_t = 1.6 \pm 0.1\mu s$  (section 3.3). The density of ionization influences the ratios between the amplitudes  $I_s$  and  $I_t$  of those states and the results of Doke et al. indicate  $I_s/I_t = 0.3$  for electrons,  $I_s/I_t = 1.3$  for  $\alpha$ -particles and  $I_s/I_t = 3.0$  for fission fragments (and presumably nuclear recoils), therefore the fast component is dominant for heavy ionizing events. This observation could produce an useful criterion to get an efficient discrimination of the events, thus an evaluation of this type has been performed onto the acquired data. The time dependence of the prompt scintillation light emission was observed in the acquired data, analyzing the  $^{222}Rn$  contamination. Selection is done using an automatic programme, followed by visual inspection of a small fraction of events of more complicated origin. The acquisition uses DAQ system together with the digital scope, in which the integrated sum of the photomultipliers is recorded every  $200ns$ .

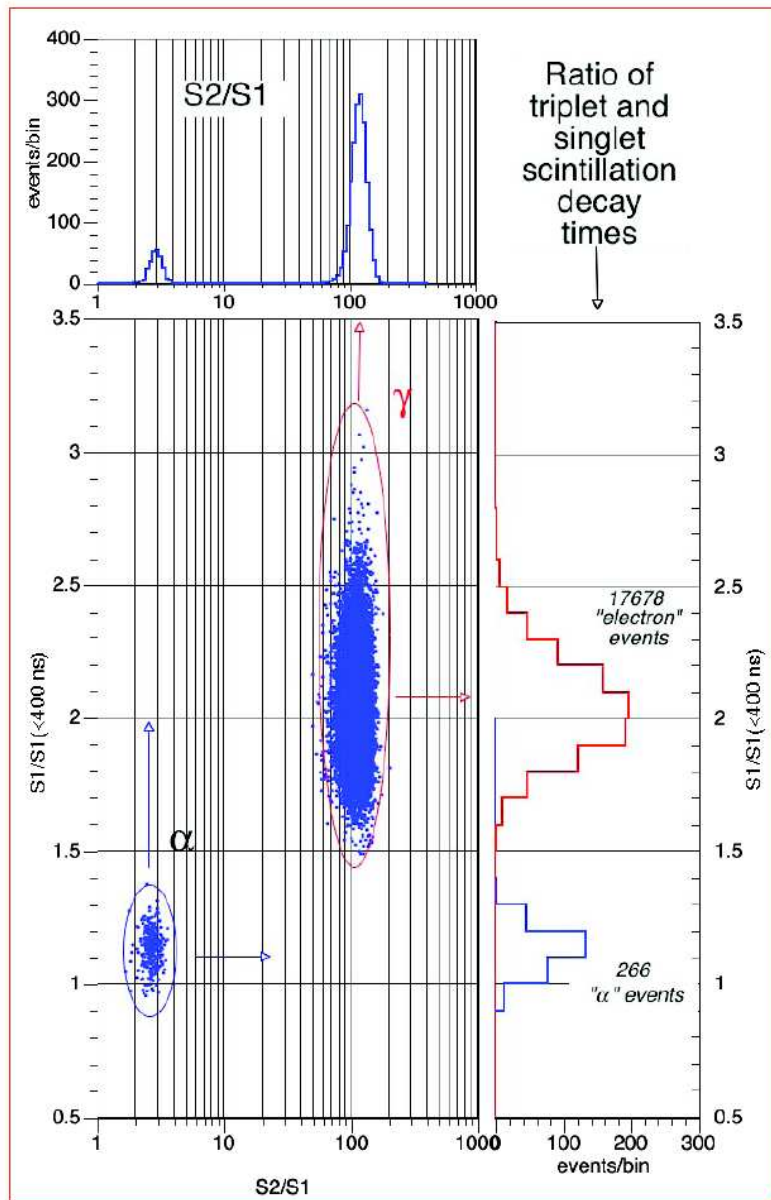


Figure 3.27: Correlation between the two particle identification methods (the one based on  $S2/S1$  (abscissa) and the other based on the shape factor on the prompt scintillation signal  $S1$ ): as we can see there is a perfect agreement between the two independent criteria.

Due to lack of synchronization between signals and clock, the short lived signal is identified as the recorded signal over the first 2 bins (400ns) of the shape recorder; in this way it is possible to contain the totality of the fast component and only a fraction of the slow triplet component. The use of a faster sampling could improve the accuracy of such type of analysis. Defining  $R = S1/S1_{(<400ns)}$  the ratio between the total amount of the primary scintillation signal and the fraction of scintillation during the first 400ns, the distribution of  $R$  measured for scanned events clearly shows the separation between  $\alpha$ -particles events from electron-like events. Two completely separated distributions, respectively of 266 and 17678 events, are shown (fig 3.26). The ratio is in agreement with those indicated in literature (Doke et al.)  $I_s/I_t = 1.3$  for  $\alpha$ -particles and  $I_s/I_t = 0.3$  for electrons, despite of the using of the drift field at 1kV/cm in our measurement.<sup>10</sup>

It is possible to verify that the events identified as  $\alpha$ -like or electron like events using the pulse shape discrimination are identified in the same way, using a selection based on the ratio of  $S_2/S_1$ . The two-dimensional plot (fig 3.27) of  $S_2/S_1$  shows two well separated peaks, indicating therefore the perfect agreement of both different techniques at least at the measured level of  $\cong 17'000$  "electron like events". In this way, due to the different phenomenologies on which the criteria are based, it should be possible to apply both methods independently, obtaining a probability of a misidentification of an electronic event as nuclear recoil event smaller than  $10^{-8}$

### 3.11 PRELIMINARY RESULTS ABOUT NUCLEAR RECOILS IDENTIFICATION

Data recorded during 13.4 days of live time in the run done in June 2005 have been analyzed looking for Recoil-like events. A total amount of  $6.5 \times 10^6$  triggers have been collected and 578 recoil-like events have been selected using the previous criteria on the pulse shape discrimination and the magnitude of the ratio of primary and secondary scintillation. In fig (3.28) the primary scintillation light (in numbers of phe) of all the selected recoil-like data, is shown as function of the drift time and it is clearly visible the distribution of the events along the sensitive volume with a clustering of the events on the cathode region. A cut on the drift time can share the total selected events in two sets of 190 recoil-like events inside the fiducial volume and 388 in the cathode region. This peculiar distribution can be explained by the daughter nuclei of the  $^{222}Rn$  decay. Although the  $^{222}Rn$  is uniformly distributed inside the LAr volume, the daughter nuclei are produced into a ionized state. The electric field inside the sensitive volume

---

<sup>10</sup>Old data seem to indicate that only higher values of fields ( $> 6kV/cm$ ) can change the ratio  $I_s/I_t$ .

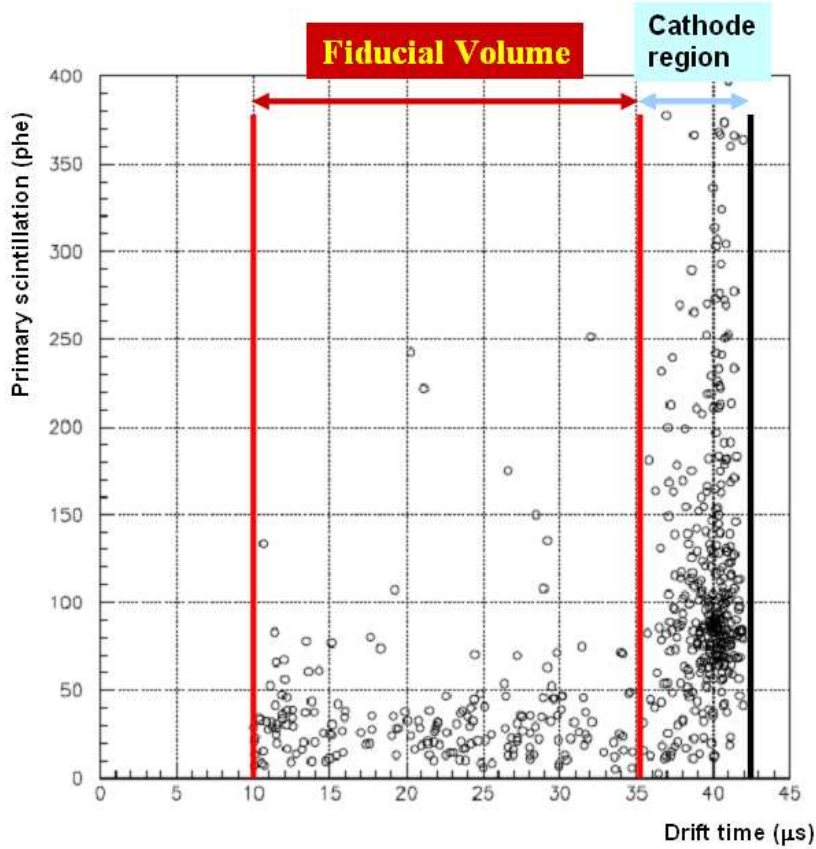


Figure 3.28: Primary scintillation light of the selected recoil data as function of the drift time. The clustering of the events in the cathode region can be produced by the daughter nuclei of the  $^{222}\text{Rn}$  decay.

makes them drift to the cathode where they finally stick. Subsequent decays can produce an  $\alpha$  or  $\beta$  particle travelling in the LAr, or, in the opposite way, the recoil of the nucleus itself toward the sensitive volume. In this way a recoil-like signal is generated close to the cathode position. Those events can be used to get an accurate energy calibration tool. As we can see in fig (3.29), events located on the cathode have an energy distribution which is well fitted by two Gaussians centred at the energies  $E_R$ , as expected from the decays of  $^{218}\text{Po} \rightarrow ^{214}\text{Pb}$  ( $E_\alpha = 6.0\text{MeV}$ ,  $E_R = 110\text{keV}$ ) and  $^{214}\text{Po} \rightarrow ^{214}\text{Bi}$  ( $E_\alpha = 7.7\text{MeV}$ ,  $E_R = 144\text{keV}$ ), giving a yields for recoil-like events  $\approx 0.7\text{phe/keV}$ . The rate of recoil-like events in the cathode region decreases with the live time of  $^{222}\text{Rn}$  (5.28 days) and, in about 20 days after filling, a constant counting rate is reached. In this conditions the signal is presumably produced by Rn emanation from the walls of the

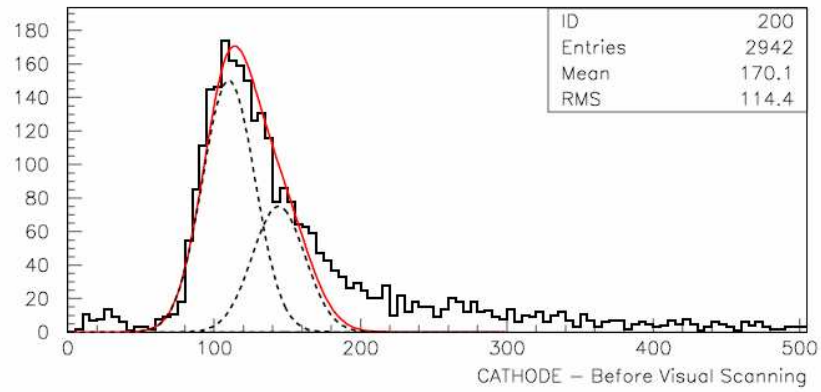


Figure 3.29: Energy distribution of the events located in the cathode region. The histogram is well fitted by two Gaussians centred at the energies expected from the decays of  $^{218}\text{Po}$  and  $^{214}\text{Po}$ .

chamber and from recirculation system.

A preliminary analysis of the event rate and of the shape of the energy spectrum of all recoil-like events inside the fiducial volume gives results compatible with the expected events induced by environmental neutrons inside the laboratory. This work is still in progress.

## Chapter 4

# WARP 100L

### 4.1 INTRODUCTION

The possibility of an efficient discrimination of the interacting particles in LAr has been shown in the last chapter. The technology developed is well suited to compete with other methods of WIMPs search. The liquid Argon technology is mature enough and well supported at industrial level to realize large mass detectors and to provide the radio-purity required in rare events search. Thus it is possible to test the bulk of SUSY parameter space with a new detector of larger mass providing a good background rejection. A 100 litres (140 kg) detector has been proposed by the WARP collaboration, to implement the LAr double phase on a large scale in order to get a sensitivity of  $10^{-8}pb$  for WIMP-nucleon cross section (required to test more favored SUSY models). The detector is now under construction and it will be installed at the Gran Sasso laboratory in 2006.

The general layout of the detector is described in the first part of this chapter. The detector will be realized satisfying severe requirements about the background minimization. Both active and passive shields are designed to this aim, together with an accurate choice of the materials. The last part of this chapter is devoted to present the results of a MonteCarlo simulation, developed in order to study the main possible backgrounds, and to show the expected sensitivity of the experiment.

### 4.2 GENERAL LAYOUT

It is possible to divide conceptually the WARP 100l detector in three parts: the inner detector, the active shield and the external passive shields.

The **inner detector** has been designed in order to reproduce the set-up of the 2.3l test chamber on a larger scale (see fig.4.1)). It contains a volume of 100l of LAr (140 kg) with a gaseous phase, and it is equipped with

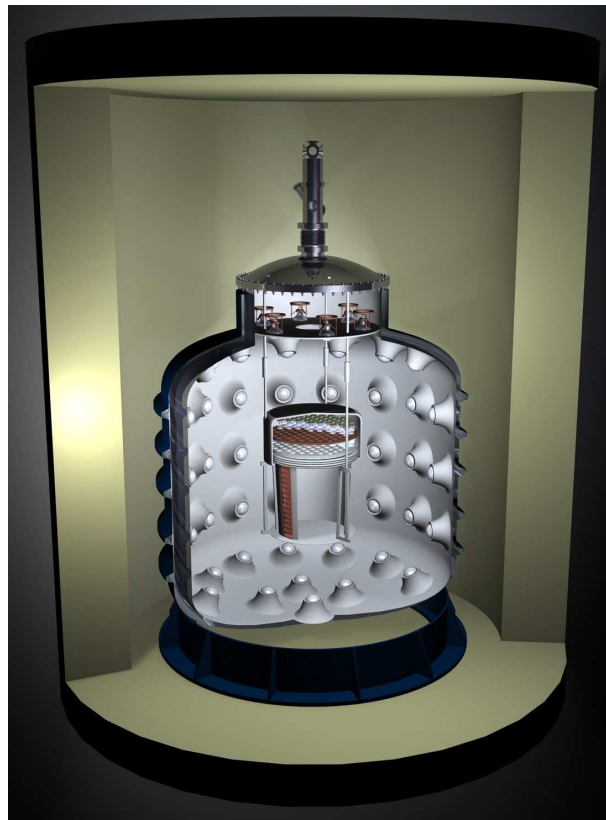


Figure 4.1: Artistic view of the 100l detector. The inner detector, the *LAr* anti-coincidence volume, and the external passive shield are visible.

field-shaping electrodes for the drift field, grids for extraction of ionization electrons from liquid phase and proportional light production in the gaseous phase, and PMTs for the detection of the scintillation light produced in both phases. A global photocathodic coverage of 10% is provided.

The inner detector is suspended at the centre of an additional volume of LAr that has the function of **active veto** in order to reject gamma and neutron backgrounds. The detector is readout by a set of 450 3" PMTs placed on the internal surface of the cryostat with a coverage of the 10% of the total surface. The external volume of LAr has a minimum thickness of 60 cm in all the directions. The inner detector and the active shield are optically separated, so that the events occurring in the outer volume are only detected by the outer PMTs. In the same way of the test chamber, the internal and external surfaces of the inner detector and the internal surface of the active shield are covered with a high reflectivity ( $\geq 95\%$ ) waveshifting layer (TetraPhenylButadiene, deposited on a highly reflective

plastic substrate).

Although the active veto can thermalise neutrons incoming into the detector, a dedicated **external passive shield** surrounding the main LAr cryostat is foreseen in order to reduce a possible environmental gamma and neutron background. Both the inner detector and the active shield are designed in order to use the minimum amount of material. All materials (mainly stainless steel, PEEK, Kapton and PMTs glass) are selected in order to reduce the radioactive contamination as much as possible. Externally a stainless steel (AISI 304L) tank (290 cm large and 445 cm high), with a free volume of 23000 litres is assembled as containment vessel in case of breaking of the main cryostat. This structure will also provide the mechanical support for the assembly of the lead shield.

Two purification systems have been designed to avoid the electronic capture by electronegative impurities in the LAr volume. The first one will be used to purify the commercial Argon during the filling procedure in the same way of the 2.3l chamber test. The only difference is the immersion of the Hopkalite filter in a liquid argon bath; in this way it will be possible to fill the cryostat using directly LAr and avoiding the long time evaporation/recondensation procedure (filling at a constant rate of about 500 l of LAr per hour will be permitted). Moreover, due to out-gassing of the inner materials, a constantly recirculation system is necessary in order to maintain an high electron lifetime during the data taking. On the other way, the overpressure, produced by the continuous evaporation of the liquid in the dewar due to thermal dissipation of the cryostat and the heating of the internal components (PMTs and resistors), will be used by the recirculation system in order to preserve the LAr purity for long periods of data acquisition. The evaporation flux at the top of the cryostat will be purified in a filter and recondensed into a LAr bath and finally injected on the bottom of the cryostat. A recirculation flux of *5litres/hour* at least will be guaranteed. Finally, the cryogenic system includes two external storage dewars, the automatic filling system for the gas recirculation and devices for pressure measuring.

### 4.3 INNER DETECTOR

The general layout of the inner detector has been thought in order to reproduce the test chamber on a larger scale. Due to the presence of the active veto, it is suspended at the middle of the external liquid argon volume. The sensitive volume inside the detector is delimited at the bottom by a stainless steel disk (3 mm thick, 58 cm of diameter) as cathode and at the top by grids of stainless steel wires stretched on an annular stainless steel frame placed just below the surface. Those components, together with a set of field shaping rings, made using copper strips printed on a conical shape

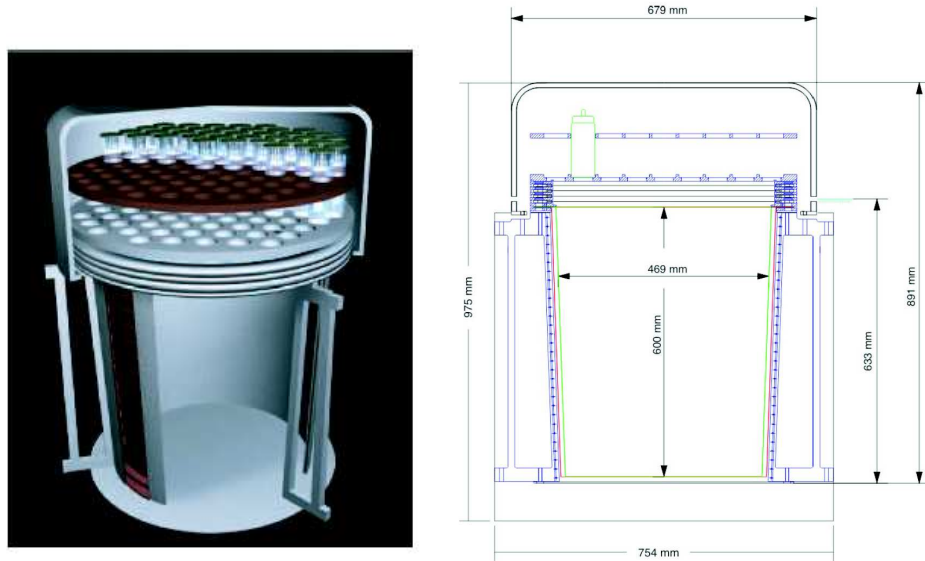


Figure 4.2: Artistic view (left) and dimensional drawing (right) of the inner detector.

Kapton foil surrounding the sensitive volume, provide the uniform drift field necessary for the extraction of the electrons from the liquid phase (see fig. 4.2). This conical layer is grounded using a foil of copper, allowing in this way that no residual field is present in the active veto region. The electrons are then accelerated in the gaseous phase (and finally collected) in order to produce the secondary scintillation signal, using additional grids providing the necessary fields. All the grids are made by a stainless steel ring with an internal diameter of 50 cm and an external diameter  $\cong 58\text{cm}$  (thickness 5 mm) holding a set of stainless steel wires (diameter  $150\mu\text{m}$ ) 4 mm pitched and mechanically tensioned to about 750 g. The grids are separated using PEEK insulators. As in the test chamber the same set of PMTs, placed on the top of the gaseous phase, are used to detect both the primary and the secondary scintillation. It is possible to get the gaseous phase inside the LAr bath using stainless a steel cup placed upside down, and a set of small heating resistances, placed just below the liquid surface, provides the continuous evaporation of the liquid. Small holes (1 mm diameter) in the stainless steel cup, placed at the middle level between the first two grids, can guarantee the correct positioning of the liquid-gas interface at the required level. In this way it is possible to get a continuous recirculation of the LAr in the drift volume. To improve the light collection efficiency, all the inner surfaces are covered with a reflecting/waveshifting layer. A PEEK structure, placed above the last grid in the gaseous phase, supports a total of 37 phototubes

<i>Inner detector</i>	
Overall External Dimensions	<i>Height = 90 cm</i> <i>Diameter = 75 cm</i>
LAr Volume (Sensitive Volume Conical Shape)	<i>Height = 60 cm</i> <i>MaxDiameter = 50 cm</i> <i>MinDiameter = 46 cm</i>
Internal LAr Mass / Volume	<i>152 kg/109 litres</i>
Number of readout 3 <i>inch</i> PMTs	31
Number of readout 2 <i>inch</i> PMTs	6
Total photocathode coverage of the inner surface	10%
Nominal reflectivity of the inner layer	94%
Nominal drift field	1 <i>kV/cm</i>
Maximum drift field	1.5 <i>kV/cm</i>
Operating Voltage at nominal drift field	-70 <i>kV</i> to +10 <i>kV</i>
Operating Voltage at maximum drift field	-130 <i>kV</i> to +10 <i>kV</i>

Table 4.1: Nominal characteristics of the inner detector.

(6 of 2 inches and 31 of 3 inches) allowing a total photocathodic coverage of 10% (see fig. 4.3). The PMTs have quartz or borosilicate window, realized using selected low activity materials. The windows can eventually be coated with TPB in the same manner of the 2.3 *l* test chamber.

Differently from the preliminary test with the 2.3*l* chamber, during data taking pure LAr with no xenon-doping will be used, in order to not modify the scintillation decay constants and to allow the signal shape discrimination.

## 4.4 ACTIVE VETO

Neutron interactions in LAr can produce nuclear recoils in the same energy range of the interesting events produced by WIMPs interactions. Moreover, differently from the electronic background (due to  $\gamma$  and  $\beta$  emission), neutron background produces exactly the same signature of the interesting events and cannot be easily rejected. The only difference is the higher total cross section for interaction  $n - Ar$  respect to the cross section  $\chi - n$ , thus neutrons can produce multiple interactions in the detector. In this way, to reduce this possible source of background, an active veto shield surrounding the sensitive volume has been designed with the main aim of the rejection of those events that have an interaction in both the inner and outer LAr

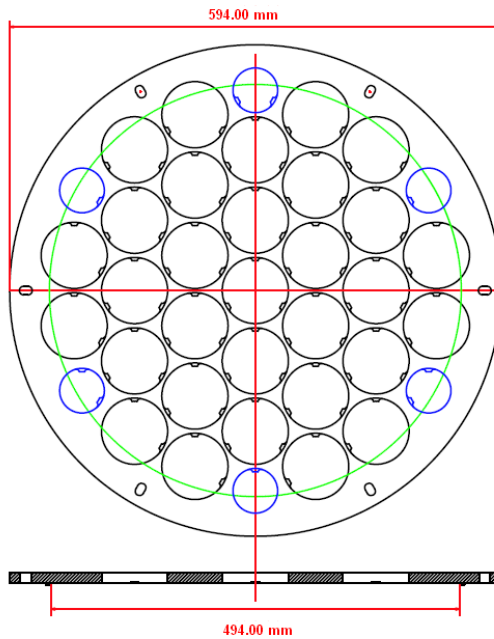


Figure 4.3: Phototubes array’s geometry. The green circle indicates the sensitive area corresponding to the drift width.

volume in a given time window. As stressed before, such double interactions can’t be related to WIMPs. The main request to the active shield is a threshold as low as possible. The active shield is made by more than 5500l of LAr in which a set of 3” photomultipliers can detect the scintillation light once it has been shifted in the same way of the inner detector. The PMTs installed on the internal surface are held by PEEK supports connected to the external support by a thin stainless steel structure, on which a waveshifting/reflecting layer (foils on a thin PEEK frame) will be mounted.

A total of 436 3” phototubes will be installed on the active shield obtaining the same photocathode coverage of the inner volume (10%) with a nominal threshold of 10 keV for argon recoils (10 photoelectrons about). The detection threshold should be lowered respect to the inner volume by the absence of any electric field that could reduce the scintillation. As stressed before, the veto volume is isolated optically and electrostatically from the inner volume using a foil of copper glued on the reflecting film. The active veto has been designed in order to offer a minimal depth of 60 cm to pass from the external to the inner volume. A detailed MonteCarlo simulation (see section 4.7.1) has been developed in order to show the effectiveness of the active veto and to evaluate its performance as a function of the thresh-

Overall External Dimensions (including PMTs and sustaining structure)	<i>Height = 260 cm</i> <i>Diameter = 220 cm</i>
Active LAr Volume	<i>Height = 220cm</i> <i>Diameter = 180 cm</i>
Thickness of <i>VETO</i> layer	<i>60 cm</i>
Internal LAr Mass / Volume	<i>7850 kg/5600 litres</i>
Number of readout 3" PMTs	<i>436</i>
Total photocathode coverage of the inner surface	<i>10%</i>

Table 4.2: Main characteristics of the anti-coincidence system.

old. The simulations show that this thickness is such to reduce by a factor  $10^4$  the probability that a neutron coming from outside can produce a recoil event above threshold in the inner volume without a correspondent signal in the veto region.

## 4.5 PASSIVE SHIELDING

Due to the necessity of minimizing the possible sources of background, the detector has been designed in such way to reduce the possibility that a particle coming from outside can interact inside the sensitive volume. In this way all materials have been selected in order to obtain the minimum radioactive contamination. An additional reduction of background could be obtained using passive shields that can absorb the particles coming from outside and from the contamination of the material of the external cryostat. Between the active shield and the external cryostat a 10 cm thick shield of polyethylene has the function of reducing a possible background induced by neutrons. While the external shielding is dedicated to the environmental neutrons and gammas, this shield is mainly thought to reduce the background coming from the cryostat contamination, whose approximate weight is about 13 ton. According to the results of MonteCarlo simulations (reported in section 4.7.1), the shield will suppress the neutrons by a factor 10, ensuring that the neutron induced background will be taken to the level of less than 1 event / 10 days. The cylinder segmented shape (see fig. 4.4) of the shield is opportunely designed in order to get the necessary spacing to allow the thermal contractions of the polyethylene during the cooling.

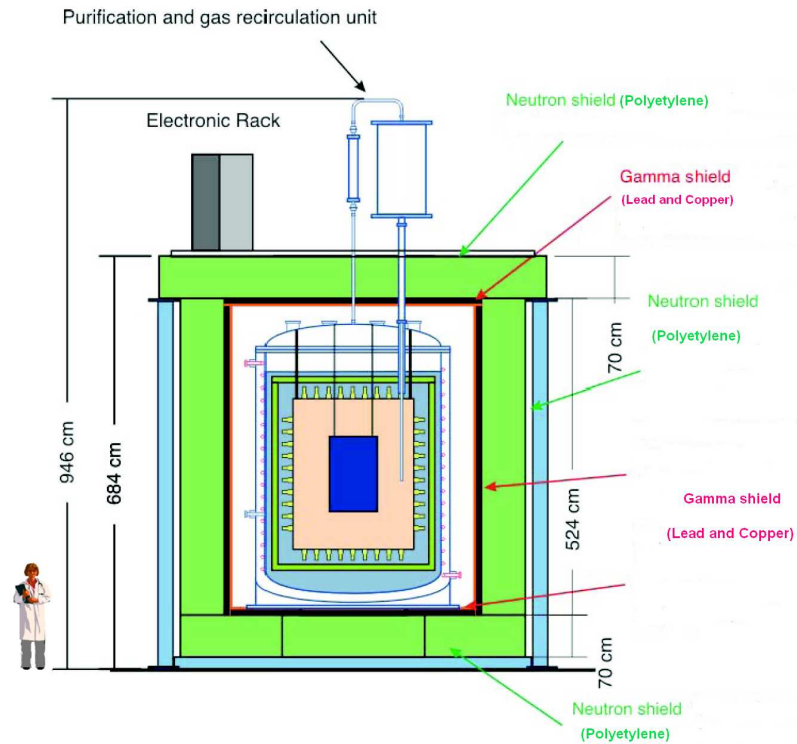


Figure 4.4: Side view of the detector. The external  $\gamma$  and neutron shields are evidenced.

The environmental gamma and neutron background is reduced by a dedicated passive shield enclosing the cryostat, composed by three concentric layers. The outer is a polyethylene layer (thickness 70 cm) for environmental neutrons thermalization, the second is a lead layer (thickness 10 cm) for environmental gammas absorption, and the inner is a copper layer (thickness 2 cm) for the absorption of X-rays eventually produced by the lead shield. Anyway it should be noted that it is not necessary to have the complete absorption of the environmental neutrons. Due to the fact that the maximum recoil energy produced in an elastic scattering by neutrons-nucleus is  $E_{max} \cong 0.1E_n$  where  $E_n$  is the energy of the incoming neutron, it is sufficient to reduce the background neutron spectrum below a kinetic energy of 300 keV to avoid the creation of an Argon recoils above the nominal threshold of 30 keV.

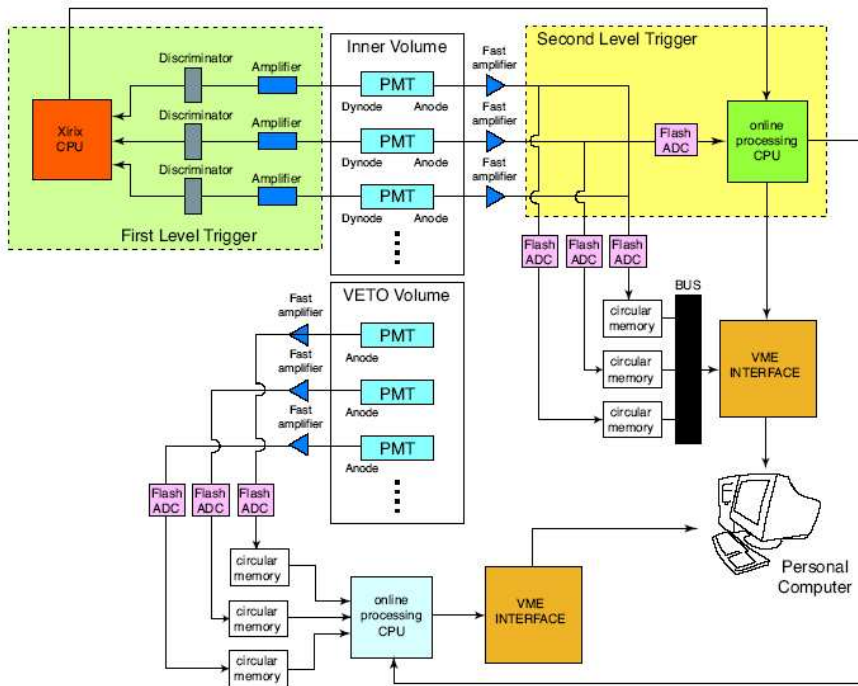


Figure 4.5: Conceptual scheme of the trigger and readout system.

## 4.6 READOUT ELECTRONICS AND TRIGGER SYSTEM

The main features of the DAQ and the trigger system are described in fig. (4.5). Differently from the test chamber, the trigger system has to consider the additional information coming from the veto system, in order to select as possible WIMP candidate, the events producing only in the inner volume a signal over threshold and with the requested ratio between primary and secondary scintillation. The interesting events are characterized by a signal over threshold in at least a number  $n$  of PMTs facing the internal volume and by the requested ratio between primary and secondary scintillation. For those events the information as shape and amplitude of the signal of each PMT of the inner detector, arrival signal times, and signal of the external veto PMTs, will be acquired. While the shape of the signals of the internal PMTs will be entirely recorded, the only interesting information to acquire from the outer PMTs are time and amplitude of the signal, in order to provide (eventually) the anti-coincidence flag. Thus the only signal of the outer PMTs acquired is the anodic signal, while for the internal PMTs both the anodic and ( $12^\circ$ )-dynodic signal are used: the first one is used to record the

event, the second one to be compared to the threshold, in order to select interesting events. The trigger system has been designed using two levels. The dynodic signal is amplified, then a programmable discriminator can provide a logic signal from the comparison between the signal and the selected threshold. The logic signal is sent to a Xirix CPU system to implement the majority logic computing into a definite time window: in case of coincidence of at least  $n$  PMTs over threshold, this system provides a trigger proposal. In order to reject the not interesting  $\gamma$ -background, reducing in this way the total amount of data recorded, a second level trigger is required to accept the trigger proposals characterized by the interesting ratio  $S_2/S_1$  alone. Thus the analogue sum of all the inner photomultipliers is digitalized using flash ADC (a custom board CAEN 789 with the pre-amplified section replaced with a fast amplifier could be used) and then sent to a programmable CPU, to calculate the ratio between the two scintillation peaks in case of first level trigger proposal. Clearly the rejecting criterion must be not so severe in order to discard only the events that can be certainly associated to  $\gamma$ -interaction. A circular memory buffer records the digitalized anodic signals: a width of 16 kB can buffer  $820\mu s$  at  $20Msample/s$ , sufficient to allow the full drift length recording ( $\approx 400\mu s$ ). A CPU controls the readout of the circular memory buffer through a VME interface and its recording onto a mass storage. An off-line more detailed selection, based on both criteria of peak's amplitude ratio and pulse shape analysis, could be performed. To prevent any rejection of nuclear recoils, the veto information is only used to flag all the acquired events. Thus the data sample can be produced by both neutron and WIMP-recoils, but only events with no signal over threshold in the veto system can be considered as interesting WIMP candidate.

## 4.7 BACKGROUND ESTIMATION

### 4.7.1 NEUTRONS INDUCED BACKGROUND

Neutrons coming from the material contamination and from the environmental radioactivity could induce nuclear recoils in the same energy range of the scattering WIMP-nucleus. The active veto has been mainly designed to reduce such background, rejecting those events that have multiple interactions and cannot be associated to a WIMP interaction. A MonteCarlo simulation of the interactions of neutrons inside the 100L detectors has been developed with the aim of studying the efficacy of the active shield in the rejection of multiple events and the effectiveness of a passive polyethylene shielding between the active veto and the dewar in order to decrease the number of neutrons arriving in the LAr volume from outside (due to material contamination and environmental radioactivity). The simulation has been performed using the FLUKA package which allows the simulation of

the interactions and transport of low energy neutrons. The background has been investigated using a preliminary geometry in which the inner sensitive volume is surrounded by the active veto and a containing stainless steel dewar . In addition, slightly different geometries including a layer of polyethylene of different thicknesses between the external dewar and the active veto have been considered (the external dimensions of the dewar are kept constant). The materials properties are defined using the same features of the Fluka package<sup>1</sup>. The basic geometry consists of a LAr cone of 22.5 cm and 23.8 cm radii, 63.0 cm height, below a volume of Argon gas of 33.0 cm radius and 25.6 cm height. A cap of stainless steel (2 mm of thickness) contains the gaseous phase, while a kapton sheet wraps the liquid phase. The central core is surrounded by a veto region of LAr whose dimensions are such that the minimum depth of LAr between inner detector and external dewar is at least 60 cm in each direction. A stainless steel cylinder (2 cm of thickness) contains the veto volume. In order to investigate the effectiveness of a polyethylene layer between the external dewar and the veto Argon, five different geometries with five different thicknesses (2.5, 5.0, 7.5, 10.0, 12.5 cm) of polyethylene have been implemented. In fig (4.6) the geometry layouts as obtained by the FLUKA geometry routines are presented, for the basic geometry (no polyethylene) and for the setup with 12.5 cm of polyethylene. Using these results it is possible to get an estimation of the background (events/day) due to neutrons contribution as the number of neutrons that have interactions in the energy range of interest only inside the inner volume without giving any signal over threshold in the active veto.

### **Fission neutrons from the cryostat**

To investigate the effect of the neutrons originating from the cryostat contamination,  $2 \times 10^6$  neutrons for each configuration have been produced in a random position inside the cryostat walls, and with a random direction. The energy spectrum reproduces a spontaneous fission spectrum (fig 4.7), in order to simulate the neutrons produced by Uranium and Thorium contamination in the cryostat. The particles releasing energy in the internal volume for the standard geometry are mainly neutrons, and photons coming from neutron captures. The fraction of signal events due to photons is 10% in the geometry without polyethylene and it grows up to 40% in the configuration using 5 cm of polyethylene. We are interested in those neutrons producing signals inside the internal volume of LAr, which do not generate a signal over the veto threshold. In fig. (4.8) the energy deposition spectra of the events producing a signal between 20 and 100 keV in the Argon signal region and with no signal above the veto threshold are presented. Four

---

<sup>1</sup>a special FLUKA software package used in the ICARUS event simulations

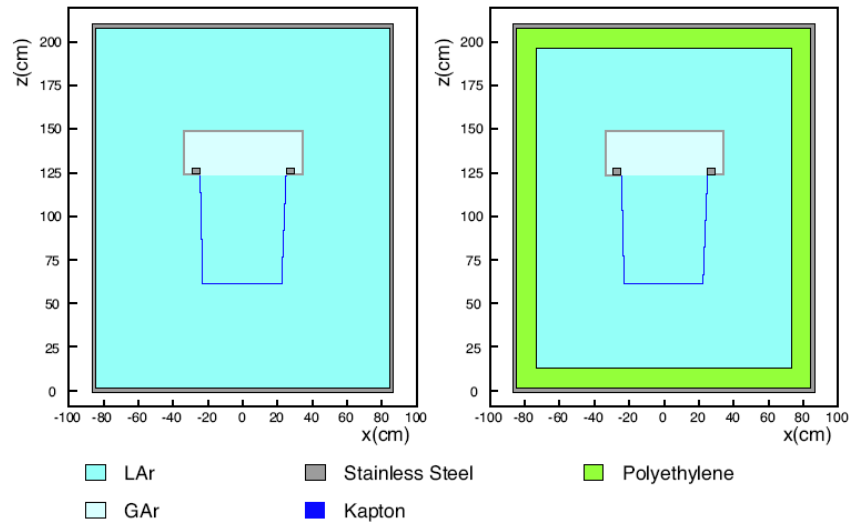


Figure 4.6: On the left the basic geometry implemented in the MonteCarlo is represented. On the right a different geometries, including an additional neutron shield, has been drawn (five different thickness of from 2.5 cm to 12.5 cm have been considered).

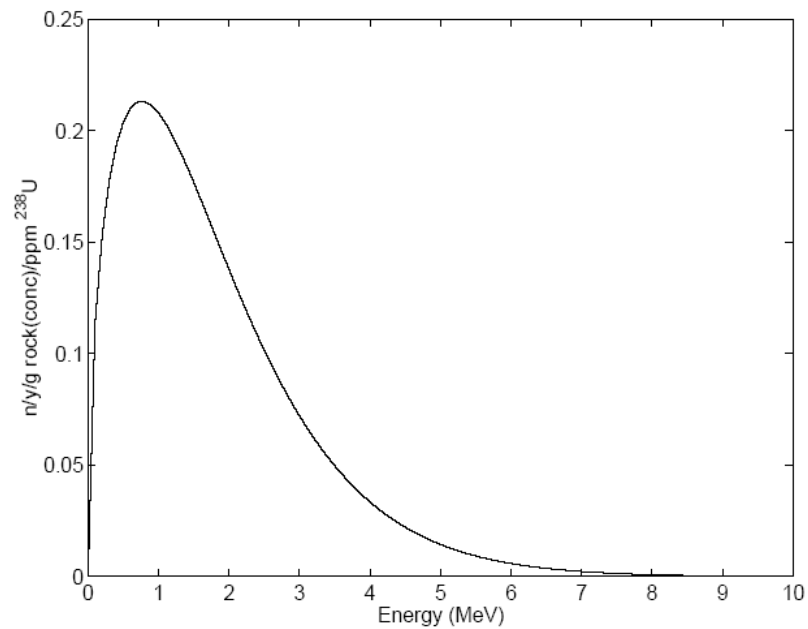


Figure 4.7: Energy spectrum of neutrons from spontaneous fission of  $^{238}\text{U}$ .

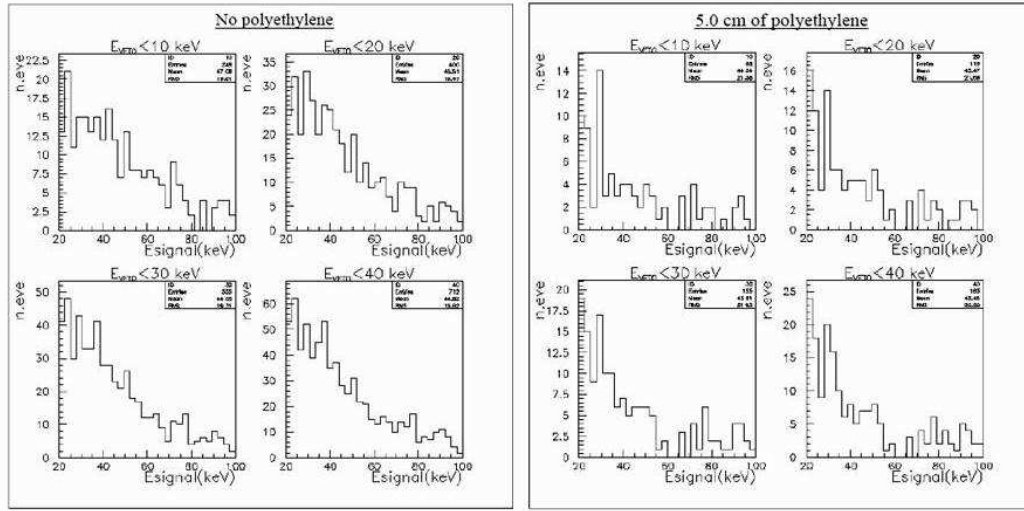


Figure 4.8: Energy deposition in the LAr core in the region 20-100 keV, with four different veto thresholds (10, 20, 30, 40 keV), for the geometry without polyethylene (left) and with 5 cm of polyethylene (right). It is possible to note the decreasing of the number of background events with the lowering of the threshold and with the using of the polyethylene layer .

Thickness of polyethylene (cm)	Energy threshold in the veto region			
	10 keV	20 keV	30 keV	40 keV
0.0	$(1.24 \pm 0.08) \cdot 10^{-4}$	$(2.0 \pm 0.1) \cdot 10^{-4}$	$(2.8 \pm 0.1) \cdot 10^{-4}$	$(3.6 \pm 0.1) \cdot 10^{-4}$
2.5	$(8.2 \pm 0.6) \cdot 10^{-5}$	$(1.30 \pm 0.08) \cdot 10^{-4}$	$(1.70 \pm 0.09) \cdot 10^{-4}$	$(2.2 \pm 0.1) \cdot 10^{-4}$
5.0	$(4.4 \pm 0.5) \cdot 10^{-5}$	$(5.8 \pm 0.5) \cdot 10^{-5}$	$(7.7 \pm 0.6) \cdot 10^{-5}$	$(9.1 \pm 0.7) \cdot 10^{-5}$
7.5	$(1.4 \pm 0.3) \cdot 10^{-5}$	$(2.3 \pm 0.3) \cdot 10^{-5}$	$(3.3 \pm 0.4) \cdot 10^{-5}$	$(4.3 \pm 0.5) \cdot 10^{-5}$
10.0	$(9.5 \pm 0.3) \cdot 10^{-6}$	$(1.4 \pm 0.3) \cdot 10^{-5}$	$(2.1 \pm 0.3) \cdot 10^{-5}$	$(2.6 \pm 0.4) \cdot 10^{-5}$
12.5	$(8.0 \pm 0.2) \cdot 10^{-6}$	$(1.0 \pm 0.2) \cdot 10^{-5}$	$(1.2 \pm 0.2) \cdot 10^{-5}$	$(1.4 \pm 0.3) \cdot 10^{-5}$

Table 4.3: Number of events per emitted (fission) neutron from the cryostat with an energy deposition between 20-100 keV in the active volume and below the threshold in the veto region.

different thresholds (10, 20, 30, 40 keV) have been considered. As we can see from fig. (4.8) the number of background events decreases with the veto threshold. Energy releases in the inner LAr volume are considered resolved as one hit if separated by less than 2 cm in the xy plane and 0.5 cm in the z (drift) axis. From the simulations it can be seen that the hit spatial distribution is uniform in the whole inner volume and that a large number of neutrons can have multiple interactions in the LAr core itself: the 52%

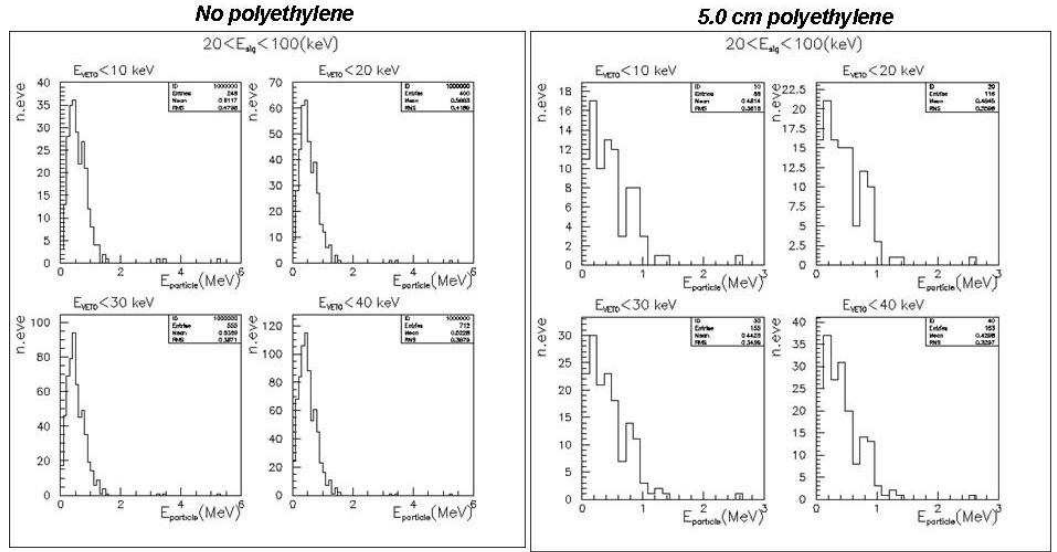


Figure 4.9: Energy spectrum of the particles producing signals in the interesting range (20-100 keV) and with an energy deposition in the veto volume below threshold for the geometry without polyethylene and with 5 cm of polyethylene.

of the incoming particles undergo more than one interaction in the central core taking in account the previous segmentation. In table (4.3) the fraction of particle surviving to cuts of the energy released in the core and in the veto is reported, for each of the six configurations. The number of simulated neutrons is  $2 \times 10^6$  for each configuration, and, depending from the configuration, there are  $1/10^4 \div 1/10^5$  event per emitted neutron producing signals in the interest energy range with an energy deposition below threshold in the veto region.

The types of the particles producing the background events and their energy distributions have been also investigated. From the simulation it can be seen that particles producing a signal in the range 20-100 keV in active volume, with a released energy below threshold in the veto volume are always neutrons. In fig (4.9) the results are reported for the basic configuration and for the one with 5 cm of polyethylene. As we can see in both cases the interesting signals are produced by neutrons with a broad spectrum centred roughly around 0.5 MeV. The simulation shows that there is a  $1/10^4 \div 1/10^5$  probability (depending on threshold and polyethylene thickness) for a neutron of releasing an amount of energy in the range of interest (20-100 keV) with an energy deposition in the veto region below the threshold. Independently from the threshold, a the reduction of about one order of

magnitude of this probability is obtained using a shielding of polyethylene with a thickness of 10 cm respect to the case without shielding.

### Neutrons coming from the LNGS underground hall

Another simulation has been done to understand the background due to neutrons coming from the LNGS hall. In this case neutrons are simulated in such a way to have an uniform and isotropic fluence inside a sphere of 2.0 m of radius surrounding the detector with a flat energy spectrum in six different energy bins: 0-0.5 MeV, 0.5-1 MeV, 1-2 MeV, 2-4 MeV, 4-8 MeV and 8-16 MeV. For this simulation the standard geometry has been used, and  $2 \times 10^6$  neutrons have been produced for each energy bin for the standard geometry without polyethylene, and  $1 \times 10^6$  for in the geometries with 5 cm and 10 cm polyethylene layers. The spectrum of the energy released in the active volume has been investigated for the particles which have an energy deposition below threshold in the veto volume. As in the previous case, the same four different thresholds have been used. The expected background events (*event cm<sup>2</sup>*) for a unit incident flux with an energy deposition between 20-100 keV in the active volume and below the threshold in the veto region is reported in the tables (4.4) for the different energy bins. The simulation shows that the expected number of background events for an unit incident flux of neutrons with energy up to 16 MeV falls in the range 1100 (*event cm<sup>2</sup>*) for the standard geometry. It must be noticed that in the cases of the geometries with 5 cm and 10 cm of polyethylene layers the number of background events is reduced respectively of one and two order of magnitude in the range  $(0 \div 1.0)MeV$ , so a polyethylene shield is very effective.

In fig. (4.10) the scatter plot of the energy of the incoming particles (y axis) versus the total energy released in the LAr sensible volume (x axis) has been represented in the cases of one or more interactions<sup>2</sup>. As we can see there is a clear relation at  $E_{signal} > 50keV$  between the energy released and the energy of the incoming particles, only in the case of one interaction. This correlation is produced by the cinematical limit on the maximum recoil energy produced in an elastic scattering by neutrons-LAr nucleus ( $E_{max} \cong 0.1E_n$ , where  $E_n$  is the energy of the incoming neutron). Few events that have larger energy releasing have been investigated. Those events are characterized by two different interaction, so close to be identified as a single scattering according to the implemented spatial resolution.

---

<sup>2</sup>the neutron energy bin considered is 0.5-1 MeV

<i>No shield</i>				
<i>Energy bin (MeV)</i>	<i>Energy threshold in the veto region</i>			
	<i>10 keV</i>	<i>20 keV</i>	<i>30 keV</i>	<i>40 keV</i>
<i>0-0.5</i>	<b><i>31.7±1.4</i></b>	<b><i>51.0±1.8</i></b>	<b><i>73.3±2</i></b>	<b><i>95.3±2</i></b>
<i>0.5-1.0</i>	<b><i>34.1±1.5</i></b>	<b><i>48.8±1.8</i></b>	<b><i>61.4±2</i></b>	<b><i>75.3±2</i></b>
<i>1.0-2.0</i>	<b><i>3.2±0.5</i></b>	<b><i>4.7±0.5</i></b>	<b><i>7.0±0.7</i></b>	<b><i>9.6±0.8</i></b>
<i>2.0-4.0</i>	<b><i>0.7±0.2</i></b>	<b><i>1.2±0.3</i></b>	<b><i>1.8±0.3</i></b>	<b><i>2.2±0.4</i></b>
<i>4.0-8.0</i>	<b><i>1.0±0.2</i></b>	<b><i>1.4±0.3</i></b>	<b><i>2.0±0.3</i></b>	<b><i>2.3±0.4</i></b>
<i>8.0-16.0</i>	<b><i>0.9±0.2</i></b>	<b><i>1.3±0.3</i></b>	<b><i>1.6±0.3</i></b>	<b><i>1.7±0.3</i></b>

<i>5 cm thick shield</i>				
<i>Energy bin (MeV)</i>	<i>Energy threshold in the veto region</i>			
	<i>10 keV</i>	<i>20 keV</i>	<i>30 keV</i>	<i>40 keV</i>
<i>0-0.5</i>	<b><i>1.3±0.4</i></b>	<b><i>2.2±0.5</i></b>	<b><i>2.9±0.6</i></b>	<b><i>3.3±0.6</i></b>
<i>0.5-1.0</i>	<b><i>3.9±0.7</i></b>	<b><i>7.0±0.9</i></b>	<b><i>8.2±1.0</i></b>	<b><i>9.6±1.1</i></b>
<i>1.0-2.0</i>	<b><i>3.2±0.6</i></b>	<b><i>4.9±0.8</i></b>	<b><i>6.5±0.9</i></b>	<b><i>8.1±1.0</i></b>
<i>2.0-4.0</i>	<b><i>2.2±0.5</i></b>	<b><i>3.7±0.7</i></b>	<b><i>4.7±0.8</i></b>	<b><i>5.8±0.9</i></b>
<i>4.0-8.0</i>	<b><i>1.1±0.4</i></b>	<b><i>1.6±0.5</i></b>	<b><i>3.0±0.6</i></b>	<b><i>3.8±0.7</i></b>
<i>8.0-16.0</i>	<b><i>1.9±0.5</i></b>	<b><i>2.4±0.5</i></b>	<b><i>2.5±0.6</i></b>	<b><i>3.2±0.6</i></b>

<i>10 cm thick shield</i>				
<i>Energy bin (MeV)</i>	<i>Energy threshold in the veto region</i>			
	<i>10 keV</i>	<i>20 keV</i>	<i>30 keV</i>	<i>40 keV</i>
<i>0-0.5</i>	<b><i>&lt;0.1</i></b>	<b><i>&lt;0.1</i></b>	<b><i>&lt;0.1</i></b>	<b><i>&lt;0.1</i></b>
<i>0.5-1.0</i>	<b><i>0.5±0.2</i></b>	<b><i>0.6±0.3</i></b>	<b><i>0.6±0.3</i></b>	<b><i>0.8±0.3</i></b>
<i>1.0-2.0</i>	<b><i>1.5±0.4</i></b>	<b><i>1.8±0.5</i></b>	<b><i>2.2±0.5</i></b>	<b><i>2.4±0.6</i></b>
<i>2.0-4.0</i>	<b><i>1.9±0.5</i></b>	<b><i>2.5±0.6</i></b>	<b><i>3.5±0.7</i></b>	<b><i>4.0±0.7</i></b>
<i>4.0-8.0</i>	<b><i>1.6±0.5</i></b>	<b><i>2.3±0.5</i></b>	<b><i>2.6±0.6</i></b>	<b><i>3.3±0.6</i></b>
<i>8.0-16.0</i>	<b><i>0.9±0.3</i></b>	<b><i>0.9±0.3</i></b>	<b><i>1.4±0.3</i></b>	<b><i>1.9±0.5</i></b>

Table 4.4: Expected background events ( $evt\ cm^2$ ) for a unit incident flux with an energy deposition between 20-100 keV in the active volume and below the threshold in the veto region, for the different energy ranges and geometries (no shield, 5.0 cm and 10.0 cm of shielding).

### Fission neutrons from the internal material contamination

The last neutron simulation dealt with neutrons coming from the contamination of the inner materials. The internal geometry has been divided in two parts: the stainless steel cathode and the stainless steel cap. Each part has been considered as a neutron source, with random direction and energy spectrum reproducing a (uncorrelated) spontaneous fission spectrum as in the case of the neutrons coming from the external dewar. A total of ( $2 \times 10^5$ ) neutrons from the cathode and ( $3.31 \times 10^5$ ) from the cap have been simulated using the standard geometry. It should be noticed that, due the lower mass of the internal components, a little number of neutrons is

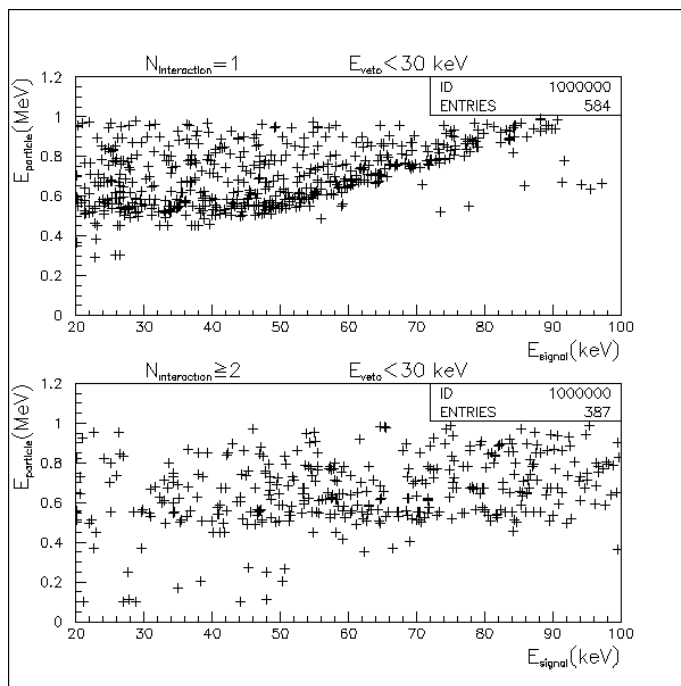


Figure 4.10: Scatter plot of the energy of the incoming particles (y axis) versus the total energy released in the LAr sensible volume (x axis) in the cases of one (top) or more (down) interactions (neutron energy range  $0.5 \div 1\text{MeV}$ ). The effect of the maximum allowed energy that is possible to release in a single elastic scattering is clear on the first plot.

Source	Energy threshold in the veto region			
	10keV	20 keV	30 keV	40 keV
Cathode	$(1.17 \pm 0.02) \cdot 10^{-2}$	$(1.49 \pm 0.02) \cdot 10^{-2}$	$(1.90 \pm 0.03) \cdot 10^{-2}$	$(2.09 \pm 0.03) \cdot 10^{-2}$
Cap	$(3.0 \pm 0.1) \cdot 10^{-3}$	$(3.6 \pm 0.1) \cdot 10^{-3}$	$(4.5 \pm 0.1) \cdot 10^{-3}$	$(5.2 \pm 0.1) \cdot 10^{-3}$

Table 4.5: Background events expected per emitted (fission) neutron coming from the contamination of some internal materials.

expected to come from the internal materials respect to the neutrons from the dewar contamination. Anyway, due to the short distance between the active volume and the source, there is a much higher probability for such type of neutrons to produce a background event than in the previous cases. In table (4.5) the number of background events, per emitted is fission neutron is reported. The simulation shows that the events per emitted neutron producing background signals is of the order of  $1 \times 10^{-2} \div 2 \times 10^{-2}$  for the neutrons coming from the cathode and  $3 \times 10^{-3} \div 5 \times 10^{-3}$  for the neutrons

coming from the cap.

### Estimation of neutron induced background

It is possible to use the previous results to compute an estimation of the numbers of events/day of background due to neutrons coming from different sources. Given the better radiopurity of low background lead and copper with respect to stainless steel (several order of magnitude), the main contribution to neutron background comes from the external stainless steel vessel. Assuming a global stainless steel mass of 13 ton, a conservative value for the Uranium contamination of the order of  $0.5Bq/kg$  and a  $^{238}U$  spontaneous fission branching ratio of  $5.45 \times 10^7$ , the expected background rate associated with spontaneous fission neutrons from the vessel is of the order of 1 event each  $1.3 \times 10^2$  days (adopting 10 cm of thickness of polyethylene and 30keV of veto threshold and assuming two neutrons generated on average in each fission). In the same way it is possible to estimate the background due to neutrons from the internal materials contamination (stainless steel cathode and cap). Assuming a mass of 6.3 kg and 9.6 kg respectively for cathode and cap and using the previous values about contamination and branching ratio together with the calculated MonteCarlo probability for a neutron to produce a background event, it is possible to estimate a rate lower than 1 event each  $10^4$  days. It is possible to get a rough estimation of the background due to environmental neutrons assuming that the expected number of background events for an unit incident flux of neutrons with energy up to 16 MeV falls in the range  $0.1 \div 4 \text{ evt cm}^2$  for the configuration with 10 cm of polyethylene. Taking the average number of the expected background events for a unit incident flux ( $\text{event cm}^2$ ) between  $0 \div 4MeV$  with a veto threshold of 30 keV ( $1.6 \text{ evt cm}^2$ ) and a total fluence of  $5 \times 10^{-7} \text{ neutrons} \cdot \text{cm}^{-2} \cdot \text{s}^{-1}$ , a value of one background event each  $10^2$  days is obtained. It must be stressed that those values must be considered as conservative upper limits. For example, using the segmentation stressed before (resolving 2 cm in xy plane and 0.5 dm along the drift direction), only less than one half of the interaction in the sensitive volume are just single interactions. We recall here that multiple interactions can be individuated and rejected, thus reducing of the potential background. Moreover, the background induced by environmental neutrons, that according to MonteCarlo simulation should be the main neutron background source, could be easily reduced at a lower level using an external hydrogenated material layer; this is due the fact that in principle a layer much larger than 10 cm can be arranged outside the dewar. To this purpose a layer of 70 cm of thickness has been designed as described in the general setup of the 100l detector.

## 4.7.2 $\beta - \gamma$ INDUCED BACKGROUND

The effect of the photons originating from the contamination of the materials of the PMTs have been studied using the same MonteCarlo package (FLUKA) and the same geometry defined above. The photons are produced in a random position in the internal volume, 7 cm above the interface between gas and liquid Argon, to simulate the photons coming from the photomultipliers. Seven different energies have been considered (50, 100, 250, 500, 1000, 1500, 2000 keV), and  $1 \cdot 10^5$  photons for each energy have been produced with a random direction. Both the spatial distribution of the hits and the energy deposition spectra inside the sensitive volume has been studied for each energy. The experimental measurements on the scintillation yield in LAr show that the slow recoils produce an amount of scintillation light with a photon yield which is  $f_N$  times smaller than the one of an electron or a gamma of the same recoil energy. A factor  $f_N = 0.3$  has been measured. For this reason an energy range of interest of  $0 \div 30$  keV and four veto thresholds of 3.0, 6.0, 9.0, 12.0 keV have been considered to have a direct comparison with the neutron analysis. The spatial distribution of the hits in the sensitive volume for the photons of all the energies has been investigated (fig 4.11), together their energy deposition in the LAr inner volume with four different veto thresholds. As it is expected the energy deposition in the energy range of interest is strictly dependent from the energy of the primary photon: for example in the case of 500 keV photons only 12 events (out of  $10^5$  produced) have an energy deposition in the energy range of interest. In table (4.6) the number of events per emitted photon with an energy deposition between 0-30 keV in the active volume and below the threshold in the veto region is reported. The simulation shows that there is a  $2 \times 10^{-5} \div 3 \times 10^{-2}$  probability (depending mainly on the photons energy) for a photons of releasing an amount of energy in the range of interest (0-30 keV) with an energy deposition in the veto region below the threshold. The maximum probability in the production of a background event is for a 100 keV photon. For these events the barycentre of the energy depositions has on average a distance from the liquid-gas interface of less than 1 cm (fig 4.11). In this way such type of events should be efficiently rejected by a geometrical cut based on the three-dimensional localization of the interactions using, as stressed before, the drift time information (z-axis) and the pattern of the PMTs signals (x-y plane). Thus the definition of a fiducial volume can efficiently reject this type of background events that are mainly localized close the liquid-gas interface. Moreover these considerations can be used in the estimation of the background produced by  $\beta$  and  $\gamma$  and events. The general background produced outside the sensitive volume can strongly be attenuated by the shielding and should constitute a negligible background, leaving as un-avoidable source of possible background the  $\gamma$  and  $\beta$  particles coming

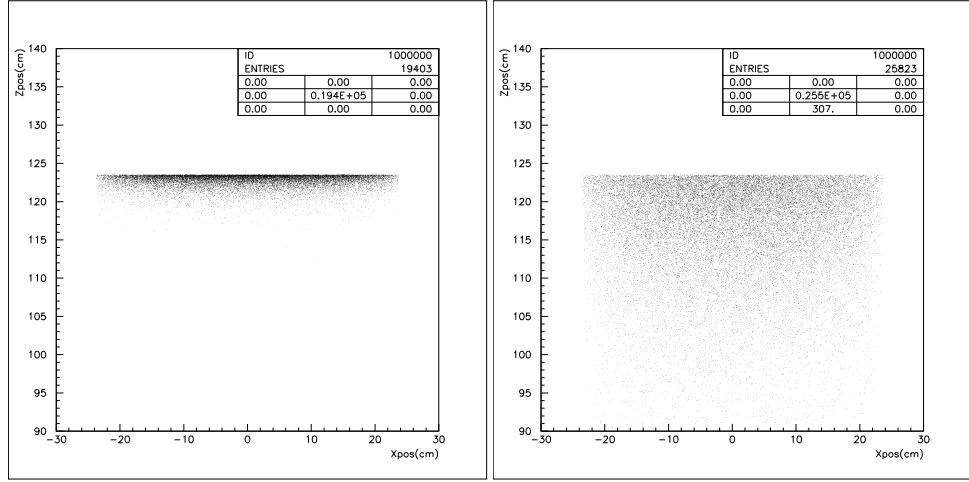


Figure 4.11: Spatial distribution of the events in the inner LAr volume obtained by simulating  $\gamma$ -ray emission from the phototubes for  $50\text{keV}$  photons (left) and  $500\text{keV}$  photons. From the plots it is clear the interface liquid-gas level. (right)

Energy (keV)	Energy threshold in the veto region			
	3 keV	6 keV	9 keV	12 keV
50	$(7.7 \pm 0.2) \cdot 10^{-3}$	$(7.7 \pm 0.2) \cdot 10^{-3}$	$(7.7 \pm 0.2) \cdot 10^{-3}$	$(7.7 \pm 0.2) \cdot 10^{-3}$
100	$(2.74 \pm 0.05) \cdot 10^{-2}$	$(2.75 \pm 0.05) \cdot 10^{-2}$	$(2.76 \pm 0.05) \cdot 10^{-2}$	$(2.77 \pm 0.05) \cdot 10^{-2}$
250	$(1.60 \pm 0.13) \cdot 10^{-3}$	$(1.61 \pm 0.13) \cdot 10^{-3}$	$(1.63 \pm 0.13) \cdot 10^{-3}$	$(1.64 \pm 0.13) \cdot 10^{-3}$
500	$(1.2 \pm 0.3) \cdot 10^{-4}$	$(1.2 \pm 0.3) \cdot 10^{-4}$	$(1.2 \pm 0.3) \cdot 10^{-4}$	$(1.2 \pm 0.3) \cdot 10^{-4}$
1000	$(7 \pm 3) \cdot 10^{-5}$	$(7 \pm 3) \cdot 10^{-5}$	$(7 \pm 3) \cdot 10^{-5}$	$(7 \pm 3) \cdot 10^{-5}$
1500	$(2.0 \pm 1.4) \cdot 10^{-5}$	$(2.0 \pm 1.4) \cdot 10^{-5}$	$(2.0 \pm 1.4) \cdot 10^{-5}$	$(2.0 \pm 1.4) \cdot 10^{-5}$
2000	$(5 \pm 2) \cdot 10^{-5}$	$(6 \pm 2) \cdot 10^{-5}$	$(6 \pm 2) \cdot 10^{-5}$	$(6 \pm 2) \cdot 10^{-5}$

Table 4.6: Number of events per emitted photon with an energy deposition between 0-30 keV in the active volume and below the threshold in the veto region

from the impurity dissolved in LAr, mainly  $\gamma$ -emission of  $^{222}\text{Rn}$  decay chain and  $\beta$ -emission of  $^{39}\text{Ar}$ . All the other possible sources considered ( $^{41}\text{Ar}$ ,  $^{42}\text{Ar}$ ,  $^{42}\text{K}$ , and  $^{85}\text{Kr}$ ) can produce a background level well below the level of 1 event each 100 days. Regarding the contamination by given Radon, as stressed before, its contribution can be neglected since  $^{222}\text{Rn}$  has a half-life of about 4 days. The main contribution to the background should come from the  $^{39}\text{Ar}$ , that has a half-life of the order of 269 years and cannot be neglected. According to the spectrum of its  $\beta$ -decay the fraction of events in the energy range of interest is of the order of about 5.0%. This result, together with the measured activity in the 2.3l prototype of  $1.1\text{Bq/l}$  leads to a

number of interaction in 100 days equal to  $4.7 \times 10^7$ . Assuming this result it would be necessary to obtain a rejection power better than  $2.1 \times 10^8$  in order to reduce the background to a negligible level of 1 event each 100 days. This level should be achievable by using the combined selections over the pulse shape and the ratio  $S_2/S_1$  as preliminary tests on the 2.3l chamber have shown. Although, an enhanced discrimination power should be expected in the 100l due to the improvements in the set-up, another possible way to reduce the  $\gamma - \beta$  background should come from the isotopic separation of the commercial Argon. A depletion of  $^{39}\text{Ar}$  by a factor  $10^2 - 10^3$  seems to be achievable, allowing, in this way, to get the requested background rate of 1 event each 100 days.

### 4.7.3 OTHER BACKGROUND SOURCES

Cosmic rays and neutrinos can produce interactions in the detector, and in principle those events must be investigated as additional sources of background. The only way for a cosmic ray to produce a background events is through the production of an unstable nuclides followed by a delayed neutron emission. Anyway, the typical contemporary emission of other particles, ( $X$ -ray or  $\alpha$  particle) by the nucleus itself, allows the rejection of such events. Moreover the rate of cosmic rays inside the underground laboratory is very low (about  $1 \text{ m}^{-2}\text{h}^{-1}$ ) should make negligible this background. Neutrinos could represent a possible source of background through the elastic scattering neutrino-nucleus

$$\nu + (A, Z)_{rest} \rightarrow \nu + (A, Z)_{recoil}$$

where  $(A, Z)$  represent the target nucleus  $A$  of mass  $M_T$  with  $N$  number of neutrons and  $Z$  atomic number. The scattering should occur for process with a small momentum transfer ( $\Delta p \cdot R_a \leq 1$  where  $\Delta p$  is the 3-momentum transfer and  $R_a$  is the spatial extension of the target nucleus). In this case, neglecting the effect associated to the nuclear form factor, the differential cross section (for all the neutrino species) can be written as<sup>3</sup>

$$\frac{d\sigma}{d\cos\theta} = \frac{G^2}{8\pi} [Z(4\sin^2\theta_w - 1) + N]^2 E_\nu^2 (1 + \cos\theta) \quad (4.1)$$

where  $\theta$  is the scattering angle,  $G^2$  the Fermi constant, and  $E_\nu$  the neutrino energy<sup>4</sup>. As  $\sin^2\theta_w \approx 0.22$  ( $\approx 1/4$ ) the contribution due to  $Z$  protons is almost cancelled and the cross section is essentially proportional to  $N^2$ .

<sup>3</sup>Only the vector current component has been considered (an axial-vector current, leading to small incoherent contribution for nuclei with spin, is neglected) .

<sup>4</sup>This coherent cross section depends on the square of the weak charge  $Q_w = N - (1 - 4\sin^2\theta_w)Z$

The integration of eq. (4.1) leads to the total cross-section

$$\frac{d\sigma}{dq^2} = \frac{G^2}{8\pi} N^2 \left[ 1 - \frac{q^2}{q_{max}^2} \right] \quad (4.2)$$

where  $\vec{q}$  is the three momentum transferred to the nucleus ( $q^2 = 2E_\nu^2(1 - \cos\theta)$ ). Thus the total cross section is

$$\sigma = \frac{G^2}{16\pi} N^2 q_{max}^2 = \frac{G^2 N^2}{4\pi} E_\nu^2 \quad (4.3)$$

In such scheme the integrated cross section can be evaluated as

$$\sigma_{tot} \approx 0.42 \cdot [10^{-44} N^2 (\frac{E_\nu}{MeV})^2] cm^2 \quad .$$

The energy transfer to the recoiling nucleus is small as its average value is

$$\overline{E_r} = \frac{2}{3A} \left( \frac{E_\nu}{MeV} \right)^2 keV \quad (4.4)$$

Hence the recoil energies could be easily evaluated. Such type of events can be produced at the same time by solar and atmospheric neutrinos. The cross section (4.2) and the solar neutrino spectrum have been implemented in a MonteCarlo simulation based on FLUKA, giving a predicted rate of *3.5 events/ton/day* for pp neutrinos, *0.23 events/ton/day* for  $^8B$  neutrinos and *0.0063 events/ton/day* for pep and hep neutrinos. The predicted recoil spectrum (fig 4.12) rapidly falls with the increasing of  $E_r$ . Although only  $^8B$  and hep neutrinos can give a signal in the range of ten keV, the minimum threshold in the recoil energy can reject those events. As we can see from the eq. (4.4) the recoil energy increases as  $E_\nu^2$ . thus atmospheric neutrinos, having higher energies (up to hundreds of MeV), can produce scattering events in our energy range of interest. The eq. (4.2) predicts a flat recoil spectrum

$$\frac{d\sigma}{dE_r} = 0.42 \times 10^{-44} N^2 A (cm^2 keV^{-1}) \quad (4.5)$$

which evaluated for Argon gives

$$\frac{d\sigma}{dE_r} = 0.81 \times 10^{-40} keV^{-1} \quad .$$

Taking into account the total atmospheric neutrinos flux, estimated as

$$\Phi \approx 11.5 cm^{-2} s^{-1}$$

the total number of recoil events can be evaluated as function of the lower energy threshold, through

$$n_r(E^{th}) = \int_{E^{th}}^{80keV} E_R \frac{d\sigma}{dE_R F^2} F^2(2M_{Ar} E_R) \Phi \rho_{Ar} dE_R \quad (4.6)$$

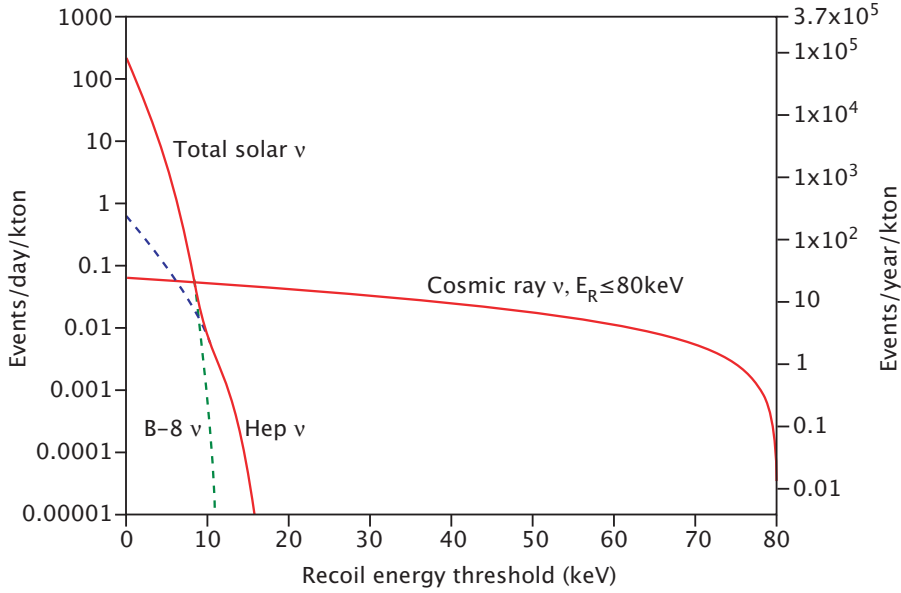


Figure 4.12: Irreducible background rates due to neutrinos as function of the detection threshold. In order to evaluate the background in the interest energy range, an upper limit in detection  $E_r < 80\text{keV}$  has been introduced in the case of cosmic neutrinos.

where  $\rho_{Ar}$  is the numeric density of Ar (number of atoms per unit of mass) and  $F^2(q^2)$  is the nuclear form factor (to be considered at higher momentum transfer). The computation of the number of events as function of the recoil energy threshold is shown in fig (4.12). Assuming a mass of 140 kg of Argon, and a lower threshold of  $30\text{keV}$ , the number of estimated background events is of the order of few  $10^{-6}\text{events/day}$ . Although the neutrino-nucleus elastic scattering could produce, in principle, a nuclear recoil into the energy range of interest, neutrinos (both atmospheric and solar) should not be considered as a significant source of background. Only a considerable reduction of the detection energy threshold would require more accurate estimations.

## 4.8 EXPECTED EXPERIMENTAL SENSITIVITY

As it has been shown in the last sections, the dominant background should be caused by the  $^{39}\text{Ar}$  contamination. The expected rate, according to the 2.3l results, should be estimate as  $0.1 \div 0.01 \text{ events } d^{-1}$ . In principle, as shown in section (2.3), the knowledge of the background spectrum could be used to apply a background subtraction, in order to compare the observed energy spectrum with the expected one. Anyway, neglecting any background

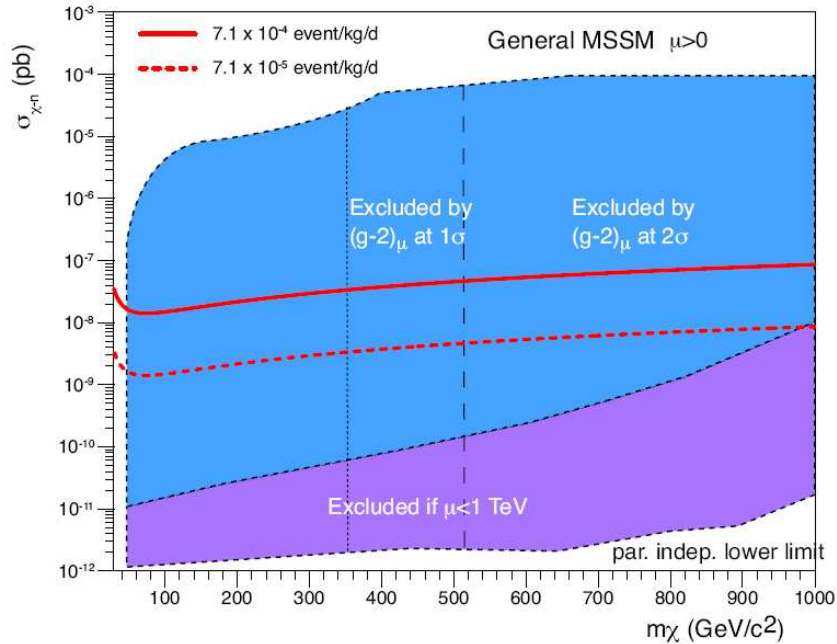


Figure 4.13: Iso-rate curves representing the number of detected events expressed in  $iru(event\ kg^{-1}\ day^{-1})$  in the  $\sigma_{\chi-n} - m_{\chi}$  space of parameters. The allowed parameter region is also shown. Reported curves, obtained according the equations of sec. (2.3), correspond to  $7.1 \times 10^{-4} events\ kg\ d^{-1}$  (continuous line) and  $7.1 \times 10^{-5} events\ kg\ d^{-1}$  (dashed line).

subtraction, it is possible to estimate the projected sensitivity for the 100l detector, requiring a WIMPs recoil rate grater than the maximum background event rate.

The maximum projected sensitivity with 100l of sensitive volume ( $M = 140kg$ ) is  $7.1 \times 10^{-4} events\ kg\ d^{-1}$  for  $0.1 events\ d^{-1}$  of background, and  $7.1 \times 10^{-5} events\ kg\ d^{-1}$  assuming  $0.01 events\ d^{-1}$  of background. Recalling iso-rates curves (fig. (3.1)), this means that it is possible to explore the WIMP-nucleon cross section at a level of  $10^{-8} \div 10^{-9} pb$  (fig. 4.13). These results give not only the possibility of a significant enhancement of actual experimental limits, but allow the aim to test the more favored SUSY models.

## Chapter 5

# Characterization of photomultiplier tubes for the WARP experiment

### 5.1 INTRODUCTION

The WARP detector will be equipped with photomultiplier tubes (PMT) for the detection of the scintillation light produced in liquid Argon by nuclear recoils and ionizing particles. As stressed in the previous chapter, the inner detector contains 37 PMTs (6 of 2" and 31 of 3") placed in the gas pocket on the top of the central detecting region. The active veto system is seen by 430 3" PMTs immersed in the liquid. Electron Tubes Ltd., London, has developed special cryogenic PMTs for this application. We have tested the first prototypes of the ETL D749QFLAPt tube, which has a 2" flat quartz window, two types of 3" PMTs, the ETL D750QFLAPt (quartz window) and ETL D750UFLAPt (low activity glass window), and finally the 2" ETL D757FLAPt recently produced. The first sets of photomultipliers specifically manufactured for the WARP detector by the Electron Tubes have been tested in Naples. Our measurements were focused to characterize the operating performances of the PMTs at room and cryogenic temperature. In order to minimize the costs of the test activity, all cryogenic measurements were carried out in liquid nitrogen, which temperature (77K) is close to that of the liquid argon (87K). We intended to measure the dark count rate and spectrum, the single electron response (SER), and the gain and linearity of response. In addition a light source has been used to measure the linearity of the response, with two orders of magnitude in lightening, corresponding to few photoelectrons and many tens of photoelectrons. All the measurements have been performed both at room and cryogenic temperature. In this chapter, after a brief introduction regarding the functioning of

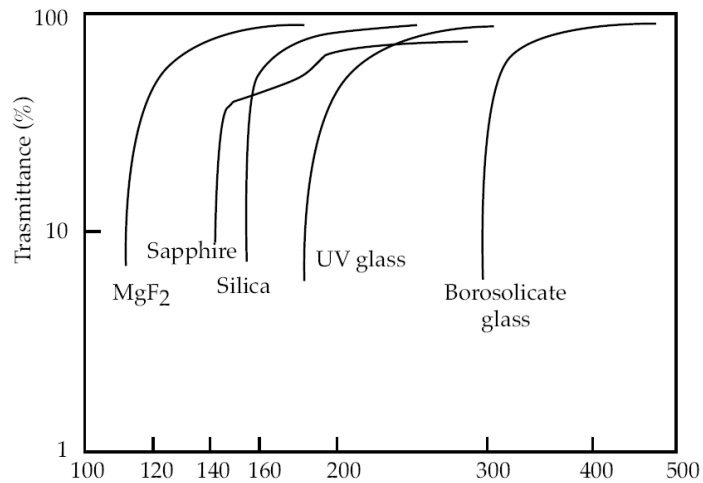


Figure 5.1: Transmittance of different materials, typically used as PMTs windows, as function of the incident light wavelength (data referred at  $1mm$  thick window.)

EMI's PMTs at cryogenic temperature, the set-up of the test facility made in Naples will be described together with the test performed. Finally the results and the conclusions about the preliminary test will be reported.

## 5.2 CRYOGENIC PHOTOMULTIPLERS

The ETL model 749 and 750 are a 12 stage linear focussed dynode photomultipliers with a flat window of glass or quartz. In fig (5.1) the windows transmittance as function of the incident light wavelength is shown. As we can see a shifting of the light to a longer wavelength is required in order to detect the liquid Argon scintillation light (peaked at  $128nm$ ) with the use of glass or quartz windows. Although an MgF<sub>2</sub> window would be able to get a transmittance value sensitively different from zero at the wavelength of the pure liquid Argon luminescence light, it has been preferred to not use such material due to its fragility at cryogenic temperature. Two ways to shift the wavelength of the Argon scintillation light have been investigated. The first one is based on a Xenon doping, whose effect becomes visible for Xenon mass concentration larger than  $10ppm$ . The mechanism of the shifting has been well studied in literature and is explained through the quick capture of the Argon scintillation light by a Xenon atom, whose dis-excitation can produce the emission of a photon with  $175nm$  of wavelength<sup>1</sup>. At this wavelength

<sup>1</sup>The processes are:

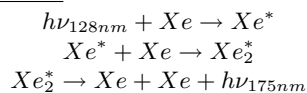
quartz windows have transmittance values different from zero (fig. 5.1). As stressed before, the solution adopted by the collaboration is to use of the Tetrphenylbutadiene (TPB), which absorbs the  $128nm$  light and reemits it in the visible range (blue light peaked at  $438nm$ ), allowing the use of glass windows (fig. 5.1). A layer of  $200\mu gcm^{-2}$  of TPB has been proved to optimize the conversion efficiency and to reduce the effect of auto-absorption.

The major problem concerning the behavior of a photomultiplier at liquid Argon temperature is the decreasing of the photocathode efficiency, due to the semiconductor nature of photosensitive materials. The *quantum efficiency* of the photocathode, defined as the ratio between the number of photoelectrons emitted and the impinging photons, is well known to be a function of temperature. The quantum efficiency strongly affects the output of the PMTs, in fact the number of photoelectron  $N_{phe}$  emitted by the photocathode, can be expressed as

$$N_{phe} \propto N_{\gamma}^{prod} \cdot \epsilon_{geo} \cdot \eta$$

where  $N_{\gamma}^{prod}$  is the number of photons emitted by the light source,  $\epsilon_{geo}$  is the geometrical efficiency of the detector<sup>2</sup> and  $\eta$  is the quantum efficiency. Bialkali photocathodes have a rapid drop of the response at low temperature due to their increased resistivity (about  $10^6$  times higher than that of multialkali materials at cryogenic temperature). In this way the emission of a large number of photoelectrons by the photocathode can produce a local voltage decrease not recovered in short time due to the high resistivity of the material. On the other hand a bialkali materials can offer an enhanced sensitivity to the wavelength from the ultraviolet region up to  $700nm$ . The *radiant sensitivity*<sup>3</sup>, directly connected to the quantum efficiency, is plotted in fig (5.3) for some of the commonly used photocathodes, and, as we can see, the bialkali photocathode  $300k$  ( $K_2CsSb$ ) is the one with the maximum sensitivity in the range  $300 - 650nm$  and has a peak corresponding to blue light.

According to the above consideration the solution adopted for the ETL model 749 and 750 photomultipliers is the use of bialkali photocathode ( $K_2CsSb$ ) evaporated onto a thin Platinum layer ( $50\text{\AA}$ ). Such layer has to be thick enough to avoid any local distortion of the fields due to a charge localization, and at the same time, thin enough to reduce as much as possible the photon absorption. This solution has been investigated by the



<sup>2</sup>defined as the ratio between the number of photons impinging the photocathode and the number of emitted photons.

<sup>3</sup>defined as the ratio between the current emitted from the photocathode and the incoming radiant photons flux

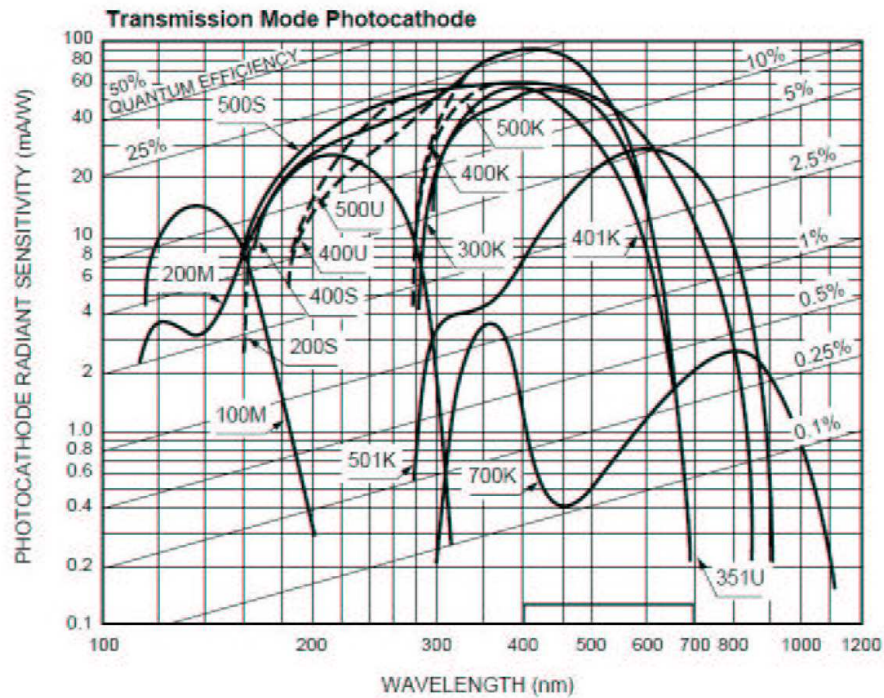


Figure 5.2: Spectral response for some materials commonly used as photocathodes. The bialkali photocathode  $K_2CsSb$  is labelled as 300k.

ICARUS collaboration, measuring the radiant sensitivity as function of the light pulse rate for ( $K_2CsSb$ ) and ( $K_2CsSb + Pt$ ) photocathodes. A LED emitting at  $470nm$  (blue light) has been used. The relative variation of the sensitivity  $R(\lambda, \nu) = S_k(T = 77K, \lambda, \nu) / S_k(T = 300K, \lambda, \nu)$  between liquid Nitrogen and room temperature is reported in fig. (5.3): as we can see, using a Platinum layer it is possible to have a good stability even with a large amount of light stimulation.

References::[43],[44],[47]

### 5.3 AIM OF THE TESTS

The main aim of the work made in the Napoli's laboratory during the period February - November 2005 was to made some preliminary tests on the first prototype bunch of photomultipliers (both of 2" and 3") and at the same time to build the facility for the tests of all the photomultipliers arriving from the factory. The aim of the WARP experiment of the detection of rare events needs the characterization of the PMTs and a good knowledge of its

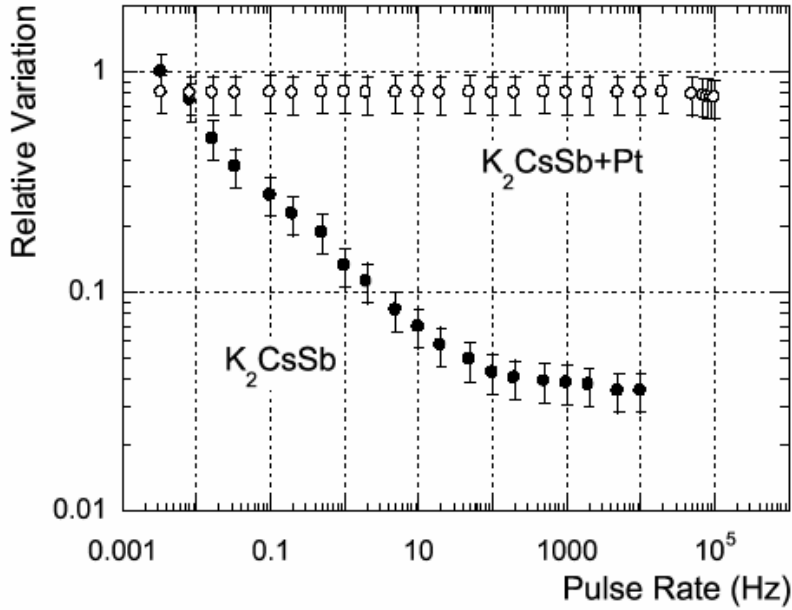


Figure 5.3: Relative variation of the photocathode sensitivity respect to the light pulse rate for ( $K_2CsSb$ ) and ( $K_2CsSb + Pt$ ) photocathodes (measurements carried out using a LED (Laser Emitting Diode) with a central emission at  $470nm$  .

behavior.

The main requirements of the preliminary test was, first of all, to check the performance of each photomultiplier both at room and cryogenic temperature. Moreover the photomultipliers' behavior has been investigated in many different conditions monitoring the stability of gain and rate during a long period of activity both in dark condition or after a strong illumination and both at room and cryogenic temperature. The response to single photoelectrons (SER), a voltage signal coming from a charge integrator, is directly related to the PMT gain, so the study of the SER was carried out in all the condition of temperature (room temperature, cooling and cryogenic temperature) and with dark condition or under a controlled emission of light. The dependence of the gain on the amplitude of the anodic voltage has been also investigated. Defining  $V_0$  as the value supplied to a voltage dividers<sup>4</sup> and  $n$  the number of dynods ( $n = 12$  for the EMI's PMTs), the gain  $g$  can be written as

<sup>4</sup>during the test the dynodic chain was provided by the proper voltages trough a voltage divider of the anodic voltage and the the cathode was grounded.

$$g = (a \cdot V^k)^n = a^n \left( \frac{V_0}{n+1} \right)^{kn} = A \cdot V_0^{kn}$$

where  $a$  is the collection efficiency<sup>5</sup> and  $k$  is a parameter defined by the dynodic material (typically  $k \approx 0.7 \div 0.8$ ). Thus an exponential dependence of the gain on the anodic voltage should be provided.

Other measurements regarded the investigation of the linearity response of the PMTs. It is well known that a un-linear behavior can affect the output of the PMTs if stimulated by a large amount of light<sup>6</sup>, due by a non-linear response of both cathode and anode. The un-linear behavior of the photocathode can be produced by a decreasing of its quantum efficiency, because the emission of hundreds of photoelectron can produce a charge localization on the cathode that can decrease the quantum efficiency (if note correctly removed). This behavior could be more effective at cryogenic temperature if a reduced resistivity can produce large charge pile. Typically a conducting layer can remove the charge pile, avoiding the decreasing of the quantum efficiency, as show in section (5.2). The anodic un-linearity can be caused by the voltage divider or by the dynodic chain. A saturation effect of the anodic current or a charge localization on the dynodic chain can produce a un-linear behavior of the PMT output. The liner behavior of all the PMTs has been tested using a LED, and both the response during the lightening and the recovery of the PMTs' output after the lighting have been monitored. As we will see later, a long time (days) was necessary for such type of measures.

The dark current has been also investigated, i.e. the current that flows in the anode circuit when voltage is applied to a photomultiplier in total darkness. The effect of the various causes of dark current varies according to the operating and environmental conditions (applied voltage, gain, temperature, humidity etc.), and also according to the tubes history (past storage and illumination conditions, etc.). A part of background radiation coming from the contamination of the materials and the cosmic rays, the permanent causes of dark current (i.e. those that are independent of the history of the tube) are mainly leakage currents and thermionic emission from cathode and dynodes. In the last case, the emission is described by the Richardson law

$$j = AT^2 \exp\left(\frac{-W_{th}}{kT}\right)$$

where  $j$  is the current density,  $A$  a constant,  $T$  the absolute temperature,  $k$  the Boltzmann constant and  $W_{th}$  is the thermionic work function of the

---

<sup>5</sup>defined as the ratio between the number electrons emitted by the photocathode and the number of electrons that can be amplified through the dynodic chain.

<sup>6</sup>a stimulation of thousands of photoelectrons with an high repetition rate (tens of kHz or more)

<i>D749Q 2" Quartz G=1.3 ·10<sup>7</sup></i>			
PMT	V [500 A/lm] (V)	CB	Dark current (nA)
102	1583	7.8	3.380
103	1481	7.6	2.020
106	1315	6.4	2.300
107	1843	7.7	1.572
108	1312	5.4	1.003
111	1342	5.1	2.780
112	1373	6.2	2.580
113	1150	5.1	3.380
114	1458	5.2	2.780
115	1170	5.1	7.790

Table 5.1: Nominal characteristics of the PMT 2". See text for details.

photocathode material. Thus the thermionic emission should be strictly dependent on the temperature. During the tests the dark count at cryogenic temperature and at room temperature has been evaluated.

In addition to gain and rate other parameters have been measured: to evaluate the relation between the signal coming from the thermionic emission of the photocathode and the electronic noise, the ratio between the amplitude of the peak of the Gaussian and the amplitude of the valley has been measured; moreover the ratio between peak and sigma of the Gaussian has been used to parameterize the width of the signal of the single electron response. As said before the photomultipliers' outputs have been acquired both in dark condition and under a controlled emission of lights. In the last case three different amounts of light have been considered: single photoelectron, few photoelectrons and many tens of photoelectrons. It must be noticed that during the period of data taking, the output of one PMT could be acquired using the MCA. In this way such type of measure required a long time, mainly to recovery the stability of the photomultipliers' behavior after the strong illumination.

In tables (5.1,5.2,5.3) them nominal characteristic at the nominal gain ( $1.3 \cdot 10^7$ ) of the tested PMTs are reported. The serial number, the voltage at the nominal gain, the radiant sensitivity<sup>7</sup> and the dark current are reported.

References:[43],[44],[47],[45]

---

<sup>7</sup>*corning blue* typically measured using a blue light source (430nm) placed in front of the window (expressed in A/lm).

<i>D750Q 3" Quartz G=1.3 · 10<sup>7</sup></i>			
PMT	V [500 A/lm] (V)	CB	Dark current (nA)
102	1297	5.7	.3400
104	1089	5.9	0.300
105	1075	5.5	0.600
107	1008	5.9	0.500
109	1038	5.4	1.500

Table 5.2: Nominal characteristics of the PMT 3" (quartz window). See text for details.

<i>D750 U 3" Glass G=1.3 · 10<sup>7</sup></i>			
PMT	V [500 A/lm] (V)	CB	Dark current (nA)
1003	1465	6.2	0.300
1004	1311	5.7	0.240
1005	1450	6.3	0.240
1007	1320	5.5	0.540
1009	1545	5.4	1.500

Table 5.3: Nominal characteristics of the PMT 3" (glass window). See text for details.

## 5.4 PMT TEST FACILITY

### 5.4.1 MECHANICAL SET-UP

In order to characterize the photomultipliers' operating performances at cryogenic temperature, we set-up a PMT Test Facility (PTF) in our Naples laboratory. The costs of the test are minimized by performing all the measurements in liquid Nitrogen at the temperature of 77K which is not far from that of liquid Argon (87K). A 3000 litre dewar containing liquid Nitrogen and a vacuum isolated cryogenic adduction line have been installed outside the laboratory in Naples. In order to characterize the PMTs both at room and cryogenic temperature we designed a test system consisting of a cylindrical dewar, 60 cm diameter, 1.2 m height, containing the liquid nitrogen where the phototubes are immersed (fig 5.4). In a first stage mechanical structures made of two different materials (polycarbonate and plexyglass) have been built to sustain of both the 2" and 3" photomultipliers. Finally the polycarbonate has been chosen due to its better mechanical resistance



Figure 5.4: Left: Side view of the dewar used to house the PMTs during the tests both at room and cryogenic temperature.  
 Top,right: view of the optical components inside the light box. LED, lens and fiber are placed on the railway.  
 Bottom,right: view of the a set of PMTs under test with the mechanical sustaining structure.

to the cryogenic temperature. The mechanical structure may host up to 24 2" phototubes or an equivalent number of 3" tubes. At the center of the structure a hole permits the passage of a Quartz optical fiber ( $600\mu m$  of core diameter) which illuminates the immersed PMTs. The dewar is closed by a flange equipped with several feed-through for the HV, the signal cables and the optical fiber (fig 5.4).

In order to test the PMT response and stability as a function of the incoming light a dedicated controlled illumination device (Light Box) has been designed and realized. The light used for the tests is produced by a high intensity blue LED (Kingbright mod. L934MBC) that has a typical emission wavelength of 440 nm. The LED is driven by a programmable

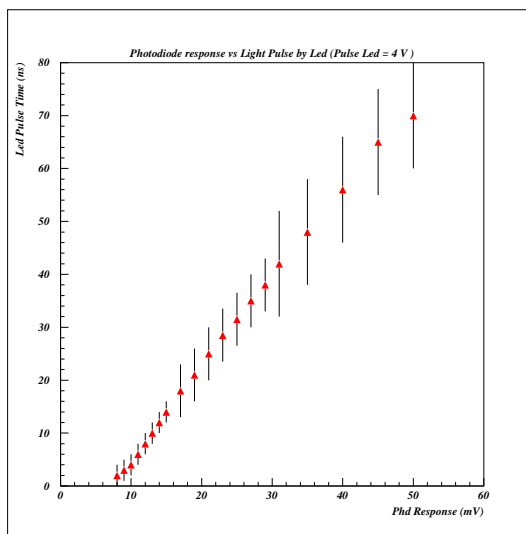


Figure 5.5: Response of the photodiode as function of the pulsing time of the LED.

pulse generator both in short pulses mode ( $t \approx 10ns$ ) and long pulses mode ( $t \approx 5\mu s$ ) in order to reproduce the conditions and the amount of light of typical events in the WARP detector. A focusing lens is placed between the led and the holder of the fiber in the Light Box in order to maximize the amount of light coming from the LED into the fiber. A system of calibrated optical filters can be also used to attenuate the light directed to the Quartz fibre. Part of the LED light is collected in the Light Box by a photodiode (Centrovision mod. OSD5.8-7 U) used to monitor the amount of light effectively emitted in each pulse. The photodiode signal is amplified by a fast, high-sensitivity charge integrator and readout by the data acquisition system. Both lens, LED, holder of the fiber, filters and photodiode are placed on a rail-way, and a micrometric positioning of each component is allowed, giving a complete control of the amount of light coming into the dewar. The response of the photodiode has been tested using the LED as light source. As we can see in fig (5.5), the output of the photodiode as function of the pulsing time of the LED has a linear behavior.

The lightening system has been designed to produce the wide range of light required to reproduce the single electron response and to study the response of the photomultipliers to a light of many tens of photoelectrons. Nevertheless the study of the response of the photomultiplier up to 100 photoelectron has been performed using an high intensity led placed directly in the dewar containing the photomultipliers, in the gaseous phase upside the liquid. In this way the large amount of light has been produced using

really short pulses ( $t \approx 10ns$ ). Due to the fact that the photomultipliers to the bottom of the dewar, its inner base have been covered by a tiny reflector layer in order to improve the diffusion of the light inside the dewar and to get an uniform lightening. The measurements at cryogenic temperature were carried out at 77 K with the PMTs directly immersed in liquid Nitrogen. To guarantee as much as possible an uniform cooling and to prevent any strong mechanical stress the dewar was previously filled with liquid nitrogen and the sustaining structure of the PMTs was quickly immersed in the Dewar. Only one of the tested PMTs could not withstand the thermal shock. During the first phase of the tests the level of the liquid has been monitored by opening the dewar, starting from June a level meter was developed using six PT1000 thermal resistors; thus the level of liquid was well-known by the number of resistances immersed in the liquid, avoiding, in this way, the opening of the dewar. The Dewar has been closed and kept in complete darkness during the tests. Periodical refills are made in order to keep the PMT always immersed in the liquid.

In order to distribute the proper electrical potential to the dinodes during the tests, each PMT was equipped with a voltage divider, realized using printed circuit boards with thick resistors ( $R = 1M\Omega$ ) soldering directly on the PMT output leads. The voltage distribution was set to have the ground on the photocathode, the first dynode at 300 V for the 2" and 450 for in the 3" as suggested by data sheet. During the test the nominal anodic voltages (at 500  $A/lm$ ) have been used for all the PMTs. We decided not to change those value during all the tests except during the gain test, when the anode's voltage has been changed and then brought back to its original value.

#### 5.4.2 DATA ACQUISITION AND ANALYSIS SOFTWARE

The scheme of the data acquisition system is shown in fig (5.6). The system has been designed with five read-out channels used to acquire the spectra of anodic signals from five PMTs. Each channel consists of an HV decoupling and a preamplifier. The PMT output was directly decoupled by the anode HV using a  $10nF$  capacitor. The preamplifier, a Camberra *mod.2005* has a conversion factor of  $4.5mV/pC$ . With the help of a switch it is possible to sequentially connect each of the five r/o channels to an amplifier and to a MCA. The signals amplitude is recorded by the means of an ORTEC Multichannel Analyzer board installed onto a personal computer, allowing the analysis of the spectra up to a maximum amplitude of 12V. The present system allows for single channel measurements, although up to five different tubes can be read-out at the same time. In order to acquire the output of a photomultiplier under light stimulation, a trigger system has been developed. A circuit based on the Motorola LS123 (Monostable multivibrator) receives the synchronization signal by the LED's driver and produces a TTL

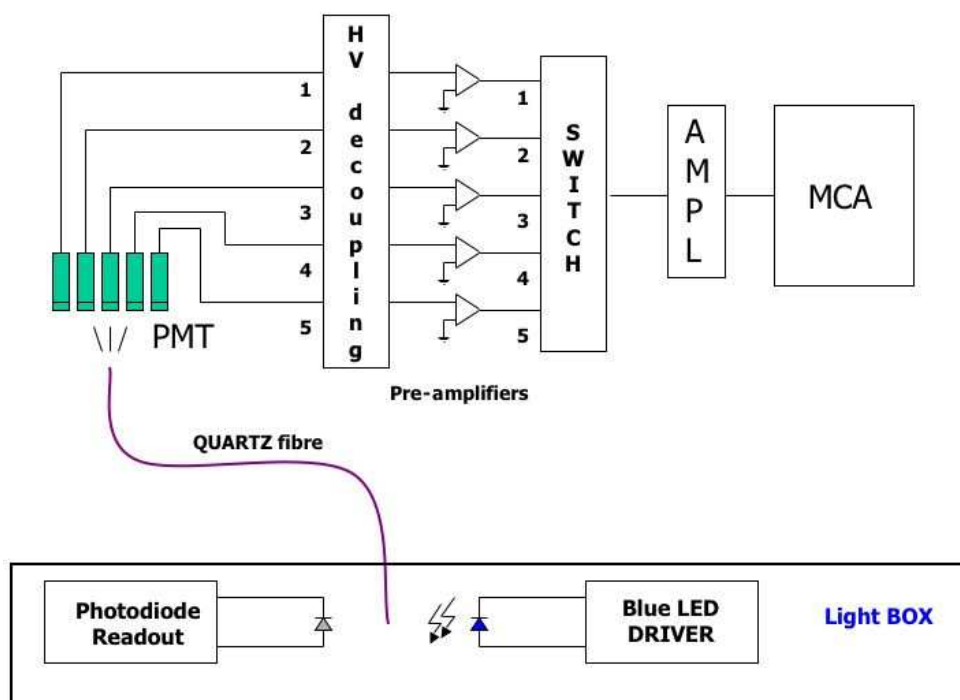


Figure 5.6: Schematic representation of the experimental set-up and of the data acquisition system.

gate signal for the MCA . A gate of  $10 \div 20 \mu s$  of length is sent to coincidence input.

The spectra have been acquired using the Maestro software (working on the MCA computer), allowing the recording of the spectrum data (channel and number of counts) and of some additional information like date, live and total acquiring time. Two software mainly based on MINUIT and PAW have been developed in order to get a tool for data analysis. The first one carry out the fitting of the spectra in two different ways: an automatic method is typically used to fit many spectra of the same photomultiplier acquired in succession, while an a interactive method, which gives the possibility of a control of the fitting procedure at each step is typically used to fit data of different PMTs. The second software, based on PAW, read the fit parameters of all the fitted spectra and perform the reconstruction of the interesting variables such as gain, rate, peaks ..etc, giving a graphical framework for the data analysis. Three different functions have been used to fit the spectra acquired with or without led stimulation. The basic function that can be used to fit the single electron response is given by the sum of a Gaussian and

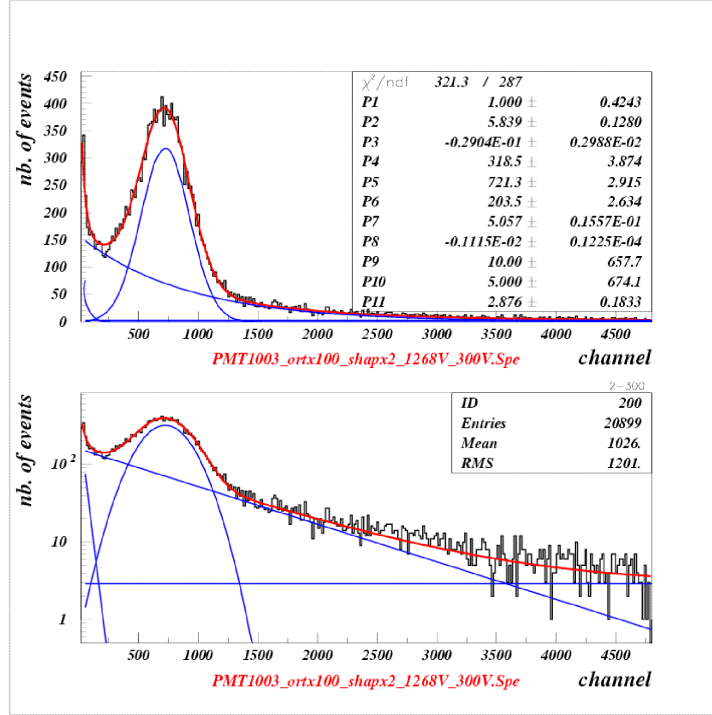


Figure 5.7: Typical dark spectrum in linear (top) and logarithmic (bottom) scale. The single electron peak is clearly visible with contributions of coming from the electronic noise and from the thermoionic emission of the dynodes at small amplitude. The long high pulse tail is attributed to scintillation induced by natural radioactivity contamination in the PMT itself and cosmic ray particles.

an exponential function, in order to take in account the signal due to a single electron emission and physical events giving a higher pulse height. Anyway a more complex function has been used to fit such type of spectra. To take into account the high noise in the first part of the spectrum (typically due to a dinodic emission of electrons) and the few events in the last part of the spectrum (producing long tail) an additional quickly decreasing exponential function and a constant function, respectively, have been added to the fitting function. The large amount of spectra fitted during the data-taking (more than 5000 spectra) has demonstrated that the function

$$f_{SER}(x) = e^{(\alpha_1 + \alpha_2 \cdot x)} + \alpha_3 \cdot e^{(-\frac{1}{2} \cdot ((x - \alpha_4) / \alpha_5)^2)} + e^{(\alpha_7 + \alpha_8 \cdot x)} + \alpha_9 \quad (5.1)$$

well represent our data (fig 5.7). Two different functions have been used to fit the spectra taken under led stimulation depending on the amount of

light generated. In the case of light corresponding to a few photoelectrons the acquired spectra have been analysed disentangling the response as sum of the different contribution of 1,2...n photoelectrons. Thus the used fitting function has a variable number of Gaussian terms in order to take into account the contribution of many photoelectrons. The mean values and the standard deviation of the higher order gaussian terms are fixed using  $\bar{x}_i = i \cdot \bar{x}_1$  and  $\sigma_i = \sigma_1 \sqrt{i}$  where  $i = 1, 2 \dots n$ . The function used was:

$$f_{Ln}(x) = e^{(\alpha_1 + \alpha_2 \cdot x)} + \sum_{i=1}^n \alpha_{3_i} \cdot e^{(-\frac{1}{2} \cdot ((x - \alpha_{4_i}) / \alpha_{5_i})^2)} + e^{(\alpha_7 + \alpha_8 \cdot x)} + \alpha_9. \quad (5.2)$$

In the case of higher light stimulation (signal corresponding to many tens of photoelectrons) just a single Gaussian function has been chosen as fitting function.

$$f_L(x) = \alpha_1 \cdot e^{(-\frac{1}{2} \cdot ((x - \alpha_2) / \alpha_3)^2)}. \quad (5.3)$$

During the fitting procedure the initializations of all the parameters of the previous functions occurs in an automatic way by a recognition of the shape of the spectrum using a code compiled each time under the PAW program. Thus it has been possible to avoid a random (or human) initialization of the parameters, and to make the procedure completely automatic (and really quick). Finally a control of the value of the  $\chi^2$  of each fit has been applied in order to eventually reject misbehaviors.

*References::*[45],[46]

## 5.5 RESULTS

### 5.5.1 DARK COUNTS AND SINGLE PHOTOELECTRON RESPONSE

The average shape of the anode pulses originated by single thermoionic electrons has been recorded with a digital oscilloscope Lecroy 6050A by feeding directly the decoupled anodic output to the 50 Ohm input of the scope. The obtained waveform is shown in fig. (5.8) for two PMTs type D750. The pulse shapes of the 2" PMTs do not show significant differences with a leading edge of 3.0 ns and a trailing edge of 3.1 ns . The plot shows the presence of secondary peaks due to multiple reflections of the signal at the mismatched ends of the cable. Anyway they should not have any influence onto the output after the integration of the signal. The typical spectrum (5.7) shows a narrow single electron peak with contributions of small amplitude pulses coming from the exponentially falling electronic noise and from the thermoionic emission of the dynodes. A long high pulse tail is attributed to multi-photoelectron events due to Cherenkov light emission

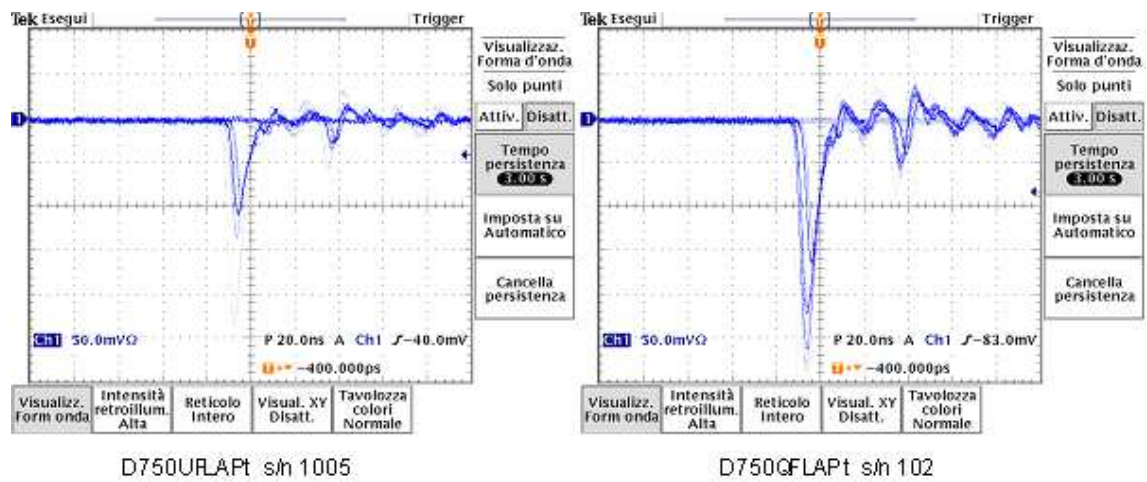


Figure 5.8: Shape of the anode pulses originated by single thermionic electrons. Reflections of the signal produce the peaks following the first.

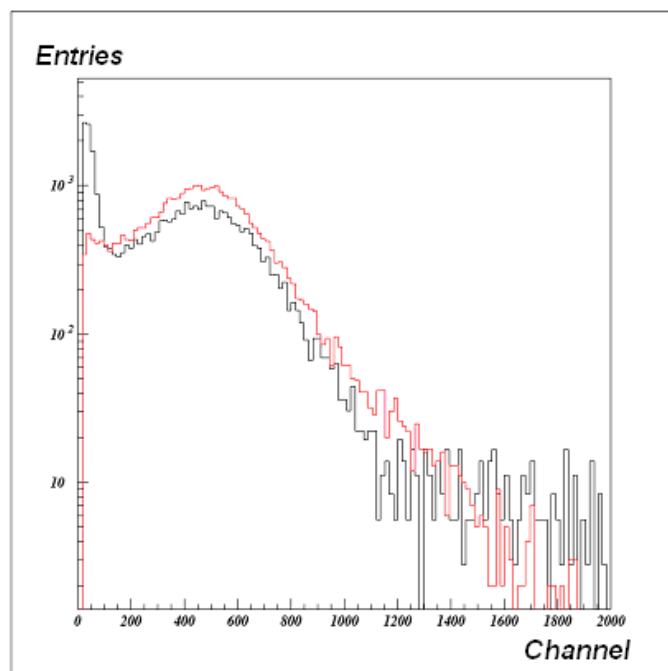


Figure 5.9: SER spectrum obtained with light stimulation (red) compared with the naturally occurring PMT dark noise charge distribution (black).

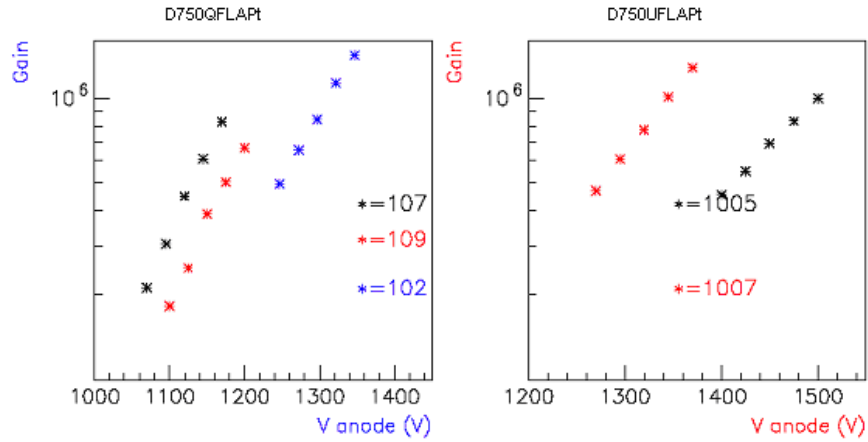


Figure 5.10: Dependence of the gain on the anodic voltage at room temperature. The PMTs exhibit the well known exponential behavior.

of cosmic ray particles and scintillation induced by natural radioactivity contamination in the PMT itself.

The achievement of single photoelectron equivalent illumination for the PMT was determined assuming that the number of photoelectrons leaving the PMT cathode is described by the Poisson distribution. Under this assumption, the probabilities to detect one or two photoelectrons, respectively  $P(1)$  and  $P(2)$ , are related by

$$\frac{P(2)}{P(1)} = \frac{\mu}{2} \quad (5.4)$$

where  $\mu$  is the mean value of the Poisson distribution. In order to keep the probability of the emission of more than one photoelectron smaller than 1% it is necessary to keep the mean value below 0.02. Adjusting the light to a level such that the PMT pulse rate above a threshold of 0.x phe was a fraction  $\mu$  of the light pulse rate fulfilled this requirement. Fig. (5.9) shows a SER spectrum obtained in such conditions (in red) compared with the naturally occurring PMT dark noise charge distribution (black).

We do not observe a significant difference between the two spectra. This feature of the PMTs under test permits to use the dark spectrum peak for the measurement of the gain.

The behavior of the PMT gain has been studied in many different conditions. The dependence of the gain on the anodic voltage both at room and at cryogenic temperature has been tested for all the PMTs. In fig. (5.10) the gain of some PMTs of 2" (D750 samples) is reported for different values of the anodic voltage at cryogenic temperature. As we can see, the PMTs exhibit also at 77 K the well known exponential behavior (see section 5.3)

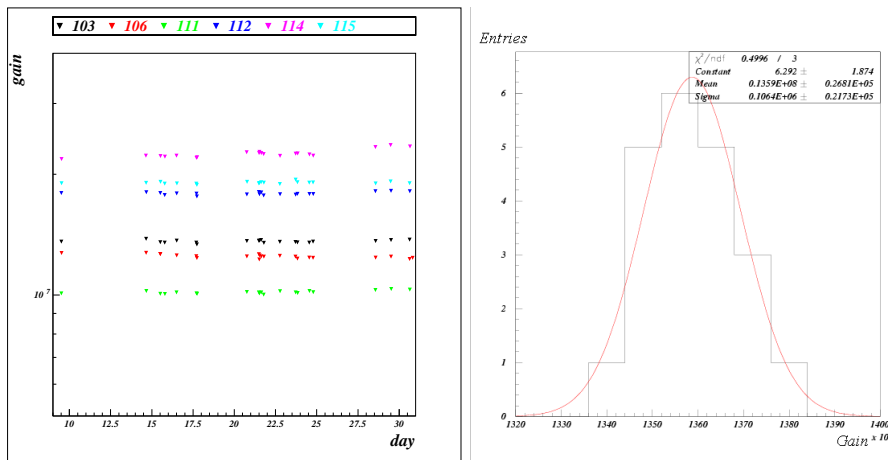


Figure 5.11: Behavior of the PMTs gains as function of the time (left) for 2'' PMTs. During the measurements PMTs were in dark condition at room temperature. The gain remains very stable in time with a variation of the order of 0.8 % (right PMT nb. 114)

### Long term stability

The implemented set-up allowed the monitoring of the PMT response in dark condition for a long period both at room and cryogenic temperature. Thus a good long term stability has been verified and the cold operation of the devices has been confirmed. In fig.(5.11) the values of the gain at room temperature during 20 days of monitoring is reported for the 2'' PMTs. As we can see, all the PMTs show a good stability during the whole period. Nevertheless it must be noticed that a gain similar to the nominal value ( $1.3 \cdot 10^7$ ) has been obtained by only two PMTs (number 103 and 106), while all the monitored gains were in the range  $[1.0 \cdot 10^7, 2.1 \cdot 10^7]$ . In fig. (5.12) the ratio between the variance and the peak of the gaussian used to fit the SER spectrum ( $\sigma/peak$ ) and the ratio between the amplitudes of SER's peak and valley ( $peak/valley$ ) are reported. Although different values have been measured, the results demonstrate the good stability of the PMTs and good performances in terms of charge resolution. Both 2'' and 3'' PMTs showed the same behavior at cryogenic temperature. The gain remains very stable in time with a variation of the order of 0.5%, during many days of data taking. In fig (5.13) the relative variance to the peak is shown for a 3'' PMT during the data taking at LNGS at cryogenic temperature. As we can see, the mean value is of the same order of the values obtained at for 2'' PMTs and the stability during more than two months is impressive.

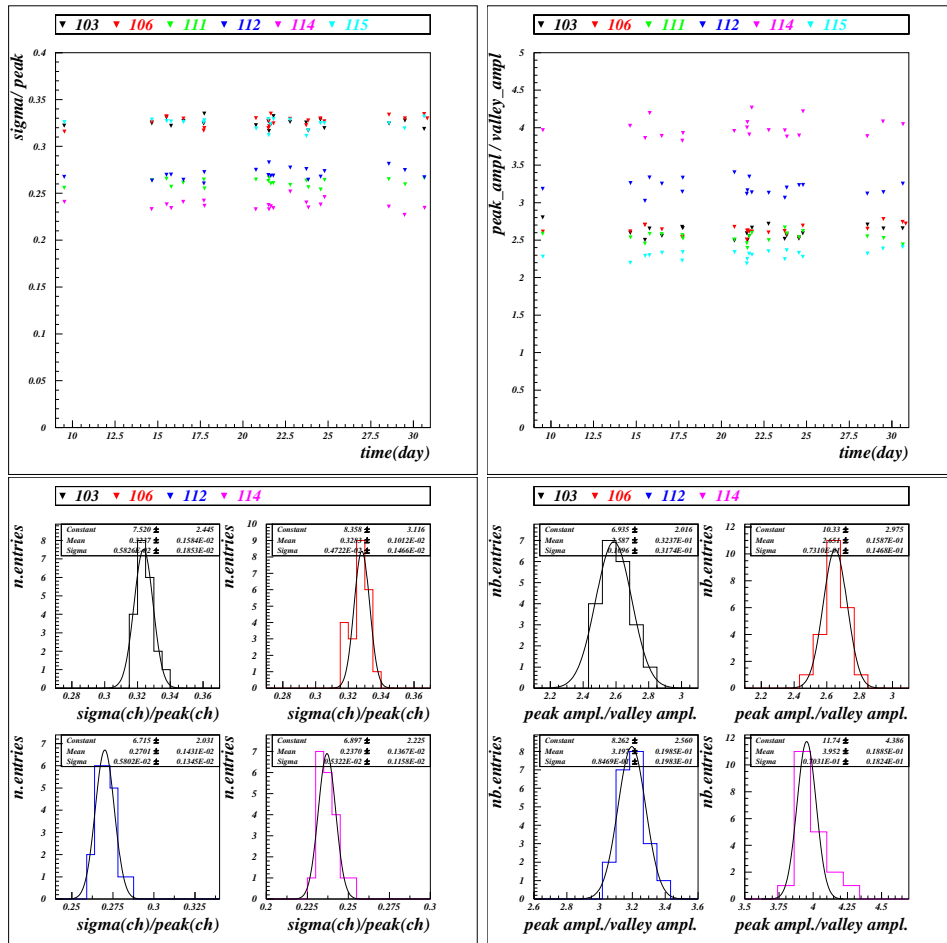


Figure 5.12: Top:  $\sigma/peak$  (left) and  $peak/valley$  (right) ratios as function of the time. During the measurements PMTs were in dark condition at room temperature.

Bottom: distributions of the ratios  $\sigma/peak$  (left) and  $peak/valley$  (right). As we can see the PMTs nb 114 is characterized by the best performances ( $\sigma/peak \approx 0.23$  and  $peak/valley \approx 3.9$ ). PMT nb.106 has the worst value of  $\sigma/peak$  ratio ( $\approx 0.32$ ), while PMT nb. 115 has the worst value of the  $peak/valley$  ratio ( $\approx 0.23$ ).

### Comparison of the responses at room and cryogenic temperature

During the cooling, the PMTs gains showed strong variations. Soon after the immersion in liquid Nitrogen, the gain has a quick rise followed by a quick decreasing to a value typically lower than the room temperature value. This effect, although not completely understood, could be due by a decreasing of the collection efficiency of the dynodic chain produced by mechanical

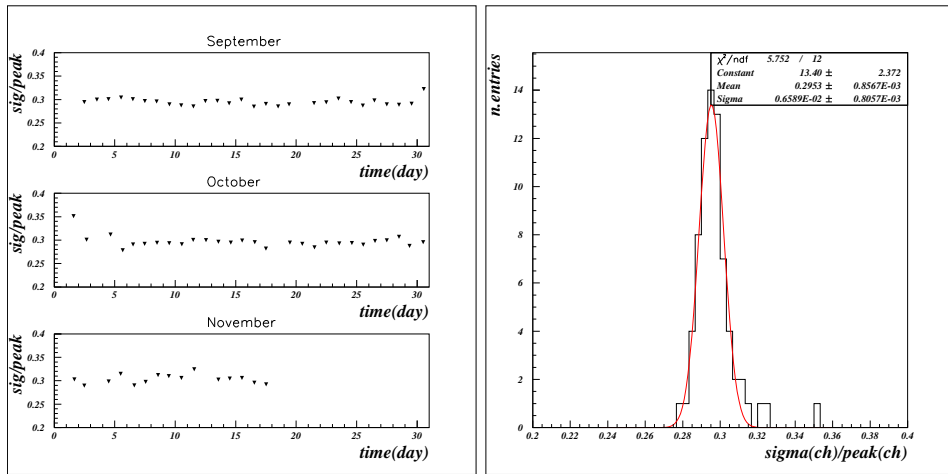


Figure 5.13: Left: Behavior of the ratio  $\sigma/peak$  as function of the time for the 3'' PMT nb. 104. During the measurements the PMT was in dark condition at cryogenic temperature. Right: distribution of the ratio  $\sigma/peak$  for the same PMT. The narrow distribution is peaked at  $\approx 0.3$

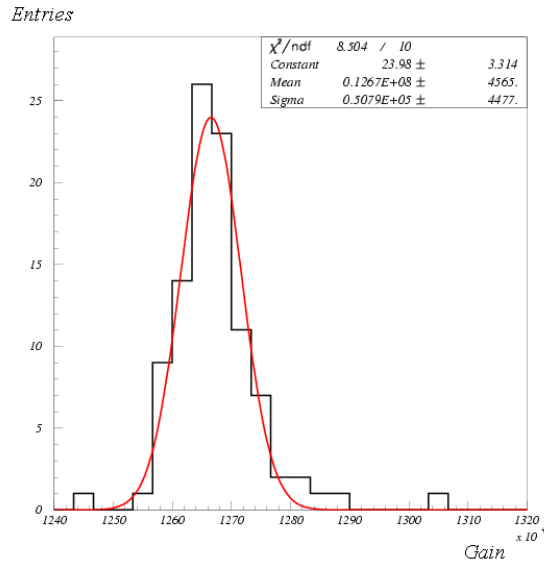


Figure 5.14: Distribution of the gain at cryogenic temperature for the PMT nb. 114 (24h of measurements). After a stabilization period ( $2 \div 3$  days) the gain is stable at the average value of  $\approx 1.27 \cdot 10^7$  with variations of the order of 0.4%.

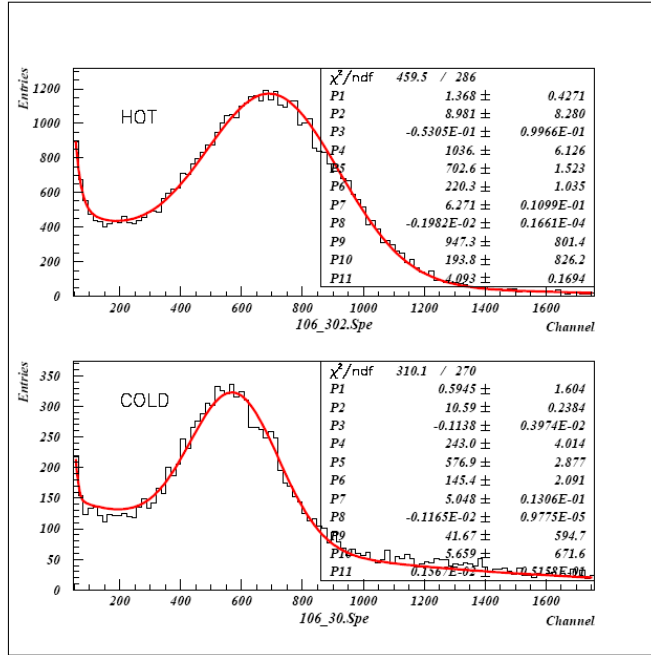


Figure 5.15: Dark spectra acquired for the same PMT (nb.106) at room (top) and cryogenic temperature (bottom). A decreasing of peak and rate are clearly visible at  $LN_2$  temperature.

arrangements. In fig. (5.14) the gain distribution, obtained of the PMT nb. 114 after the stabilization period (2 ÷ 3days), is shown. The average value is about the 7% less than the value obtained at room temperature (see fig. 5.11) with variation of the order of  $\approx 0.4\%$ . As stated in section (5.3), a decreasing of the dark rate is expected at  $LN_2$  temperature. In fig. (5.15) two different spectra of the PMT n. 106, acquired in different condition, are compared. A decreasing of the gain ( $\approx 18\%$ ) between room and cryogenic temperature is clearly visible<sup>8</sup>.

### 5.5.2 MULTIPHOTONS RESPONSE

In order to check the linearity of the PMT response to light pulses producing more than one photoelectron the amount of light was progressively increased. The output charge distribution recorded under such conditions is reported in fig. (5.16); the peaks due to multiple photoelectrons contributions, 3 in one case and 5 in the other, are clearly visible. The measured distributions can be analysed to disentangle the response of the multiplier chain to n-electrons

<sup>8</sup>as stated before the gain can be directly measured using the dark spectrum peak.

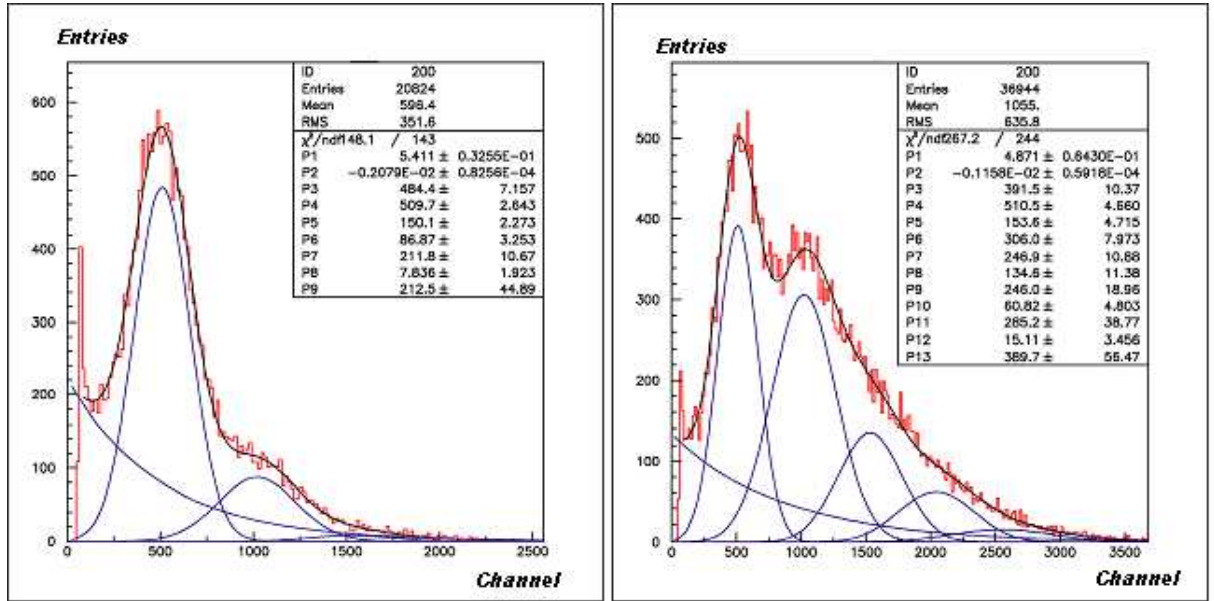


Figure 5.16: Response under light pulses producing more than one photoelectron. The contribution of two photoelectrons (left) and five photoelectrons (right) are clearly visible.

bursts. The results of this analysis are reported in fig (5.16): as expected the individual contributions could be fitted using a variable number of additional Gaussian terms besides the one due to the first electron. Furthermore, the analysis shows that, given  $x_1$  and  $\sigma_1$ , respectively the mean value and the standard deviation of the single photoelectron response, then the mean value and the sigma of the response to  $n$  photoelectrons satisfy the following relations  $x_n = nx_1$ ,  $\sigma_n = \sigma\sqrt{n}$ ,  $P_n = \frac{\mu}{n}P_{n-1}$  where  $P_n$  is the number of events under the  $n$ -th Gaussian, according to the Poisson statistic with the mean number of detected photoelectrons. The working conditions in the WARP 100 litre detector are such that a maximum of about 200 photoelectrons are foreseen on each PMT as primary signal (S1), a large part of which being emitted in few tens of nanoseconds. On the other hand, as many as 2500 photoelectrons per PMT can be due to the secondary signal (S2) in a time scale of few microseconds. The event rate is expected to be of the order of 100 Hz, mainly due to the  $^{39}\text{Ar}$  and  $^{85}\text{Kr}$  contamination of Argon itself. Under these conditions possible effects of saturation and fatigue have to be considered. For this reason, a dedicated test has been performed in order to characterize the PMTs under moderate to high illumination conditions at cryogenic temperature. A first set of measurements was performed on five 3" samples: three of the type D750Q and two D750U. The tubes

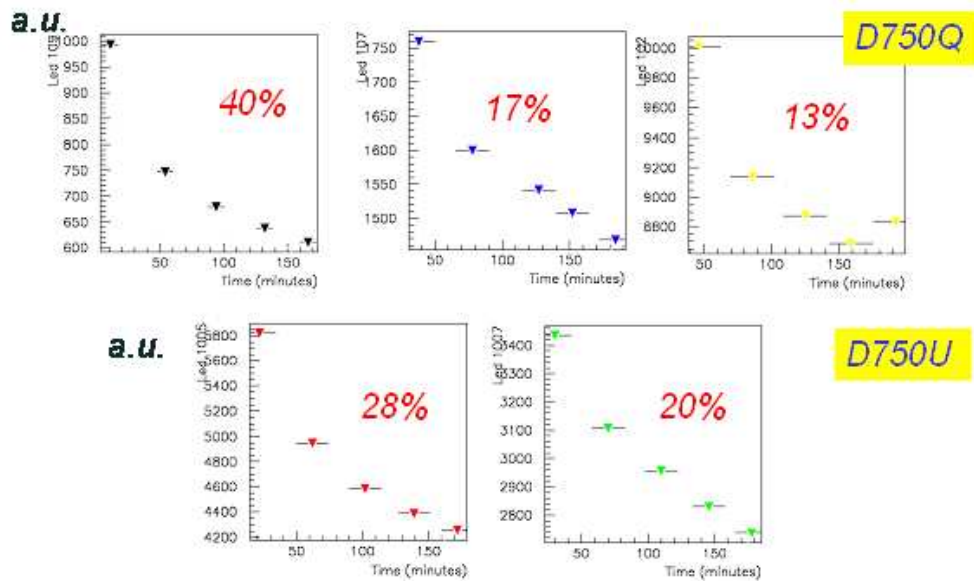


Figure 5.17: Response of the PMTs to intense light pulses: all the sample tested suffered from fatigue effects (resulting in a decrease of the response of the order of several percent after 1 hour)

were set at their nominal voltage (see table 1) and allowed to stabilize in liquid Nitrogen. The response of the PMTs to intense light pulses, of the order of 200 phe in 500 ns, was recorded at low frequency. The repetition rate of the LED pulses was then increased to 5 kHz, and the PMT response monitored for a long time. The data plotted in fig. (5.17) show that all the samples suffered from fatigue effects resulting in a decrease of the response of the order of several percent after 1 hour. No saturation of the effect was observed during the measurement and a very slow recovery of the response could be seen once the light source was switched off. In fig. (5.18) the observed response  $R = N_{phe} \cdot \epsilon \cdot G$  is translated into gain by assuming no variation of the collection efficiency ( $\epsilon$ ) and of the number of photoelectrons ( $N_{phe}$ ) and normalizing to the observed gain after illumination. The observations suggest that the decrease of the PMT response to constant light stimulation is caused by a correspondent gain loss. After 10 hours from the end of the stimulation the gain had not recovered its initial value yet. The phenomenon was further investigated on the D749 2" phototubes, to establish the saturation generated by an equivalent photocurrent of very short duration. For this test the blue LED was inserted in the gaseous cap above the cryostat in order to produce up to 100 phe in 16 ns on all the

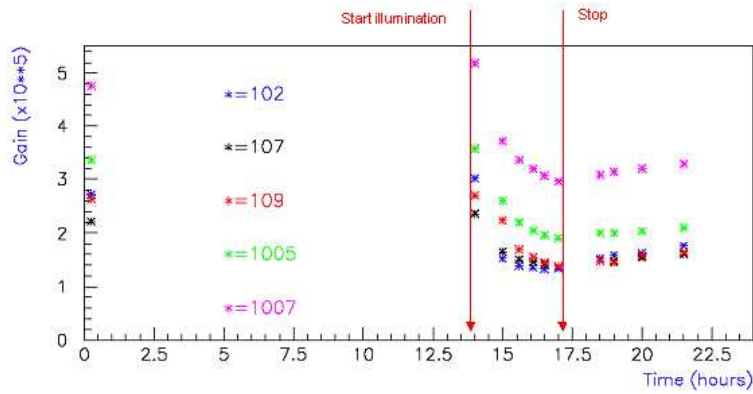


Figure 5.18: Intense light pulses stimulation: the gain variation is estimated by assuming no variation of the collection efficiency and of the number of photoelectrons and normalizing to the observed gain after illumination.

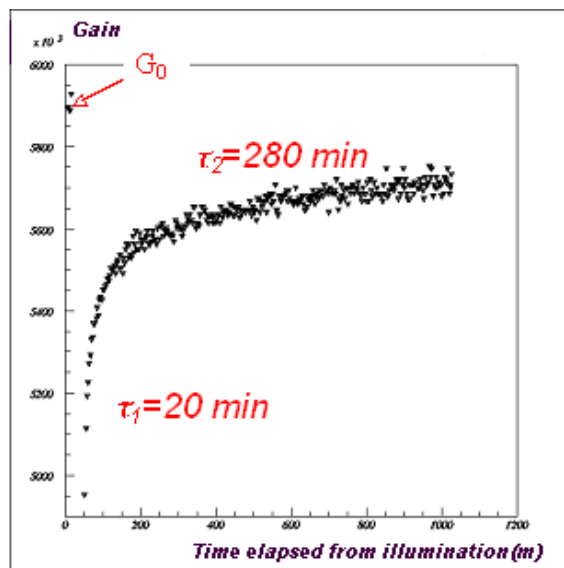


Figure 5.19: Recovery of the gain after an intense light pulses stimulation. All the tested samples all showed a similar behavior, with two different time constants, of the order of 20 and 300 min respectively.

PMTs. The pulse repetition rate was set to 5 kHz and the peak response recorded over 30 minutes. Again a significant decrease of the PMT response was observed. After the illumination, the SER was monitored at regular intervals in order to establish the complete recovery of the gain. The tested samples all showed a similar behavior, with two different time constants, of the order of 20 and 300 min respectively, and asymptotically reaching a gain a few percent smaller than the initial value (see fig. 5.19). Eventually, we decided to progressively increase the light level at a pulse repetition rate of 10 Hz, in order to disentangle the proper saturation effects from the fatigue. During the illumination the gain is monitored acquiring the pulses due to the photocathode thermoionic emission, accounting for the clearly visible SER peak. Tests of this kind were performed on the photomultipliers type D757. Results are shown in fig. (5.20) for PMT no. 1006. All the PMTs showed saturation effects in the range of a few percent when the amount of light reached the 100 phe level. The progressive loss of linearity seems to be largely due to a degradation of gain, which is not recovered when the light is turned off. As a further test, the PMT no 1006 was illuminated for several minutes with pulses corresponding to 100 phe in 10 ns at a frequency of 100 Hz (fig. 5.21). The data show that an increase in the repetition rate results in an unstable behavior, with the gain exponentially falling to values 10% lower than the original one. Finally, the light pulse frequency was varied from 10 Hz to 5 kHz (fig. 5.22). From the data, we can deduce that the gain loss is strongly dependent from the repetition rate. This result, together with the observation that, for a given rate, it depends also on the light intensity, allows us to conclude that the effect is proportional to the integrated luminous flux and as a consequence may be considered a fatigue effect.

## 5.6 POSSIBLE IMPROVEMENTS TO THE SET-UP

The set-up described in the previous sections has been used to perform preliminary tests on the first bunch of PMTs, which have been then used for the data taking in the 2.3l chamber at LNGS. Anyway the set-up has been also thought in order to prepare a facility for a mass test of hundreds of PMTs necessary for the functioning of the 100l detector. Many upgrade to the set-up have been performed during this preliminary test. Some other improvements are now planned in order to increase the automatism and robustness of the testing procedure in view of the massive test of the VETO detector PMTs. To get an uniform lightening of the PMTs inside the dewar as much as possible, two enhanced systems, based on a diffusion lens and on a bundle of fibers, are under study. Moreover we are planning to upgrade

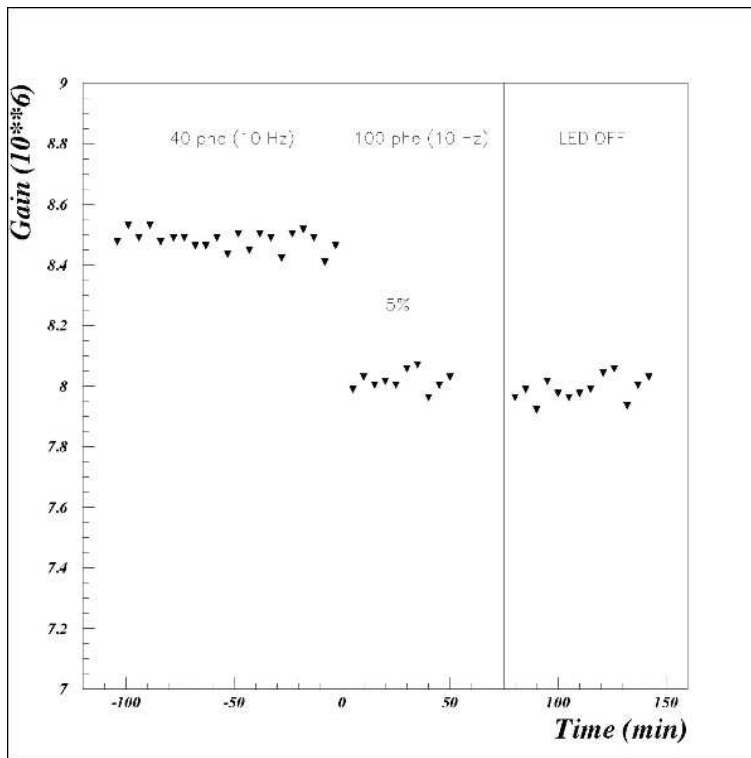


Figure 5.20: Behavior of the gain during the illumination (PMT no. 1006 at cryogenic temperature).

the DAQ system by implementing a VME based architecture, in order to allow the acquisition of many PMTs' output at the same time. Two options are under study: the first one is based on the use of a "charge to digital" converter, or QDC; a possible choice is the CAEN V965 16 channels "dual range" (0-800 pC and 0-100 pC) QDC, which is designed for PMT applications allowing to avoid saturation with large charge pulses while increasing resolution with small ones. The second option we are going to test makes use of a new 2 GHz sampling ADC (CAEN prototype V1729) together with fast preamplifiers.

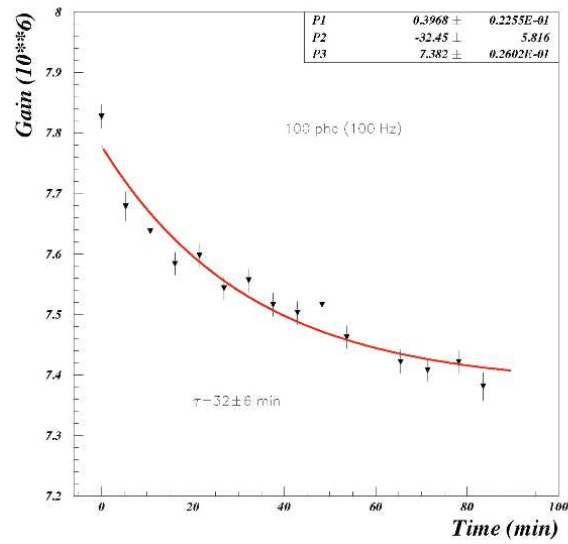


Figure 5.21: Gain exponentially falling to values 10% lower than the original one under illumination (pulses corresponding to 100 phe in 10 ns at a frequency of 100 Hz).

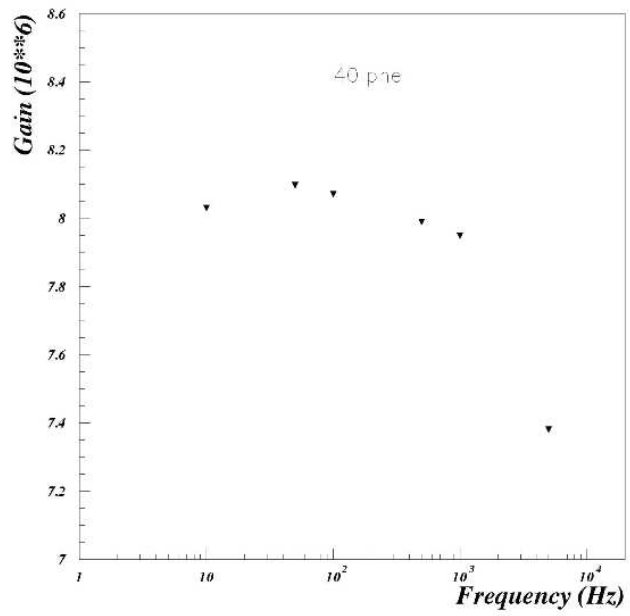


Figure 5.22: Gain variation under illumination. The light pulse frequency has been varied from 10 Hz to 5 kHz .

# SUMMARY

One of the most important goals of modern physics has been the determination of the value and composition of the energy density of the universe. Today several experimental observations, based on different experimental techniques, suggest that the dominant contributions to matter density has an unknown nature: only the 15% of the matter density of the Universe can be explained in terms of baryonic matter, while the largest part constitutes the missing mass of the Universe, the so-called *dark matter*, i.e. that doesn't emit or absorb electromagnetic radiation. The experimental results showed in chapter 1 point out that this unknown mass should be made of a generic class of neutral, non-baryonic and non-relativistic particles called Weakly Interacting Massive Particles (WIMPs). Theoretical predictions suggest that this particles could be relics of the Big Bang and still exist today. Impressively, particle physics predicts the existence of such a type of particle starting from a completely different point of view. Supersymmetry can solve one of the major problems within the Standard Model called the Higgs divergence problem and can make a step towards a theory of the unification of the forces. The theory assumes that, for every Standard Model particle there is a corresponding supersymmetric particle with a different mass. The most promising WIMP candidate is represented by the Lightest Supersymmetric Particle (LSP).

WIMPs are believed to exist in a spherical halo in the galaxy, through which the solar system, and hence the Earth, moves. Those particles could be detectable through the elastic collisions with the atomic nuclei of detectors placed on Earth, although the interactions should be characterized by a very low cross section. Such type of processes can produce a nuclear recoil in a range up to  $100keV$ .

The **WARP** programme (*WIMP ARgon Programme*) aims to obtain an evidence of the WIMPs existence through direct detections of elastic scattering of WIMPs over the Argon nuclei. Very rare WIMP elastic scatterings with matter have to be discriminated from the the dominant electromagnetic background, in order to detect the tiny energy deposition produced by a recoiled nucleus.

As shown in chapter 3, liquid Argon provides the main requests in order

to represent a good sensitive material to detect WIMPs. First of all, it allows to realize large mass detectors; moreover liquid Argon technology is mature enough and well supported at an industrial level to provide the radio-purity required in rare event search; finally it is possible to provide an efficient event by event identification of nuclear recoil and electron interactions. The results presented in chapter 3 show that the simultaneous measurements of the ionization charges and scintillation light, that occur when a particle interaction takes place, can be used to discriminate the nature of the interacting particle. A second (and independent) identification technique is provided by prompt scintillation signal shape analysis. The experimental techniques have been tested using a 2.3l double phase argon chamber prototype, and a really good background rejection power has been shown. The combination of the two proposed identification techniques is able to provide a rejection power of the order of  $10^{-7} \div 10^{-8}$ . A 100l (140kg) of sensitive target detector has been proposed by the WARP collaboration, in order to reach a sensitivity of the order of  $10^{-8} pb$  in the WIMP-nucleon cross section. The detector has been designed particularly taking care of the background reduction.

An active shield is used to reject the events due to neutrons or other particles penetrating from outside or travelling out from the central part. Dimensions of the outer LAr volume are chosen in such a way that the probability for a neutron to interact in the inner detector without producing a signal in the VETO system is negligible, thus only events with no signals in it are potential WIMP-nucleus interactions. Moreover an external passive shield is added to adequately reduce environmental neutron and gamma background and all the materials are characterized by an high radiopurity. Data taking at Gran Sasso national laboratory showed that the most dangerous background component is represented by the  $^{39}Ar$  contamination of the commercial Argon. A  $\beta$ -emission activity of about  $0.76 Bq \cdot (kg \text{ of } Ar)^{-1}$  has been measured using the test chamber. As shown in chapter 4, the rejection power obtained from the combination of the two event-identification techniques is able to reduce the probability of a  $\beta$  interaction mislabeled as nuclear recoil, and a background rate of 1 *event* each  $10 \div 100 \text{ days}$  is expected for the 100l detector.

One of the most interesting activity concerns the test and the characterization of the cryogenic photomultiplier tubes, necessary for the detection of the scintillation light produced in both phases, that, inside the 100l detector, work directly immersed in LAr. As stressed in chapter 5 a PMTs test facility has been prepared in Naples laboratory. The results reported in chapter 5 show that all the tested phototubes are characterized by an high gain and by a good stability at cryogenic temperature. Moreover they showed a very narrow single electron response, indicating a good energy resolution and low

dark noise.

Concluding, the promising result obtained by the 2.3*l* chamber shows the effectiveness of a LAr detector for Dark Matter search. On this base, the 100*l* detector gives not only the possibility of a significant enhancement of actual experimental limits, but allows to test the more favored SUSY models. Moreover, the *LAr* technique is even more promising: although WIMPs signatures could be found with higher event rates, larger sensitive masses are allowed to the LAr technology, giving, in principle, access to the full range of theoretical predictions.

# Bibliography

- [1] G. Jungman, M. Kamiankosky, K. Griest, *Phys. Rep.* 267 (1996), 195;
- [2] M. Roncadelli, *Aspetti astrofisici della materia oscura* Ed. Bibliopolis (2004);
- [3] D. H. Perkins, *Particle Astrophysics* Ed. Oxford Univ. Press (2003);
- [4] G. Bertone, D. Hooper, J. Silk, hep-ph/0404175 (2004);
- [5] T. J. Sumner, *Liv. Rev. in Relativity* 5 (2002), 4;
- [6] G. Chardin, astro-ph/0411503 (2005);
- [7] A. Morales, astro-ph/0211446 (2002);
- [8] L. Bergstrom, hep-ph/0002126 (2000);
- [9] G. Bertone, D. Merrit, astro-ph/0504422 (2005);
- [10] M. Kamionkowski, A. Kinkhabwala, *Ph. Review D* 57 (1998);
- [11] M.S. Turner, E.W. Kolb *the early Universe* (1990);
- [12] G.F. Smoot, D. Scott, astro-ph/9603157 (1995);
- [13] J. D. Cohn, K. Kadota, astro-ph/0409657 (2005);
- [14] W. Hu, *The Astrop. journal*, 506 (1998), 485;
- [15] M. White, D. Scott, J. Silk, *Ann. Rev. Astron. and Astroph.*, 32 (1994), 319;
- [16] J. L. Feng, *Annals of Physics* 315 (2005), 2;
- [17] C. Munoz, hep-ph/0309346 (2004);
- [18] G. L. Kane, *Contemp. Physics* 41 (2000), 359 ;
- [19] D. Wagner, *Introduction to Supersymmetry at the NLC* (1999)

- [20] S. Ei, K. Fujii, T. Kunihiro, hep-th/9905088 (1999);
- [21] Y. A. Simonov, *Jour. of Nonlinear Mat. Phys.* 12, (2005), 625 ;
- [22] J. G. Bellido, astro-ph/0502139 (2005);
- [23] J.D. Lewin, P.F. Smith, *Astropart. Phys.* 6 (1996),87;
- [24] Y.G. Kim *et al.*, hep-ex/0208069 (2005);
- [25] Y. Ramachers, astro-ph/0211500 (2002);
- [26] R. Abusaidi, *PHYSICAL REVIEW LETTERS* 84 (2000), 5699;
- [27] N. Mirabolfathi, astro-ph/0412103 (2004);
- [28] J. Gascon, *Nuclear Physics B* 143 (2005), 423;
- [29] Y. Ramachers, M. Hirsch, H.V. Klapdor-Kleingrothaus, *Eur. Phys. J. A* 3 (1998), 93;
- [30] N. Spooner, *Phys. Reports* 307 (1998), 253;
- [31] A. Drukier, L.Stodolsky *Phys. Rev D* 30 (1984), 2295;
- [32] K. Scholberg, hep-ex/0511042 (2005);
- [33] G. Battistoni *et al.*, *stroparticle Physics* 19 (2003), 269;
- [34] R. Baranbei *et al.*, *Phys. Lett. B* 349 (2000), 23;
- [35] R. Baranbei *et al.*, *Int. J. Mod. Phys. D* 13 (2004), 2127;
- [36] W. Seidel, *Nucl. Phys. B* 138 (2005), 130;
- [37] T. Doke, K. Masuda, *Nucl. Instr. and Meth. A* 420 (1999), 62;
- [38] S. Kubota *et al.*, *Phys. Rev. B* 20 (1979) 3486;
- [39] S. Kubota *et al.*, *Phys. Rev. B* 17 (1978) 2762;
- [40] T. Doke *et al.*, *Nucl. Instr. and Meth. A* 291 (1990), 617;
- [41] M. Suzuki *et al.*, *Nucl. Instr. and Meth. A* 327 (1993), 67;
- [42] A. Hitachi *et al.*, *Phys. Rev. B* 27 (1983), 5279;
- [43] Hamamatsu Photonics, *Photomultiplier tube*, Japan (1994);
- [44] Photonis, *PHOTOMULTIPLIER TUBES principles & applications* , France (2002);

- [45] M. Ichige *et al.*, *Nucl. Instr. and Meth. in Ph. Res. A* 327, (1993) 144;
- [46] R. Dossi *et al.*, *Nucl. Instr. and Meth. in Ph. Res. A* 451, (2000) 623;
- [47] M. C. Prata *et al.*, *Characterization of ETL 9357FLA Photomultiplier Tubes for Cryogenic Temperature Applications*, ICARUS TM/04-18 (2004);